

Microhydrodynamics of driven and active filaments

By

Abhrajit Laskar

PHYS10200905002

The Institute of Mathematical Sciences, Chennai

A thesis submitted to the

Board of Studies in Physical Sciences

In partial fulfillment of requirements

For the Degree of

DOCTOR OF PHILOSOPHY

of

HOMI BHABHA NATIONAL INSTITUTE



July, 2016

STATEMENT BY AUTHOR

This dissertation has been submitted in partial fulfillment of requirements for an advanced degree at Homi Bhabha National Institute (HBNI) and is deposited in the Library to be made available to borrowers under rules of the HBNI.

Brief quotations from this dissertation are allowable without special permission, provided that accurate acknowledgment of source is made. Requests for permission for extended quotation from or reproduction of this manuscript in whole or in part may be granted by the Competent Authority of HBNI when in his or her judgment the proposed use of the material is in the interests of scholarship. In all other instances, however, permission must be obtained from the author.

Abhrajit Laskar

DECLARATION

I, hereby declare that the investigation presented in the thesis has been carried out by me. The work is original and has not been submitted earlier as a whole or in part for a degree / diploma at this or any other Institution / University.

Abhrajit Laskar

List of Publications arising from the thesis

Journal

- Published

1. **Abhrajit Laskar**, R Adhikari. *Filament actuation by an active colloid at low Reynolds number*. *New Journal of Physics*, 2017.
2. **Abhrajit Laskar**, R Adhikari. *Brownian microhydrodynamics of active filaments*. *Soft Matter*. 2015.
3. **Abhrajit Laskar**, Rajeev Singh, Somdeb Ghose, Gayathri Jayaraman, PB Sunil Kumar, R Adhikari. *Hydrodynamic instabilities provide a generic route to spontaneous biomimetic oscillations in chemomechanically active filaments*. *Nature, Scientific Reports*. 2013.
4. G Jayaraman, S Ramachandra, S Ghose, **Abhrajit Laskar**, M Bhamla, PB Sunil Kumar and R Adhikari. *Motility of Active Filaments due to Spontaneous Flow-Symmetry Breaking*. *Physical Review Letters* 109, 158302. 2012.

- In preparation

1. Lisa Tran, **Abhrajit Laskar**, R Adhikari, David J. Pine. *Friction at a distance in transient and steady states of a sedimenting chain*. 2016.

2. **Abhrajit Laskar**, R Adhikari. *Transients and steady states in the sedimentation of an active body*. 2016.

Abhrajit Laskar

List of presentations and participations at conferences

- SERC Non-linear Dynamics winter school, Delhi University, India, Dec, 2009
- Gravitation and Cosmology School, HRI, Allahabad, India June, 2010
- Soft Condensed Matter School, SNBNCBS, Kolkata, India, Dec, 2010
- Unifying Concepts of Material, JNCASR, Bangalore, India, Jan, 2012
- Statistical Mechanics School, RRI, Bangalore, India, April, 2012
- Discrete Simulation of Fluid Dynamics, JNCASR, Bangalore, India, July, 2012
- Bayesian inference workshop, Bayes by the bay, Pondicherry, India, January, 2013
- Poster presentation, Conference On Condensed Matter And Biological Systems (CCMB13), BHU, Varanasi, India, January, 2013
- Poster presentation, Diversity and Complexity: Realm of Today's Statistical Physics, SINP, Kolkata, India, January, 2013
- Statistical Mechanics School, RRI, Bangalore, India, April, 2013
- Poster presentation, Summer School Fundamental Problems in Statistical Physics XIII, Leuven, Belgium, June, 2013
- Complex Fluids-2013, IITD, Delhi, India, December, 2013
- Poster presentation and local organiser, SMYIM, Pondicherry, January, 2014
- Poster presentation, SMYIM-2, Pondicherry, December, 2014
- Poster presentation, Complex fluids-2014, JNCASR, Bangalore, December, 2014

- Talk presentation, New Colloids discussion meeting, RRI, Bangalore, India, July, 2015
- Poster presentation, Non-equilibrium collective dynamics-2015, Potsdam, Germany, Oct, 2015

List of Corrections

Below I summarize all the modifications I have made in my thesis “Microhydrodynamics of driven and active filaments” based on the referee reports and suggestions of doctoral committee.

The page numbers given below correspond to the pages of the previous version of the thesis which was sent to the referees for review.

- List of publications is updated.
- List of presentations and participations at conferences is included.
- Chapter4, The reference of electric field is dully removed from the text.
- Chapter5, The chemo-mechanical word is removed.
- Chapter5, Citations are added to clarify the comments “Previous studies on biomimetic motion and activity induced hydrodynamic interactions are not considered.”
- Spill over of title “list of figures” is corrected.
- Figure1.1, Spelling of Kramers is corrected.
- Section 5.2, Language “So, we here, are...”“...co-block polymers...” “which are consists of” is accordingly corrected.
- Section 5.3, typo in “...the detail dynamics...” is fixed.
- The glitches in reference are corrected.

ACKNOWLEDGMENTS

First and foremost, I would like to express my heartfelt gratitude to my supervisor Prof. Ronojoy Adhikari. His constant guidance and encouragement not only made this thesis possible but also helped me in shaping up where I am today with much more rationality and curiosity. His vast knowledge across fields, enthusiasm for learning new methods and techniques and power of critical analysis, ignoring needless details has influenced me beyond the realm of academics. He, as a researcher, will always be a source of inspiration. At the same time, his high expectations from students with perfectionist's viewpoint does take its toll during this era of "publish or perish".

In addition to my supervisor, I would like to thank Prof. S Nemani, Prof. S R Hassan, Prof. A Dua, and Prof. Purusattam Ray for their suggestions, constructive criticisms and fruitful discussions. Collaborations with Prof. P. B Sunil Kumar, Prof. Soumyajit Roy and Prof. David Pine have been very motivating, enjoyable and productive.

I also thank Rajesh Singh, Rajeev Singh, Raj Kumar Manna, Somdeb Ghose, Gayatri Jayaraman for many fruitful discussions on a variety of topics. I have enjoyed a lot spending time with you guys. Thank you very much for good advice at critical junctures.

I also convey my regards to Tanumoy Mandal, Chandan Maity, Sarbeswar paul, Amit K Bhattacharya, Arghya Dutta, Neeraj kamal, Sudhir N Pathak, Nirmalya Kajuri, Subhadeep Roy, Jahanur Hoque, Aritra Biswas, Tuhin Subhra Mukherjee, PV Sriluckshmy, Archana Mishra, Rohan Pujari, Dibyakrupa Sahoo, Arya S, Trisha Nath, Upayan Baul, Ushasi Roy, Madhumita Sahoo, Sushama and many others for making the hard time of PhD an enjoyable and memorable one.

Lastly, I express my sincere gratitude to my parents, my brother, sister-in-law and other family members for their constant support and always being there, when I needed them most.

Contents

Synopsis	1
1 Introduction	5
1.1 Slender bodies at the microscale	5
1.1.1 Examples from the natural world	5
1.1.2 Examples from bio-mimetics	6
1.1.3 Emergent behaviour	7
1.2 Theoretical models of slender bodies	8
1.3 Outline of the thesis	10
2 Microhydrodynamics of active slender bodies	13
2.1 Introduction	14
2.2 Modelling of slender bodies	15
2.3 Force and torque balance	17
2.4 Force and torque on active beads	19
2.4.1 Active slip	19
2.4.2 Expansion of surface distributions	20
2.4.3 Slip friction tensors	22
2.4.4 Boundary integral solution	23
2.4.5 Mobility and propulsion tensors	26
2.5 Flow due to active beads	30
2.6 Active Kramers model	33
2.7 Conclusion	34

3	Dynamics: motion and motility of an active filament	37
3.1	Introduction	38
3.2	Minimal active filament	39
3.3	Hydrodynamic instability	42
3.4	Free and tethered filament	43
3.5	Clamped filament	46
3.6	Linear stability analysis	51
3.7	Discussion and conclusion	55
4	External fields: sedimentation of an active filament	59
4.1	Introduction	59
4.2	Model description	60
4.2.1	Hydrodynamic forces	61
4.3	Sedimentation of a passive filament	63
4.3.1	Planar steady states	64
4.3.2	Transient and metastable states	64
4.3.3	Aplanar steady states	66
4.4	Sedimentation of an active filament	67
4.4.1	Planar steady states	68
4.4.2	Aplanar steady states and transients	68
4.4.3	Phase boundaries and dynamical features	71
4.5	Conclusion	72
5	Biomimetics: passive filament driven by an active colloid	75
5.1	Introduction	75
5.2	Model description	77
5.3	Dynamics of the assembly	79

5.4	Linear stability analysis	85
5.5	Conclusion	86
6	Emergence: collective dynamics of many active rods	89
6.1	Introduction	90
6.2	Model description	91
6.3	Dynamics of two active rods in unbounded flow	92
6.4	Dynamics of active rods near a wall	96
6.4.1	Single active rod	96
6.4.2	Two active rods	97
6.5	Dynamics of many active rods	100
6.6	Conclusion	102
7	Conclusion	105
A	Appendix	107
A.1	Constraint force on the tethered bead	107
A.2	Integrals and matrix elements	107
A.3	Discrete form of the writhe	108
A.4	Simulation method and parameters	109
	References	111

List of Figures

1.1	Passive filament models	8
2.1	Fluid flow around an active colloid in an unbounded domain	30
2.2	Fluid flow around an active colloid in a wall-bounded domain	31
3.1	Fluid flow around a minimal active filament	42
3.2	Steady states of the active filament - free and tethered	44
3.3	Comparison of filament kinematics and curvature dynamics.	45
3.4	Steady states of the active filament -clamped	46
3.5	Fluid flow around the active filament undergoing aplanar corkscrew rotation	47
3.6	Fluid flow around the active filament undergoing planar beating	48
3.7	Variation of the scaled timeperiod	49
3.8	Variation of the non-dimensionalised time period	50
3.9	Variation of rescaled volume of convex hull and variation of transition points	51
3.10	Variation of the largest non-zero eigenvalues of the stability matrix - free and tethered	52
3.11	Variation of the scaled real and imaginary parts of the largest eigenvalues	53
3.12	Variation of the largest scaled eigenvalues of the sacobian matrix - clamped	54
4.1	Fluid flow around a passive and a active bead under uniform external field	62
4.2	Planar steady state conformations of the passive filament	63
4.3	Transition dynamics from metastable state to terminal state	65
4.4	Power-dissipation during sedimentation	66

4.5	Aplanar steady states during sedimentation of passive filament	67
4.6	Steady states during the sedimentation of an active filament	69
4.7	Phase diagram of steady states of an active filament during sedimentation	70
5.1	Schematic diagram of a passive filament driven by an active colloid	77
5.2	Fluid flows around an assembly of passive-active colloids	80
5.3	Non-equilibrium steady states of the assembly	81
5.4	Writhe of the assembly during autonomous actuation	84
5.5	Phase diagram of dynamic steady states.	85
5.6	Linear stability analysis of the assembly	86
6.1	Dynamics of a pair of stiff extensile rods in an infinite medium	93
6.2	Dynamics of a pair of stiff contractile rods in an infinite medium	94
6.3	Autonomous motion of a T junction formed by a pair of contractile rods .	95
6.4	Instability of a single neutrally buoyant active rod near a wall.	96
6.5	Dynamics of a pair of neutrally buoyant extensile rods near a wall	98
6.6	Dynamics of a pair of neutrally buoyant contractile rods near a macro- scopic wall	99
6.7	Dynamics of many active rods in infinite flow and near a wall	101

Synopsis

In this thesis, we develop and apply a formalism applicable to the study of active slender bodies in the micro-hydrodynamic regime. Considering elasticity of the slender body, Brownian motion, activity at the fluid-structure interface and many-body hydrodynamic interaction, we present a general theory of active filaments. Then, we study the spontaneous motion of a minimal active filament which is force-free and torque-free. Thereafter, the dynamic response of the active filament in an external field is studied in detail. We further propose a new method of synthesising a motile micromotor by assembling a passive elastic filament with an active bead. We conclude the thesis with our study on the emergent behaviour of active rods near a wall.

In Chapter 1, the micro-hydrodynamics of slender bodies that can autonomously produce motion in a viscous fluid is introduced. We first provide an overview of those phenomena often found in biology, followed by recent developments of artificial active slender bodies that mimic their biological counterparts. We then review emergent collective dynamics of these bodies. Then we move on to provide a survey of theoretical advances spurred by these experimental studies. We conclude the section highlighting the need to develop particulate modelling to fill the gap between successful long-wavelength theories and experiments.

In Chapter 2, we develop a general theory of active slender bodies in a viscous fluid. Slender bodies capable of spontaneous motion in the absence of external actuation in an otherwise quiescent fluid are common in biological, physical and technological contexts. The interplay between the spontaneous fluid flow, Brownian motion, and the elasticity of the body presents a challenging fluid-structure interaction problem. We model the

problem by approximating the slender body as an elastic filament that can impose non-equilibrium velocities or stresses at the fluid-structure interface. We derive an equation of motion for such an active filament by enforcing momentum conservation in the fluid-structure interaction and assuming slow viscous flow. The fluid mediated interaction is obtained through a discretisation which replaces the continuous filament by a series of connected beads. These beads are active, have thin yet active boundary layers around them - which in turn - generate spontaneous hydrodynamic flow. The flow can be computed, to any desired degree of accuracy, by solving Stokes equation through boundary integral method in the presence of active boundary layers on the surfaces. By further applying the Kirkwood-Risemann superposition approximation to the solution, we obtain a simplified form of the equation of motion. This equation of motion forms the basis of our study of the dynamics of the active filaments in later chapters. Our model provides the foundation to study collective phenomena in momentum-conserving, Brownian, active filament suspensions, as we illustrate with a series of experimentally motivated applications.

In Chapter 3, we present a minimal model for an active filament in a viscous fluid and study the motion and dynamics of it by varying the strength of activity and boundary conditions. The filament is constituted by a series of apolar yet active beads, connected by nonlinear springs. The activity of the beads manifests in the production of spontaneous fluid flow. This flow can destabilise linear conformation of the active filament beyond a certain threshold and thus, provide a hydrodynamic route to autonomous motion. We study such motions of active filaments when they are a) free, b) tethered and c) clamped at one end as a function of a dimensionless ratio, the activity number \mathcal{A}_S , which is the ratio of the active and elastic forces acting locally on the filament. By varying this number, we observe a series of nonlinear steady states, arising from the complex interplay between the elasticity of the filaments, activity and fluid flow. In particular, we demonstrate a

spontaneous beating motion, which closely resembles the dynamics of a microtubule-motor assembly, observed in a recent experiment. Other steady states are reminiscent of motions observed in cilia and flagella. A linear stability analysis is performed to identify the nature of transitions from a linear quiescent state to states of filament motion. The system is stable, for any amount of activity, if hydrodynamic interactions are neglected. This observation highlights the crucial importance of hydrodynamic interactions in the non-linear dynamics of active slender bodies.

In Chapter 4, conformational dynamics and non-linear responses of an active filament are studied under a uniform external field. The competition between the flexibility of the slender body, external driving, internal activity and many-body hydrodynamic interaction yet another challenging fluid-structure interaction problem. External force and internal activity coupled with hydrodynamic interaction induce instabilities in both the parallel and the perpendicular direction to the applied field. Consequently, with the variation of applied external field and internal activity, while maintaining the structural properties of the filament, a series of steady states appear. Further by recognising two dimensionless measures, the activity number \mathcal{A}_S defined above, and sedimentation number \mathcal{S} , we demarcate regions of different steady states, characterised by their conformational and dynamical properties. We provide a qualitative understanding of the progression of steady states from a comparison of the hydrodynamic forces and torques due to internal activity and external driving. Our findings can be verified experimentally in the sedimentation of active biological filaments and chains of active phoretic beads.

In Chapter 5, we show that a passive semi-flexible filament can be actuated and transported by attaching an active colloid to its terminus. We study the dynamics of this assembly when it is free, tethered, or clamped. Linear states are destabilized by buckling instabilities to produce stable states of non-zero curvature and writhe. We demarcate boundaries of these states in the two-dimensional parameter space representing dimen-

sionless measures of polar and apolar activity. Our proposed assembly can be used as a novel component in the design of micro-machines at low Reynolds number.

In Chapter 6, we present the emergent behaviour of active rods in a viscous fluid in an unbounded domain and near a wall. Active rods in the micro-hydrodynamic regime produce spontaneous flow and interact with others hydrodynamically. As a consequence, in unbounded geometry, a pair of extensile rods attract each other when parallel but repel when perpendicular; the opposite obtains for the contractile case. These fluid mediated interactions lead to form assemblies, which are in general autonomously motile and dynamic in nature. The presence of no-slip wall modifies the properties of the spontaneous flow, the resultant hydrodynamic interaction and the dynamical behaviours. Though the dynamics parallel to the wall remains qualitatively the same, the dynamics perpendicular to it differs significantly due to the breaking of translational symmetry in the concerned direction. To elucidate the problem in detail, we successively investigate the dynamics of a single rod, a pair and many of them. Furthermore, the collective dynamics in unbounded and wall-bounded domains are compared with each other. Our theory and understanding provide the first crucial step to developing a microscopic theory of momentum conserving active anisotropic fluids near a wall. We conclude the chapter by comparing our findings with recent experiments on tri-metallic active rods near a wall and indicate further directions for the experiment.

In the last Chapter 7, we conclude with a brief summary of our study and directions for further study.

Introduction

The study of the flow produced by bodies immersed in a viscous fluid has a long and distinguished history going back to the invention of the microscope in the sixteenth century [1]. The study of the irregular movement of microscopic particles, viewable for the first time with the invention of the microscope, lay at the heart of the development of a new field of stochastic processes [2, 3, 4, 5, 6, 7, 8]. While the field continues to develop, expanding its reach to more complex systems and to areas outside of the traditional domain of physics [9], a more recent focus has been to study systems that are driven out of equilibrium by bodies that consume energy to do work on the fluid [10, 11, 12, 13]. The field of active matter, now a decade or so old, studies this novel class of non-equilibrium phenomena.

There are many systems that are driven out of equilibrium by local interaction, across different length scales. Here, in this thesis, we focus on micron-sized active slender bodies in a fluid environment. Examples are common in the context of biology, engineering and biotechnology. We introduce the topic below.

1.1 Slender bodies at the microscale

1.1.1 Examples from the natural world

Micron-sized slender bodies that can move autonomously or can be actuated by internal driving in a fluid, form the basis of motility at microscopic world. Prokaryotic bacteria employ whip-like appendages, known as flagella, to swim in a viscous fluid [14, 13].

Structurally these appendages are made of parallel microtubules tracks which are covered with membrane and attached to the cell body by a hook. The hook is continuously being rotated by an internal motor [15]. In the process, biological fuel such as adenosine triphosphate is consumed. The specific mechanisms of swimming vary from microbe to microbe, depending critically on the structure of the bodies, number of flagella, their relative positions and the medium they inhabit. Eukaryotic cells also swim by a continuous flapping of their flagella. On the contrary, the structure of eukaryotic flagella, cilia and spermatozoa are quite complex and the mechanism that initiates the actuation is also different. The spontaneous motions in those systems are achieved by motors walking on the microtubule tracks. This mechanism initiates sliding between microtubule tracks which in competition with inextensible elastic structure produces autonomous actuation [16, 17, 18, 19, 20, 21]. Such autonomous actuation is also of crucial importance in the functioning of ciliary layers, which push dust particles along with mucus out of the trachea and moves the ovum to target. In recent years, there is a fresh interest to develop autonomously motile bodies, that can perform similar tasks in-vitro and in micro-fluidic devices [22, 23, 24, 25, 26].

1.1.2 Examples from bio-mimetics

These fascinating autonomous appendages have inspired many experimental studies aimed at understanding the detailed mechanism and in developing micron-scale slender bodies that can perform similar work. In the first theme of studies, researchers dissect the appendages from the bodies, their internal structures and study them in the presence of fluid enriched with biological-fuel and motors. Few of those remarkable experiments include spontaneous coordinated wave motion of a headless bovine spermatozoa in a medium with ATP [27]; planar asymmetrical beating motion in a demembrated flagellar structure in a calcium-rich solution [28]; more recently, researchers have managed to assemble

microtubules in a motor-filled solution, which shows a remarkable cilia-like beating [23].

In the second theme of studies, researchers have achieved motility by injecting energy at the local scale. The common strategy is through the use of external fields such as electric, magnetic and ultra-sound [29, 30, 31]. Chemists have chosen a different route, they have patterned the surface of slender structures which can produce a local gradient and propulsion through local osmotic currents. Most remarkable development is the synthesis of such bodies that can move in water and in biofluid environment of the human vascular system [32, 33, 34]. In another noteworthy development, Williams et al [35] have selectively attached heart muscle cell on a slender metal body. The periodic contraction of the heart muscle drives the periodic waveforms on the slender body propelling it through the fluid. The speed of propulsion is controlled by the point of attachment along the contour length.

1.1.3 Emergent behaviour

The collective dynamics and emergent behaviour of these active bodies are no less interesting. In a bath of microbes, researchers have discerned spatiotemporally coherent motion, super-diffusion and density dependent large scale collective motion [36, 37, 38]. The presence of confinements makes these dynamics even more counterintuitive as found in recent studies [39, 40, 41, 42]. In a motility assay, biological filaments, sperm cells and microtubules self-organise spontaneously, forms novel patterns such as asters, vortices, spirals and so on [43, 44]. In microtubule-motor assembly, researchers have even found spontaneous formation and dissociation of defects [23, 45, 46]. More such observations include the formation of the 2-d crystal, decreased viscosity, enhanced diffusivity and phase separation [47, 48, 49, 50, 51]. Many of those emergent properties are yet to be fully understood in terms of mechanical theory, i.e. in terms of microscopic forces and torques acting on the constituent objects.

1.2 Theoretical models of slender bodies

To proceed towards a microscopic understanding and consequent modelling of such phenomena, it is worthwhile to survey the theoretical frameworks that have been used in the past in modelling passive slender bodies. The first, and earliest, is derived by extending classical beam theory [52]. The slender body is considered here as a space curve and a material frame is imagined along the curve. The elastic energy due to the bending and twisting of the slender body can easily be computed from this model has been exploited to understand the conformational dynamics and transition in shape for actuated filaments, growing bacteria and in knot formation [53, 54]. The predecessor of such modelling goes back to Kirchhoff in his study of elastic beams [52].

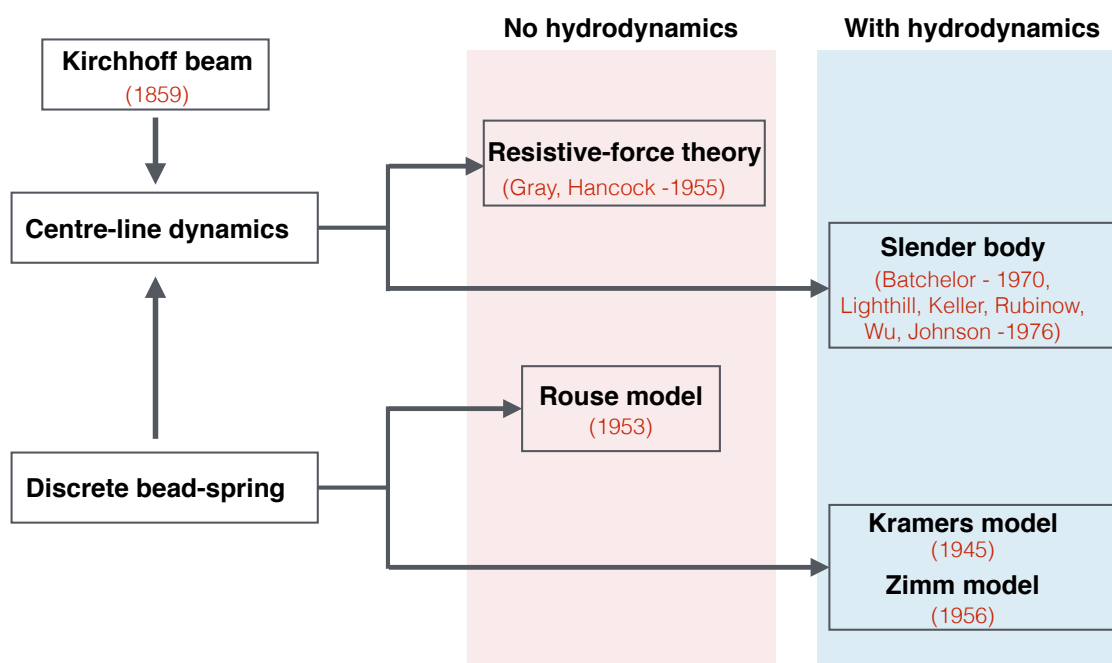


Figure 1.1: Frameworks for modelling slender bodies

Sometimes, in the absence of torsional modes or when the slenderness ratio of the body is small, the slender bodies can be modelled as a curve. This curve is chosen to be the centre-line of the body. Researchers had used it to understand beating motion

of bacterial flagella. In their study, the tail of the bacteria was modelled as a slender filament with stresses that arise from the internal activity. These bodies were studied under external periodic actuation with boundary conditions that approximate *in vitro* situations [18, 55, 56, 57].

In both the above classes of models, the local stresses from the ambient viscous fluid have to be modelled. This can be done at varying levels of sophistication. A common method is resistive force theory, where the effect of the fluid is replaced by anisotropic viscous forces that act locally [58]. Non-local hydrodynamic interaction is considered in slender body theory. The details of the theory can be found in [59, 60]. This method has been adapted in various studies of slender bodies under external driving [61, 62, 63].

In another class of models, developed in the context of macromolecules, slender bodies are modelled as a series of beads connected by non-linear potentials. The predecessor of such modelling traces back to Kramers [64]. In sequence, Rouse had extended it by considering a simple form of local friction [65] while Zimm did likewise by considering non-local hydrodynamic interactions [66]. This bead-spring model is now the most widely used framework for polymer dynamics [67].

Here we want to note that, the central-line dynamics and bead-spring models are closely related to each other. Bead-spring models of polymers can be mapped to a corresponding centre-line model in the limit where the separation between consecutive beads decreases to zero keeping the length of the polymer constant. Similarly, when the dynamics governed by center-line dynamics is discretised, for the purpose of numerical solutions, it yields a corresponding bead-spring model. In this sense, there is a one-to-one mapping between these two parallel developments.

In this thesis, we are interested in developing a mesoscopic theory of generic active slender bodies in a viscous fluid and applying it to study a variety of phenomena of current experimental interest. It is prudent to choose a simple model which can handle

hydrodynamic interactions, elasticity, Brownian motion and activity, and one which is amenable to numerical solutions. Given the enormous amount of effort that has been expended in studying the first three of the above mentioned phenomena within bead-spring models and the maturity of the framework [67] we choose, in this thesis, the bead-spring framework for constructing a microscopic theory of active slender bodies.

Bead-spring models of a single slender body can also be generalized, with little additional effort, to study collective dynamics of many such objects in a viscous fluid. The current understanding of the collective dynamics of active bodies is based upon two classes of theories. They are continuum theories and kinetic approaches [11, 12]. These approaches predict spontaneous breaking of symmetry at long wavelength limit in these systems, which lead to spontaneous motions and continuous generation of defects. But the complementary domain of short wavelength which is concerned with local fluctuations and shape of the body is yet to be fully explored. This domain is relevant in many experimental systems, where the number of active particles is not thermodynamically large. Our microscopic theory is able to model phenomena that lie outside the hydrodynamic limit, yet, reproduce hydrodynamic phenomena when the number of particles are large. Thus, we are able to delineate the limits of applicability of the hydrodynamic and kinetic theories by situating them within our microscopic framework.

1.3 Outline of the thesis

The outline of the thesis is as below. In Chapter 2, we develop a general theory of active slender bodies considering elasticity, hydrodynamic interactions, Brownian motion and activity. In Chapter 3, the autonomous motion of an active slender body is studied in detail. In Chapter 4, the motion of the active body is studied when it is subjected to an external field. In Chapter 5, we propose a new microscopic actuator combining a passive filament and an active colloid. In Chapter 6, the collective dynamics of active rods are

studied in an unbounded and wall-bounded domain. In Chapter 7, we conclude with a brief summary and possible future directions.

Microhydrodynamics of active slender bodies

A general theory of active slender bodies in a viscous fluid is developed in this chapter. The interplay between the spontaneous fluid flow, Brownian motion, and the elasticity of the body presents a challenging fluid-structure interaction problem. We model the problem by approximating the slender body as an elastic filament that can impose non-equilibrium velocities or stresses at the fluid-structure interface. Then, an equation of motion for the active filament is derived by imposing momentum conservation in the fluid-structure interaction and assuming slow viscous flow. The fluid mediated interaction is obtained through a discretization which replaces the continuous filament by a series of connected beads. The activity of the beads is expressed by an “active slip” that generates spontaneous hydrodynamic flow. The spontaneous flow and resulting hydrodynamic torque and force can be computed, to any desired degree of accuracy, by solving Stokes equation using the boundary integral method. Further considering only the leading order contributions of hydrodynamic interactions, a simplified form of the equation of motion can be obtained. We use this simplified form to perform numerical investigation about the dynamics of active and driven filaments in various conditions in later chapters. Our model provides the foundation to study collective phenomena in momentum-conserving, Brownian, active filament suspensions resolving the material at the scale of its constituents.

2.1 Introduction

Slender bodies capable of spontaneous motion in viscous fluids are common in biological, chemical, physical and technological contexts. Examples from biology, in increasing degree of molecular complexity, include microtubules driven by molecular motors, axonemes [28], cilia and flagella [55, 68, 69, 70, 24, 25, 71, 72, 27, 14, 73, 74, 58, 75, 76, 77]. In chemistry and physics, self-assembled bundles of microtubules driven by kinesin motors yield a model experimental system in which broken symmetry, collective excitations, and topological defects can be studied out of equilibrium [23, 45, 78]. In technology, much recent research has been directed towards the synthesis of slender bodies capable of spontaneous motion [79, 80, 81, 34, 82, 83, 84]. Such self-actuated slender bodies are expected to have many microfluidic and biomimetic applications [35, 85].

Despite the great variety in both the structure of the body and its mechanism of self-actuation, the examples above have three features in common: the spontaneous motion of the slender body produces flow in the ambient fluid, the body is of a size sufficiently small to make Brownian fluctuations important, and the body resists deformation produced by the spontaneous flow and Brownian fluctuations. Any universal emergent behaviour in active slender bodies must appear from the interplay between fluid flow, Brownian fluctuations and the elasticity. Such systems present a new class of fluid-structure interaction problems.

In this chapter, we construct a theory of active slender bodies, by modelling them as filaments that enforce slip velocities or non-equilibrium stresses at the fluid-structure boundary. A multitude of microscopic mechanisms can produce such velocities or stresses. Our theory isolates the specific microscopic details of self-actuation in the boundary conditions, from which universal, macroscopic fluid flow can be generated. Such flow results from the exchange of momentum between the body and the fluid, and since no external forces act on the body or the fluid, the sum of their linear momenta is conserved. In the

absence of external torques, the sum of their angular momenta is similarly conserved. These two constraints are explicitly taken into account when computing the fluid flow within our theory.

2.2 Modelling of slender bodies

As we have discussed in the Introductory chapter, there are many ways to model slender bodies with varying details. Singling out a particular model out of many possibilities depends on the phenomena or experiment one wants to model. Our approach here is to choose a model that is generic enough to reproduce the key phenomena seen in active filaments. These basic requirements of such a model are the elasticity of the filament to resist deformation of the body, internal activity which may lead to deformation and lastly, the hydrodynamic interaction between different parts of the body. With these in mind, we choose our slender body to be a slender filament, which we discretise by a set of finite sized spherical beads. These beads are connected to each other by nonlinear potential, are restricted to overlap each other and most importantly are active. The antecedent of such a bead-spring discretization of a continuous filament traces back to Kramers [64], who used it to model the dynamics of a polymer. The crucial difference between the model of Kramers and our adaptation of it is that the beads in our theory are active. The detail of our modelling of activity is presented in section 2.4.

Such chains of active beads have been used previously to model active filaments. In the earliest such model [86, 87, 88], the beads produce dipolar stresslet flows but are individually non-motile and are assumed so large that Brownian effects are negligible. In subsequent contributions [89, 90], the beads are taken to be motile, Brownian effects are included in two-dimensions but contributions from non-local hydrodynamic flow are neglected. In a related model, passive beads are driven by tangential active stresses, hydrodynamically correlated Brownian motion is included in three-dimensions but the

active flow is neglected [91, 92, 93]. Later, in another contribution [94], the activity is modelled through chemically active dimers and the dynamics is studied through multi-particle collision techniques. Our theory presented here contains all previous models as special cases.

Let us consider a suspension of N beads in a viscous fluid. There are many forces that act on the beads in the suspension. In the absence of any external driving, the relevant forces are internal body forces, Brownian noises and fluid mediated hydrodynamic forces. There may be additional body forces in the presence of external driving and constraining forces if the dynamics of the filament is restricted.

The internal body force acts to resist any deformation from its equilibrium conformation. This force on the n -th bead is $\mathbf{F}_n^{int} = -\nabla_n U$, where U is a non-linear potential. We assume the potential U to be a sum of connectivity, elastic, and self-avoidance potentials,

$$U = \sum_{m=1}^{N-1} U^C(\mathbf{R}_m, \mathbf{R}_{m+1}) + \sum_{m=2}^{N-1} U^E(\mathbf{R}_{m-1}, \mathbf{R}_m, \mathbf{R}_{m+1}) + \sum_{m < n} U^S(\mathbf{R}_n, \mathbf{R}_m). \quad (2.1)$$

The connectivity potential $U^C(\mathbf{R}, \mathbf{R}') = k(b - b_0)^2/2$, with elasticity parameter k , penalizes departures of the distance, $b = |\mathbf{R} - \mathbf{R}'|$, of two consecutive particles from the equilibrium value of b_0 . The elastic potential for bending $U^E = \bar{\kappa}(1 - \cos\phi)$, with rigidity parameter $\bar{\kappa}$, penalizes departures of the angle ϕ between consecutive bonds from their equilibrium value of zero. The rigidity parameter $\bar{\kappa}$ connects to bending rigidity κ as $\bar{\kappa} = \kappa b_0$. The self-avoidance potential U^S restricts the overlap of particles and is taken here to be a Lennard-Jones potential that vanishes smoothly at a distance $\sigma_{LJ} = 2^{\frac{1}{6}}\sigma$.

The net body force on the filament vanishes as can be easily verified by summing the body force on each particle.

2.3 Force and torque balance

In addition to the internal force, each of the constituent beads is acted upon by external body forces \mathbf{F}^e and surface forces due to both Brownian noise $\boldsymbol{\xi}^T$ and due to fluid mediated hydrodynamic force \mathbf{F}^H . Similarly, each bead could be driven by external body torque \mathbf{T}^e and surface torques due to both Brownian noise $\boldsymbol{\xi}^R$ and fluid mediated hydrodynamic torque \mathbf{T}^H . Therefore, the force balance and torque balance equations on n -th bead, given by Newtons law are,

$$M\dot{\mathbf{V}}_n = \mathbf{F}_n^H + \mathbf{F}_n^e + \mathbf{F}_n^{int} + \boldsymbol{\xi}_n^T, \quad (2.2)$$

$$I\dot{\boldsymbol{\Omega}}_n = \mathbf{T}_n^H + \mathbf{T}_n^e + \mathbf{T}_n^{int} + \boldsymbol{\xi}_n^R, \quad (2.3)$$

where M is the mass of the bead, I is the moment of inertia, \mathbf{V}_n is the velocity and $\boldsymbol{\Omega}_n$ is the angular velocity of the body.

Now at the micro-hydrodynamic regime, viscosity dominates the dynamics rather than the usual inertial force, we experience in our surroundings. Therefore, in the analysing motion of micro-scale or in developing theory at micro-scale, one can safely ignore the inertial effect arising from *both* particle and the fluid. There are many crucial consequences of viscosity dominated motion. The first of these is instantaneity . The motion is completely determined by the forces and torques that are exerted on the body at a particular moment, not from previous time instants. Further, it does not depend on the rate of exertion. This can be understood in a simple way. Let us assume a passive micron-sized bead is being driven by an external force and at a particular moment the external force is turned off. Now, the amount of time it will take and the distance it will cover before coming to rest is a measure the inertia of the motion. Purcell, in his work on ‘‘Life at low Reynolds number’’ [95], shows that these estimates are orders of magnitude smaller than the time scale and length scale of the colloidal motion under external influence. He

also demonstrates that, as a consequence, no reciprocal motion is possible: no swimmer with a single degree of freedom is able to move in a viscous fluid. The second consequence is the appearance of non-local many-body forces. The force and torque applied on any suspending body will affect all the other suspending bodies, as stresses can be transmitted through the fluid. Third, the Brownian motion of the suspended particles is now hydrodynamically correlated, a necessary consequence of the fluctuation-dissipation relation. Consequently, the Langevin description of Brownian motion required correlated noises whose covariance depends on the configuration of all particles. Considering these, Newton's equations in the microscopic domain reduce to a pair of constraints.

$$\mathbf{F}_n^H + \mathbf{F}_n^e + \mathbf{F}_n^{int} + \boldsymbol{\xi}_n^T = 0, \quad (2.4)$$

$$\mathbf{T}_n^H + \mathbf{T}_n^e + \mathbf{T}_n^{int} + \boldsymbol{\xi}_n^R = 0. \quad (2.5)$$

The crucial task left in Eq. (2.4 and 2.5) is to determine the hydrodynamic force and hydrodynamic torque on each bead in the presence of other beads, all of which have active boundary layer on them. We dedicate the next section for this task. We will first argue heuristically about the forms of the hydrodynamic moments and existence of generalized resistance tensors appealing to the linearity of slow viscous flow and of the boundary conditions. Though computing these generalized resistance tensors analytically is possible for simple geometries, it may not be the case for an arbitrary geometry. In the next subsection, we will elaborate the outline of a boundary integral method to compute the generalized resistance tensors analytically. Then, by inverting the resistance tensors we write down the general equation of motion for the active beads in a viscous fluid. We will conclude the section, by recovering the Kirkwood-Riseman mobility tensors and their new associates, the propulsion tensors, as a leading order approximation of our general theory. In the later chapters, we will use these forms to investigate systems of active slender bodies and demonstrate rich dynamics of these remarkable systems.

2.4 Force and torque on active beads

In the suspension of active beads, the force and torque that are exerted on a bead, say the n -th one, is given by,

$$\mathbf{F}_n^H = \int \mathbf{f} dS, \quad (2.6)$$

$$\mathbf{T}_n^H = \int \boldsymbol{\rho}_n \times \mathbf{f} dS. \quad (2.7)$$

where, $\mathbf{f} = \mathbf{n} \cdot \boldsymbol{\sigma}$ is the surface traction and $\boldsymbol{\sigma}$ is the fluid stress, first introduced by Cauchy [96], \mathbf{n} is the normal vector, $\boldsymbol{\rho}_n$ is the radius vector from centre of the body to its surface S . The fluid stress $\boldsymbol{\sigma} = -p\boldsymbol{\delta} + \eta(\nabla\mathbf{v} + \nabla\mathbf{v}^T)$ has both hydrostatic and viscous contributions and can be determined from conditions of incompressibility and local momentum conservation, which is Stokes equation in the micro-hydrodynamic domain.

$$\nabla \cdot \mathbf{v} = 0; \quad \nabla \cdot \boldsymbol{\sigma} = 0. \quad (2.8)$$

where \mathbf{v} is the fluid velocity, p is pressure and η is the viscosity.

The solution of this Stokes system provides the stress, from which the contact contribution of the force and torque on the every particle can be determined. In the absence of inertia and body forces, the conservation of particle momentum requires that the net contact force and the net contact torque on every particle be zero. The solution of the Stokes equation is determined by the boundary conditions on the particle surfaces and the macroscopic boundary, if present.

2.4.1 Active slip

Activity on the surface of the bead, in general, can modulate traction or velocity or both at the fluid-bead interface and can be expressed in a variety of boundary conditions on

the fluid through surface velocity and surface stress. We model activity on the surface of a chemo-mechanically active bead by the appearance of an additional boundary layer. When the width of the boundary layer, w , in comparison to the radius of the bead a , is thin ($w/a \ll 1$), the dynamics of the boundary layer can be ignored and asymptotic value of the velocity inside the boundary layer can be treated as modified boundary condition on the bead surface [97, 98, 99, 100]. We assume this modified condition to be an additional active slip velocity $\mathbf{v}^A(\boldsymbol{\rho}_n)$. This encompasses a wide variety of active phenomena, including electrophoresis, diffusiophoresis [100, 101, 102, 98], self-phoresis due to chemical catalysis [103, 104], and even swimming of microorganisms [105, 106, 107, 108]. We chose the fluid to be at rest at infinity. The boundary conditions, therefore, are

$$\mathbf{v}(\mathbf{R}_n + \boldsymbol{\rho}_n) = \mathbf{V}_n + \boldsymbol{\Omega}_n \times \boldsymbol{\rho}_n + \mathbf{v}^A(\mathbf{R}_i + \boldsymbol{\rho}_n) \quad \text{on } S_n \quad (2.9)$$

$$|\mathbf{v}(\mathbf{r})| \rightarrow 0, \quad |p(\mathbf{r})| \rightarrow 0, \quad |\mathbf{r}| \rightarrow \infty. \quad (2.10)$$

The first two terms in Eq. (2.9) are the usual kinematic contribution from the rigid body motion while the third term, is of dynamical origin, is the active slip.

Unlike the previous contributions, our choice of this additional velocity is any general vector field on the spherical surface of the bead [109, 110, 108, 88]. In the recent study [108], complex time-dependent patterns of swimming *Chlamydomonas Reinhardtii* and corresponding complex fluid flow around it has been constructed with high precision through the active slip model.

2.4.2 Expansion of surface distributions

Choice of spherical active beads allow us to expand the additional active slip \mathbf{v}^A and traction \mathbf{f} in a global basis. Our choice is tensorial spherical harmonics, $\mathbf{Y}^{(l)}$. On n -th

bead, whose radial coordinate is ρ_n , the tensorial spherical harmonics is defined as,

$$\mathbf{Y}_{\alpha_1 \alpha_2 \dots \alpha_l}^{(l)}(\hat{\boldsymbol{\rho}}_n) = (-1)^{l+1} \rho_n^{l+1} \nabla_{\alpha_1} \dots \nabla_{\alpha_l} \left(\frac{1}{\rho_n} \right). \quad (2.11)$$

In this basis, the surface velocity and traction on each particle can be expanded,

$$\mathbf{v}_n^A(\mathbf{R}_n + \boldsymbol{\rho}_n) = \sum_{l=1}^{\infty} \frac{1}{(l-1)!(2l-3)!!} \mathbf{V}_n^{(l)} \cdot \mathbf{Y}^{(l-1)}(\hat{\boldsymbol{\rho}}_n), \quad (2.12)$$

$$\mathbf{f}(\mathbf{R}_n + \boldsymbol{\rho}_n) = \sum_{l=1}^{\infty} \frac{2l-1}{4\pi a^2} \mathbf{F}_n^{(l)} \cdot \mathbf{Y}^{(l-1)}(\hat{\boldsymbol{\rho}}_n), \quad (2.13)$$

where, respective expansion coefficients for active velocity $\mathbf{V}_n^{(l)}$ and for traction $\mathbf{F}_n^{(l)}$, are tensors of rank l , are symmetric and irreducible in their last $l-1$ indices [109, 110]. Further using elementary SO(3) angular momentum algebra, these coefficients can be expressed as a sum of three irreducible tensors, symmetric(s) with rank l , antisymmetric(a) with rank $l-1$ and the trace(t) with rank $l-2$. Later, we use σ as a dummy index for irreducible multipoles of different ranks.

$$\mathbf{V}_n^{(l)} = \overline{\mathbf{V}_n^{(ls)}} + \overline{\boldsymbol{\epsilon} \cdot \mathbf{V}_n^{(la)}} + \overline{\boldsymbol{\delta} : \mathbf{V}_n^{(lt)}}, \quad (2.14)$$

$$\mathbf{F}_n^{(l)} = \overline{\mathbf{F}_n^{(ls)}} + \overline{\boldsymbol{\epsilon} \cdot \mathbf{F}_n^{(la)}} + \overline{\boldsymbol{\delta} : \mathbf{F}_n^{(lt)}}, \quad (2.15)$$

where, over-bracket represents the irreducible nature of the tensor underneath it.

Rigid body components for active slip can, now, easily be identified. They are linear velocity $\mathbf{V}_n^A = \mathbf{V}_n^{(1s)}$ and angular velocity $\boldsymbol{\Omega}_n^A = \mathbf{V}_n^{(2a)}/a$. In terms of active slip velocity, they are

$$4\pi a^2 \mathbf{V}_n^A = - \int \mathbf{v}^A(\boldsymbol{\rho}_n) dS_n, \quad (2.16)$$

$$4\pi a^2 \boldsymbol{\Omega}_n^A = - \frac{3}{2a^2} \int \boldsymbol{\rho}_n \times \mathbf{v}^A(\boldsymbol{\rho}_n) dS_n. \quad (2.17)$$

The above two equations have been known in the context of phoresis [100] and swimming by surface distortions [111]. They were later derived by the use of the Lorentz reciprocal relation [112] and by using boundary integral representation of Stokes flow [108].

2.4.3 Slip friction tensors

Appealing to the linearity of the governing Stokes equation (2.8) and the boundary condition (2.9), a set of linear relations between the velocity and traction coefficients can be assumed [110].

$$\mathbf{F}_n^{(l\sigma)} = -\gamma_{nm}^{(l\sigma,1s)} \cdot \mathbf{V}_m - \gamma_{nm}^{(l\sigma,2a)} \cdot \boldsymbol{\Omega}_m - \gamma_{nm}^{(l\sigma,l'\sigma')} \cdot \mathbf{V}_m^{(l'\sigma')}. \quad (2.18)$$

In writing the above, we have used the summation convention for repeated particle (n, m) and mode (l, σ) indices.

The linear relation can then be divided into sub-blocks and some of them can be recognised as classical friction tensors, which appear in rigid body motions of a passive colloid. The remaining are new friction tensors, arising due to active slip. The element of generalised friction tensor $\gamma_{nm}^{(l\sigma,l'\sigma')}$, relates the σ th irreducible part of l th rank traction coefficient to σ' th irreducible part of l' th rank velocity coefficient.

Here, we note down that, the friction tensors are many body in nature and encode hydrodynamic interaction between different active spherical beads. These tensors depend on the relative position of the active beads but do not depend on the orientation of the bodies. The traction coefficients $\mathbf{F}^{(l\sigma)}$, on the contrary, depend on orientation of the beads, which is concealed in active slip and its irreducible coefficients $\mathbf{V}^{(l\sigma)}$ [110].

The hydrodynamic force can be identified for the case $l = 1$ and $\sigma = s$ and hydro-

dynamic torque for $l = 2$ and $\sigma = a$. These terms are

$$\mathbf{F}_n^H = -\gamma_{nm}^{TT} \cdot \mathbf{V}_m - \gamma_{nm}^{TR} \cdot \boldsymbol{\Omega}_m - \gamma_{nm}^{(T,l\sigma)} \cdot \mathbf{V}_m^{(l\sigma)}, \quad (2.19)$$

$$\mathbf{T}_n^H = -\gamma_{nm}^{RT} \cdot \mathbf{V}_m - \gamma_{nm}^{RR} \cdot \boldsymbol{\Omega}_m - \gamma_{nm}^{(R,l\sigma)} \cdot \mathbf{V}_m^{(l\sigma)}. \quad (2.20)$$

Where, $\gamma_{nm}^{TT} = \gamma_{nm}^{(1s,1s)}$, $\gamma_{nm}^{TR} = \gamma_{nm}^{(1s,2a)}$, $\gamma_{nm}^{RT} = \gamma_{nm}^{(2a,1s)}$ and $\gamma_{nm}^{TT} = \gamma_{nm}^{(2a,2a)}$ are classical friction tensors and $\gamma_{nm}^{(T,l\sigma)}$ and $\gamma_{nm}^{(R,l\sigma)}$ relate the force and torque on the n -th bead to the $l\sigma$ mode of the active slip on the m -th bead. Inserting those contact forces and torques in the force balance equation (2.4) and the torque balance equation (2.5) we get,

$$-\gamma_{nm}^{TT} \cdot \mathbf{V}_m - \gamma_{nm}^{TR} \cdot \boldsymbol{\Omega}_m - \gamma_{nm}^{(T,l\sigma)} \cdot \mathbf{V}_m^{(l\sigma)} + \mathbf{F}_n^e + \mathbf{F}_n^{int} + \boldsymbol{\xi}_n^T = 0, \quad (2.21)$$

$$\underbrace{-\gamma_{nm}^{RT} \cdot \mathbf{V}_m - \gamma_{nm}^{RR} \cdot \boldsymbol{\Omega}_m}_{\text{viscous drag}} - \underbrace{\gamma_{nm}^{(R,l\sigma)} \cdot \mathbf{V}_m^{(l\sigma)}}_{\text{activity}} + \mathbf{T}_n^e + \mathbf{T}_n^{int} + \boldsymbol{\xi}_n^R = 0. \quad (2.22)$$

The noises $\boldsymbol{\xi}_m^T$ and $\boldsymbol{\xi}_m^R$ are hydrodynamically correlated and preserve fluctuation-dissipation theorem in equilibrium. Therefore, $\langle \boldsymbol{\xi}_n^\alpha \boldsymbol{\xi}_m^\beta \rangle = 2k_B T \gamma_{nm}^{\alpha\beta}$. We point here out that, though activity provides extra degrees of freedom to inject energy, the fluid does not restore these to the boundary layer through thermal fluctuations. Therefore, we should not expect a fluctuation-dissipation theorem when the active slip is non-zero.

2.4.4 Boundary integral solution

Though we have argued for the existence of resistance tensors, we did not provide the explicit computation of stress and traction using complete knowledge of active slip. Here, we provide an outline of a boundary integral method [113, 114]. to compute resistance tensors [110]. The first step of the method is to write down the fluid flow solution in terms of the boundary distributions as

$$v_i(\mathbf{r}) = - \sum_{m=1}^N \int G_{ij}(\mathbf{r}, \mathbf{r}_m) f_j(\mathbf{r}_m) dS_m + \sum_{m=1}^N \int K_{jik}(\mathbf{r}, \mathbf{r}_m) n_k v_j(\mathbf{r}_m) dS_m. \quad (2.23)$$

In general, the Green function \mathbf{G} , pressure tensor \mathbf{P} and stress tensor \mathbf{K} are connected to each other by,

$$\nabla_i G_{ij} = 0, \quad (2.24)$$

$$-\nabla_i P_j(\mathbf{r}, \mathbf{r}') + \eta \nabla^2 G_{ij} = -\delta(\mathbf{r} - \mathbf{r}') \delta_{ij}, \quad (2.25)$$

$$K_{ijk}(\mathbf{r}, \mathbf{r}') = -\delta_{ik} P_j + \eta (\nabla_k G_{ij} + \nabla_i G_{jk}). \quad (2.26)$$

Inserting the expanded forms of boundary sources, presented in an earlier section, in the boundary integral representation leads to a succinct expression for the fluid flow in terms of the expansion coefficients [109],

$$\mathbf{v}(\mathbf{r}) = - \sum_{m=1}^N \mathbf{G}^{(l)}(\mathbf{r}, \mathbf{R}_m) \cdot \mathbf{F}_m^{(l)} + \sum_{m=1}^N \mathbf{K}^{(l)}(\mathbf{r}, \mathbf{R}_m) \cdot \mathbf{V}_m^{(l)}. \quad (2.27)$$

The boundary integrals $\mathbf{G}^{(l)}$ and $\mathbf{K}^{(l)}$ can be evaluated explicitly in terms of the Green's function \mathbf{G} and its derivatives. In this expression, the velocity coefficients is computed from the boundary condition, but the traction coefficients remain unknown. To determine the traction coefficients, the boundary condition is first enforced on the boundary of n -th particle, the resulting equation is weighted by the l -th tensorial harmonic and finally integrated over the n -th boundary. This Galerkin procedure yields an infinite-

dimensional linear system of equations for the unknown traction coefficients [109],

$$-\mathbf{G}_{nm}^{(l,l')}(\mathbf{R}_n, \mathbf{R}_m) \cdot \mathbf{F}_m^{(l')} + \mathbf{K}_{nm}^{(l,l')}(\mathbf{R}_n, \mathbf{R}_m) \cdot \mathbf{V}_m^{(l')} = \begin{cases} \frac{1}{2} (\mathbf{V}_n - \mathbf{V}_n^A), & l\sigma = 1s \\ \frac{1}{2} (a\boldsymbol{\Omega}_n - a\boldsymbol{\Omega}_n^A), & l\sigma = 2a \\ \frac{1}{2} \mathbf{V}_n^{(l)}, & \text{otherwise,} \end{cases} \quad (2.28)$$

where the matrix elements $\mathbf{G}_{nm}^{(l,l')}$ and $\mathbf{K}_{nm}^{(l,l')}$ can, again, be evaluated analytically in terms of the Green's function \mathbf{G} and its derivatives. From this Eq. (2.28), one can derive elements of the friction tensor,

$$\gamma_{nm}^{(l\sigma, l'\sigma')} = \mathbf{P}^{(l\sigma)} \cdot \left[\mathbf{G}^{-1} \left(-\frac{1}{2}\mathbf{I} + \mathbf{K} \right) \right]_{nm}^{(l,l')} \cdot \mathbf{P}^{(l'\sigma')}. \quad (2.29)$$

where, $\mathbf{P}^{(l\sigma)}$ is the projection operator that projects $\mathbf{V}^{(l)}$ to its irreducible block $\mathbf{V}^{(l\sigma)}$. \mathbf{G} and \mathbf{K} are sub-blocks of the matrices $\mathbf{G}_{nm}^{(l,l')}$ and $\mathbf{K}_{nm}^{(l,l')}$. Details can be found in the recent paper [110].

The γ matrices encode hydrodynamic interactions and are long-ranged in nature. It is shown earlier that, the matrix element $\gamma_{nm}^{(l\sigma, l'\sigma')}$ to leading order is proportional to $\nabla_n^{l-1} \nabla_m^{l'-1} \mathbf{G}$ [110].

For a suspension of finite-sized beads in infinite domain, the Green's function \mathbf{G} takes the Oseen-Burgers form which decays as ρ^{-1} , with $\boldsymbol{\rho} = \mathbf{r} - \mathbf{r}'$, the separation vector between source point \mathbf{r}' and field point \mathbf{r} . Thus in infinite flow, all elements of the γ tensors can be computed explicitly. One can now easily see that, γ_{nm}^{TT} decay as ρ_{nm}^{-1} , γ_{nm}^{TR} and γ_{nm}^{RT} decay as ρ_{nm}^{-2} , γ_{nm}^{RR} decay as ρ_{nm}^{-3} , in general, $\gamma_{nm}^{(T,l\sigma)}$ decay as ρ_{nm}^{-l} while the $\gamma_{nm}^{(R,l\sigma)}$ decay more rapidly as $\rho_{nm}^{-(l+1)}$, where $\rho_{nm} = |\mathbf{R}_n - \mathbf{R}_m|$ is the distance between the centre of the n -th and m -th beads. For $n = m$, all slip friction matrices other than $\gamma_{nn}^{(T,1s)} = 6\pi\eta a\boldsymbol{\delta}$ and $\gamma_{nn}^{(R,2a)} = 8\pi\eta a^3\boldsymbol{\delta}$ are zero [110].

For wall bounded domain, the Green function \mathbf{G} takes Lorentz-Blake form [115, 116] and following similar procedure, elements of the corresponding resistance tensors can be obtained.

The friction formulation, presented so far, provides a clear understanding of the physics of the problem but is cumbersome to solve numerically, as the resulting kinematic equations are implicit. For numerical solutions, it is convenient to construct explicit equations involving linear and angular velocities given in terms of external force, internal body force and given coefficients of active velocity slip.

2.4.5 Mobility and propulsion tensors

By rearranging Eq. (2.21) and Eq. (2.22), the linear and angular velocity of the n -th bead can be obtained in terms of mobility tensors $\boldsymbol{\mu}_{nm}$ and a new set of propulsion tensors $\boldsymbol{\pi}_{nm}$. Mobility and propulsion tensors now encode hydrodynamic interaction between the beads and for the efficient numerical purpose, one needs to use approximate forms for them. While mobility matrices can be computed by inverting the sub-block of the friction tensor that deals with translation and rotation of the beads, propulsion matrices can be shown to be [110],

$$-\boldsymbol{\pi}_{nm}^{(T,l\sigma)} = \boldsymbol{\mu}_{nq}^{TT} \cdot \boldsymbol{\gamma}_{qm}^{(T,l\sigma)} + \boldsymbol{\mu}_{nq}^{TR} \cdot \boldsymbol{\gamma}_{qm}^{(R,l\sigma)}, \quad (2.30)$$

$$-\boldsymbol{\pi}_{nm}^{(R,l\sigma)} = \boldsymbol{\mu}_{nq}^{RT} \cdot \boldsymbol{\gamma}_{qm}^{(T,l\sigma)} + \boldsymbol{\mu}_{nq}^{RR} \cdot \boldsymbol{\gamma}_{qm}^{(R,l\sigma)}. \quad (2.31)$$

Using those tensors, the update equations for an active bead in mobility formalism are

$$\begin{aligned}
\mathbf{V}_n = & \underbrace{\boldsymbol{\mu}_{nm}^{TT} \cdot (\mathbf{F}_m^e + \mathbf{F}_m^{int}) + \boldsymbol{\mu}_{nm}^{TR} \cdot (\mathbf{T}_m^e + \mathbf{T}_m^{int})}_{\text{passive}} \\
& + \underbrace{\sqrt{2k_B T \boldsymbol{\mu}_{nm}^{TT}} \cdot \boldsymbol{\zeta}_m^T + \sqrt{2k_B T \boldsymbol{\mu}_{nm}^{TR}} \cdot \boldsymbol{\zeta}_m^R}_{\text{Brownian}} + \underbrace{\boldsymbol{\pi}_{nm}^{(T,l\sigma)} \cdot \mathbf{V}_m^{(l\sigma)}}_{\text{active}}, \quad (2.32)
\end{aligned}$$

$$\begin{aligned}
\boldsymbol{\Omega}_n = & \underbrace{\boldsymbol{\mu}_{nm}^{RT} \cdot (\mathbf{F}_m^e + \mathbf{F}_m^{int}) + \boldsymbol{\mu}_{nm}^{RR} \cdot (\mathbf{T}_m^e + \mathbf{T}_m^{int})}_{\text{passive}} \\
& + \underbrace{\sqrt{2k_B T \boldsymbol{\mu}_{nm}^{TT}} \cdot \boldsymbol{\zeta}_m^T + \sqrt{2k_B T \boldsymbol{\mu}_{nm}^{TR}} \cdot \boldsymbol{\zeta}_m^R}_{\text{Brownian}} + \underbrace{\boldsymbol{\pi}_{nm}^{(R,l\sigma)} \cdot \mathbf{V}_m^{(l\sigma)}}_{\text{active}}. \quad (2.33)
\end{aligned}$$

The positivity of dissipation ensures that mobility matrices are positive-definite and Onsager symmetry constrains them to be symmetric in both the particle and translation-rotation indices. These two properties ensure that a mobility matrix can be factorised into a lower triangular matrix and its transpose, any one of which is a “square-root” of the mobility matrix. The fluctuations can then be expressed as products of uncorrelated Wiener processes $\boldsymbol{\zeta}^T, \boldsymbol{\zeta}^R$ and the “square-root” Cholesky factors.

The coupled Langevin equations (2.32) and (2.33), are a generalisation of Einstein-Smoluchoski description of diffusion of passive suspension to their active counterpart. For passive suspension, hydrodynamically correlated diffusive motion of N colloidal particles was completed by several authors using Liouville, kinetic theory, Fokker-Planck and Langevin approaches [117]. In the absence of activity, they reduce to the equation of Brownian dynamics with hydrodynamic interactions [118]. When the forces derive from positional and angular potentials, the form, chosen for the fluctuations ensures that the Gibbs distribution of the positions and orientations is the stationary distribution. When activity is included, the balance between fluctuation and dissipation is no longer main-

tained and stationary states are no longer described by the Gibbs distribution. As we show in the remainder of the thesis, non-trivial stationary states are obtained when the beads are chained together into filaments.

By using an iterative method, one can compute the mobility and the propulsion tensors to any desired accuracy and order [110]. To the leading order in \mathbf{G} , mobility tensors can be shown to be,

$$\boldsymbol{\mu}_{nm}^{TT} = \begin{cases} \frac{1}{6\pi\eta a} \boldsymbol{\delta} & m = n \\ \mathcal{F}^0 \mathcal{F}^0 \mathbf{G}(\mathbf{R}_n, \mathbf{R}_m) & m \neq n \end{cases} \quad (2.34)$$

$$\boldsymbol{\mu}_{nm}^{TR} = \begin{cases} 0 & m = n \\ \frac{1}{2} \nabla_m \times \mathbf{G}(\mathbf{R}_n, \mathbf{R}_m) & m \neq n \end{cases} \quad (2.35)$$

$$\boldsymbol{\mu}_{nm}^{RT} = \begin{cases} 0 & m = n \\ \frac{1}{2} \nabla_n \times \mathbf{G}(\mathbf{R}_n, \mathbf{R}_m) & m \neq n \end{cases} \quad (2.36)$$

$$\boldsymbol{\mu}_{nm}^{RR} = \begin{cases} \frac{1}{8\pi\eta a^3} \boldsymbol{\delta} & m = n \\ \frac{1}{4} \nabla_n \times \nabla_m \times \mathbf{G}(\mathbf{R}_n, \mathbf{R}_m) & m \neq n \end{cases} \quad (2.37)$$

The diagonal parts of these matrices are one-body terms while the off-diagonal parts represent the hydrodynamic interactions. The diagonal parts are the familiar Stokes translational and rotational mobilities while the off-diagonal parts can be recognised as the Rotne-Prager-Yamakawa tensors [119, 120] and their generalizations to rotational motion. The Onsager symmetry of the mobility matrix is manifest in these expressions.

Similarly, the propulsion matrices can also be computed [109], which are

$$\pi_{nm}^{(T,l)} = \begin{cases} \delta & m = n, l\sigma = 1s \\ 0 & m = n, l\sigma \neq 1s \\ c_l \mathcal{F}^0 \mathcal{F}^{(l-1)} \nabla_m^{(l-1)} \mathbf{G}(\mathbf{R}_n, \mathbf{R}_m) & m \neq n \end{cases} \quad (2.38)$$

$$\pi_{nm}^{(R,l)} = \begin{cases} \frac{1}{a} \delta & m = n, l\sigma = 2a \\ 0 & m = n, l\sigma \neq 2a \\ \frac{c_l}{2} \nabla_n \times \nabla_m^{(l-1)} \mathbf{G}(\mathbf{R}_n, \mathbf{R}_m) & m \neq n \end{cases} \quad (2.39)$$

where, \mathcal{F}^l is the operator

$$\mathcal{F}^l = \left(1 + \frac{a^2}{4l+6} \nabla^2 \right).$$

that accounts for the finite-size Faxen correction for the flow due to a bead of radius a and c_l is a numerical constant.

The form of mobility and propulsion matrices, we have thus got for beads of radius a by considering solution after the first iteration, can be computed through alternative way through the pair-wise superposition approximation, first introduced by Kirkwood and Riseman [121], in the context of the dynamics of a polymer. This match of our theory with the popular superposition method not only reiterates the validity of our method but also underlines the superiority of our method to do more accurate numerical studies with hydrodynamic interaction. It can easily be done numerically, by increasing the number of iteration. With this approximation, the mobility matrices reduce to the well-known Rotne-Prager-Yamakawa tensors while the propulsion matrices are obtained analytically [109] as gradients of the fundamental solution of the Stokes equation for an unbounded fluid. For a passive polymer, Yoshizaki and Yamakawa [122] verified that the superpos-

ition approximation is correct to $\mathcal{O}((a/b)^3)$, where b is the mean separation between beads, as $N \rightarrow \infty$. Since the propulsion matrices decay more rapidly with separation than mobility matrices, the superposition approximation for active filaments is also accurate to $\mathcal{O}((a/b)^3)$ [109].

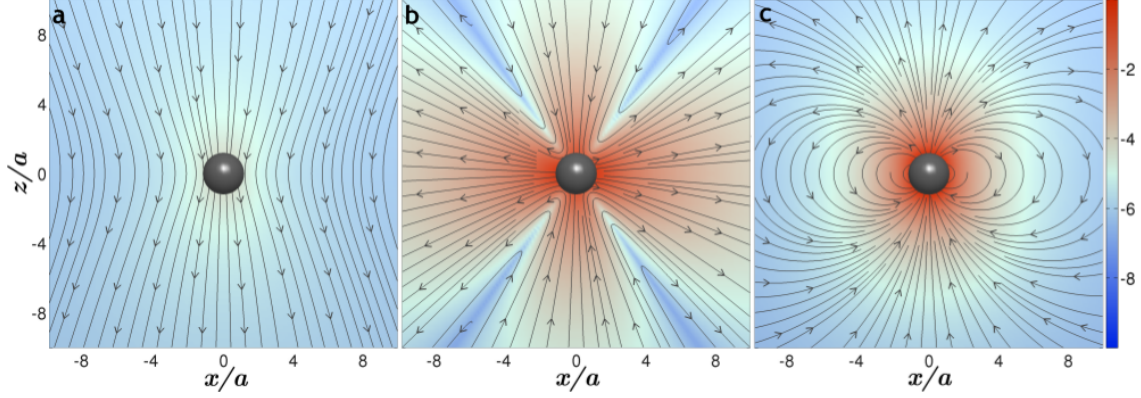


Figure 2.1: Streamlines of irreducible modes of slow viscous flow around an active bead. Displayed in (a) is $\mathcal{F}^0 \mathbf{G} \cdot \mathbf{F}$, the flow around a bead translating under the action of a force \mathbf{F} ; in (b) is $\mathcal{F}^1 \nabla \mathbf{G} \cdot \mathbf{V}^{(2s)}$, the minimal flow around a non-motile active bead; and in (c) is $\nabla^2 \mathbf{G} \cdot \mathbf{V}^{(3t)}$, the minimal flow around a motile active bead. In the limit $a \rightarrow 0$, the flows in (a) and (b) reduce to a Stokeslet and stresslet, respectively, while (c) is a degenerate velocity quadrupole. The background colour is proportional to the logarithm of the velocity magnitude.

2.5 Flow due to active beads

To understand the dynamics of the active bodies, it is crucial to know the kind of spontaneous flow they generate. The flow due to N beads in the fluid can easily be computed from

$$\mathbf{v}(\mathbf{r}) = \sum_{m=1}^N \mathbf{G}^{(l)}(\mathbf{r}, \mathbf{R}_m) \cdot \mathbf{F}_m^{(l)} - \sum_{m=1}^N \mathbf{K}^{(l)}(\mathbf{r}, \mathbf{R}_m) \cdot \mathbf{V}_m^{(l)}. \quad (2.40)$$

when all the traction and velocity coefficients are known either directly or from the solution of the Stokes equation. Depending upon the geometry of the domain, the kernels

will change to satisfy boundary conditions. If we consider the domain to be an infinite medium the Green function is the Oseen-Burgers tensor. On the other hand, if the domain is near a no-slip wall, the green function will be the Lorentz-Blake tensor.

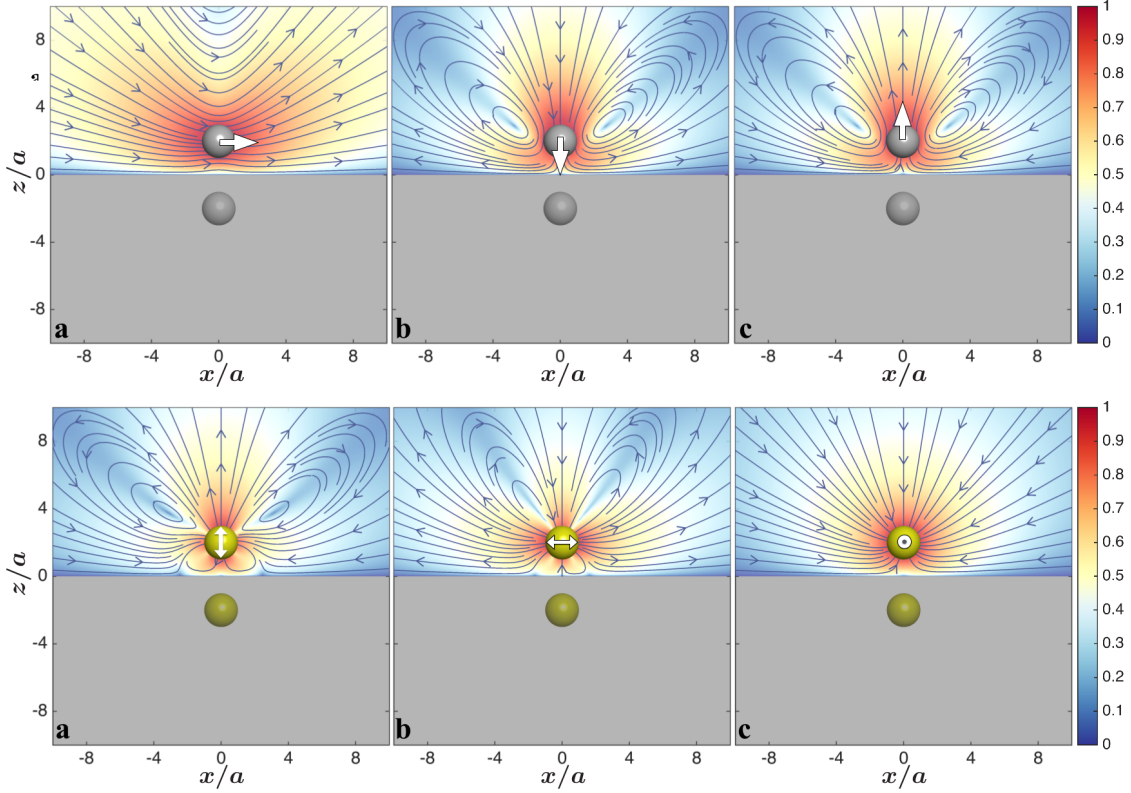


Figure 2.2: Distortion of streamlines of irreducible modes of slow viscous flow around an active bead is shown near a macroscopic wall. Displayed in (first row) are $\mathcal{F}^0 \mathbf{G}^w \cdot \mathbf{F}$, the flow around a bead translating under the action of a force \mathbf{F} in the direction x , $z-$ and $z+$ respectively; in (second row) are $\mathcal{F}^1 \nabla \mathbf{G}^w \cdot \mathbf{V}^{(2s)}$, the minimal flow around a non-motile apolar active bead when its director is pointed towards z , x and y . The background is pseudo coloured with the logarithm of the velocity field, normalised with the maximum value of the domain.

In an unbounded domain, these kernels become translation invariant and become function of only the separation $\boldsymbol{\rho} = \mathbf{r} - \mathbf{r}'$, \mathbf{r} and \mathbf{r}' are being field point and source points respectively.

$$8\pi\eta G_{ij} = \frac{\delta_{ij}}{\rho} + \frac{\rho_i \rho_j}{\rho}. \quad (2.41)$$

The corresponding fluid flow due to different basic irreducible multipoles is shown in

the Fig. (2.1). In a) the flow-field around a passive colloid is shown when it subjected to an external field. In b) the flow-field is due to the leading order *apolar* active multipole. In c) the flow is due to the leading order *polar* active multipole, known as potential dipole or degenerate quadrupole. The strength of the flowfields due to Stokeslet, Stokes dipole and degenerate quadrupole decay as ρ^{-1} , ρ^{-2} and ρ^{-3} respectively with the increase of separation. When a particle autonomously spins without any external torque, a particular multipole, the spinlet is active. This mode decays as ρ^{-4} and is, therefore, short ranged in nature [108].

Similarly, the flow near a macroscopic wall with no-slip boundary condition on it can be computed. This was first recognised by Lorentz [115] and a modern formulation was given by Blake [116]. The corresponding Green's function \mathbf{G}^w is

$$G_{ij}^w = G_{ij} - G_{ij}^* - 2h\mathbf{M}\nabla_j G_{i3}^* + 2h^2\mathbf{M}\nabla^2 G_{ij}^*. \quad (2.42)$$

where $\mathbf{M} = (1 - 2\hat{n}\hat{n})$ is the mirror operator with \hat{n} is the unit normal vector on the macroscopic boundary and G^* represents Green's function due to virtual source, which is at the position of the virtual image - $\mathbf{r}^* = \mathbf{M}\mathbf{r}$. In the Fig. (2.2), we present flow fields around a colloid near a macroscopic wall, when it is driven by an external field in different directions and around a non-motile active colloid of radius a . In the first row, the external force is parallel to the wall in (a), towards the wall in (b) and away from the wall in (c). In the second row, the orientation of the apolar active colloid is perpendicular to the wall in (a) and parallel to the wall in (b) and (c). In the first case, the flow has cylindrical symmetry, fluid comes from equatorial regions and goes toward polar region. While in other two cases, the flow-field does not have cylindrical symmetry. The fluid flow around those beads looks like the flow-field given in (2.1b), when their orientations are aligned. Near a wall, the strength of the flowfields due to Stokeslet,

Stresslet and degenerate quadrupole decay as ρ^{-2} , ρ^{-3} and ρ^{-4} respectively with increase of separation. Clearly the only active term that contributes to long range interaction is stresslet. Other active terms can contribute by inducing Stokeslet or rotlet by some local mechanisms.

2.6 Active Kramers model

Over the last few sections, we have presented a method to compute hydrodynamic forces and torques on an active bead in a suspension. We have also provided the equations of motion to describe their dynamics (Eq. 2.32 and 2.33). Now, considering internal body force, described by non-linear elastic potential (Sec. 2.2), we write down the coupled equation for an active filament. Moreover, the rotational motion of the beads can be ignored, assuming torsional potentials that prevent such rotations. Therefore, the orientation of the beads is no longer a dynamical degree of freedom to be determined from the angular velocity, but is prescribed. It is natural to fix the orientation of n -th bead, $\mathbf{p}_n = \alpha_1 \mathbf{t}_n + \alpha_2 \mathbf{n}_n + \alpha_3 \mathbf{b}_n$, in the local Frenet-Serret frame in terms of the of the tangent \mathbf{t}_n , normal \mathbf{n}_n and binormal \mathbf{b}_n , and the direction cosines are $\alpha_{i \in \{1,2,3\}}$. Combining all of the above, we obtain the following equation of motion for active filaments,

$$\begin{aligned} \dot{\mathbf{R}}_n = & \frac{\mathbf{F}_n^b}{6\pi\eta a} + \sum_{m \neq n}^N \mathcal{F}^0 \mathcal{F}^0 \mathbf{G} \cdot \mathbf{F}_m^b + \sum_{m \neq n}^N \left(\frac{2k_B T}{6\pi\eta a} \boldsymbol{\delta} + 2k_B T \mathcal{F}^0 \mathcal{F}^0 \mathbf{G} \right)^{\frac{1}{2}} \cdot \boldsymbol{\zeta}_m \\ & + \underbrace{\sum_{m \neq n}^N \sum_{l=2}^{\infty} c_l \mathcal{F}^0 \mathcal{F}^{(l-1)} \nabla_m^{(l-1)} \mathbf{G} \cdot \mathbf{V}_m^{(l)}}_{\text{Active}} + \mathbf{V}_n^a. \end{aligned} \quad (2.43)$$

where, $\mathbf{F}_n^b = \mathbf{F}_n^e + \mathbf{F}_n^{int}$ is net body force on n -th monomer.

These stochastic differential equations describe the Brownian dynamics of an extens-

ible, semi-flexible, self-avoiding active filament including hydrodynamic interactions that arise from the exchange of momentum between the filament and its local conservation in the bulk fluid. The square-root of the mobility matrix in the third term above is to be interpreted as a Cholesky factor. These equations are the natural extension of Brownian hydrodynamics of passive filaments to the active case and contain both the Rouse and Zimm descriptions of equilibrium polymers.

2.7 Conclusion

In this chapter, a general mesoscopic theory of active slender bodies in a viscous fluid is developed. Our theory considers key mechanisms that are found in a variety of in-vivo and in-vitro experiments. They are the restoring elasticity of the slender body, destabilising internal activity, non-local many-body hydrodynamic interaction and correlated Brownian motion. We also keep the provision for inclusion of external driving, force and torque that might arise from various kinds of constraint motions, shear and incident fluid flow in general. Therefore, our general theory of active filaments includes all the possibilities and all other models [89, 90, 91, 92, 94] can be derived as special cases.

The equations of motion, presented provide the foundation for studying non-equilibrium statistical mechanics of active filaments. The coupled Langevin equation for the positions can be recast as Fokker-Planck equations, whose stationary solutions in the absence of activity are given by the Gibbs distribution. Activity, in the forms envisaged in this work, introduces an additional drift in the Fokker-Planck equation, destroying the balance between fluctuation and dissipation. This will lead to non-Gibbsian distributions in the stationary state, and, likely change well-known equilibrium properties like statics of the coil-globule transition [123] and the distribution of loop closure times [103]. We believe that some of these problems can be addressed both experimentally and through theory and simulations.

Numerically, our method yields the hydrodynamic interaction between particles without the need to resolve bulk fluid degrees of freedom. This makes our theory useful for computing the hydrodynamic interaction of active particles in three dimensions, as the computational cost of resolving fluid degrees of freedom is greatly reduced [109, 124].

Moreover, due to generality of our theory, it can model many mesoscopic phenomena in the microscopic length scale, may it be the motion of elongated microbes [125], their appendages such as cilia and flagella, axonemes, or even self-assembled filamentous structures such as motor-microtubule assembly engineered in [23, 45]. It can also model slender bodies driven by external field [126, 127, 128, 129] or internal activity [35]. Our theory includes the dynamics when both internal activity and external driving are present simultaneously [130, 131, 132].

In recent times, researchers have synthesised microscopic bodies that can self-propel by momentum conserving complex interaction with the peripheral fluid environment [133, 81]. Our momentum conserving theory has the ability to describe the individual as well as the collective motion, resolving motion at the scale of the constituent. In the rest of the chapters, we study models inspired by recent experiments and demonstrate the generality of our theory and the power of the numerical method.

Dynamics: motion and motility of an active filament

Autonomous motion and dynamics of an active filament in a viscous fluid is studied as an archetypical representative of the class of problem on active slender bodies. Considering only the leading order activity and non-local hydrodynamic interaction between different segments of the filament, we introduce our minimal model. This filament is envisaged as a series of apolar active beads, connected by nonlinear springs. The activity of the beads here is manifested not by self-propulsion but by the production of non-equilibrium fluid flow. This spontaneous flow, beyond a certain threshold, can destabilise linear conformation of the active filament and thus provides a hydrodynamic route to autonomous motion. To characterise the dynamics of the active filament, we define a dimensionless number - the activity number - as the ratio between activity and elasticity of the filament. We further study the motion of the active filament when it is a) free, b) tethered and c) clamped at one end. We find a series of nonlinear steady states, arising from the complex interplay between the elasticity of the filaments, activity and fluid flow. In particular, we demonstrate that our model can reproduce spontaneous beating motion, observed in a recent experiment of a microtubule-motor assembly. Other steady states observed in our numerical study also resemble motions often found in cilia and flagella. We characterize those states by measuring the time period and amplitude of the oscillations and by presenting the spontaneous fluid flow around the dynamical structures. To identify the nature of the transition from linear conformation to nonlinear dynamical states, we have

also carried out a linear stability analysis. Remarkably, similar analysis neglecting non-local contributions of spontaneous flow does not produce an instability. This highlights the crucial role of non-local hydrodynamic interactions in the dynamics of active slender bodies.

3.1 Introduction

Autonomous motion of micron-sized slender bodies in the absence of any external driving are quite common in biological contexts and recently in technological contexts. Examples of such slender structures in biology are cilia, flagella both bacterial and eukaryotic, axonemes and microtubule-motor assembly [28, 23, 14, 27]. Those active machines are crucial for motility at cellular scale, from individual motion, to accomplish important tasks together such as removing dust particle from lungs, moving ovum to uterus and transport [24, 70, 134]. Even inside a cell, the microtubule-motor assemblies provide routes for transporting important ingredients to target parts beating diffusive barrier. Cilia and eukaryotic flagella are the slender extensions of cellular matrix, formed by a combination of 9+2 pairs of microtubular tracks and wrapped around by cellular membrane. When molecular motors walk on the microtubular tracks by using biochemical fuel ATP, sliding occurs between nearby micro tubule tracks, leading to bending, which results in spontaneous motion [135]. It is also been observed that the internal structure of those organelle in the absence of cell membrane, known as axoneme, demonstrate spontaneous movements in vitro [28]. Prokaryotic or bacterial flagella, on the other hand, are not extension of cellular matrix, but separate slender body part which is attached to the cell by a hook. This kind of flagella is formed from protein flagellin [14]. To achieve motility, the hook is rotated by some internal mechanism using biochemical fuels. Lately, in vitro experiments from Dogic group demonstrate astonishing phenomena of microtubule-motor assembly in the presence of ATP. In their contributions [23, 45, 136], cilia-like beating motion, spon-

taneous transport mechanism and collective streaming motion are observed. All those in-vivo and in-vitro observations in biology with their qualitatively similar outcome indicate that some universal physical mechanism rather than detail individual mechanism might be behind them. We will explore this mechanism in this chapter.

3.2 Minimal active filament

In the earlier chapter, we have already presented the most general equation of motion for active slender bodies considering internal activity, Brownian noise and elasticity of the body. We have also shown there that chemo-mechanical activity can produce a variety of nontrivial modes in the absence of any external driving. Those modes decay differently in the fluid medium and can be classified using symmetry in terms of polar and apolar, chiral and achiral. Usually, different synthetic or biological machines can easily be modeled with sufficient accuracy by isolating few selected modes out of all. For instance, The slowest decaying active mode is stresslet or Stokes dipole, which is apolar and achiral and decays as ρ^{-2} . When the body is propelling autonomously, it predominantly excites a particular active mode that is known as degenerate quadrupole or potential dipole. This mode is polar yet achiral and decays as ρ^{-3} . Similarly, an autonomously spinning body without translation excites a particular mode, the spinlet, which is an apolar yet chiral and decays as ρ^{-4} . It is important to note that the last two modes contribute directly to the one body motion whereas leading order contribution of many body hydrodynamic interaction comes from Stokes dipole. As a consequence, the motion of any micro-swimmers can be modelled to the leading order by considering these three basic multipoles.

In our minimal model of the active filament, the beads are non-motile, $\mathbf{V}_n^A = 0$, and all active velocity components other than the symmetric part of $\mathbf{V}_n^{(2s)}$ are zero. Thus each individual bead produces stresslet flow shown in Fig. (2.1b). The velocities and tractions

are, therefore,

$$\mathbf{v}(\mathbf{R}_m + \boldsymbol{\rho}_m) = \dot{\mathbf{R}}_m + \mathbf{s}_m \cdot \boldsymbol{\rho}_m, \quad (3.1)$$

$$4\pi a^2 \mathbf{f}(\mathbf{R}_m + \boldsymbol{\rho}_m) = -\nabla_m U + 3\mathbf{S}_m \cdot \boldsymbol{\rho}_m, \quad (3.2)$$

where \mathbf{s}_m and \mathbf{S}_m are, respectively, the symmetric parts of the second-rank velocity and traction coefficients. The solution of the boundary integral equation, in the diagonal approximation, relates the unknown traction coefficient to the known value of the velocity coefficient

$$\mathbf{S}_m = -\frac{20\pi\eta a^3}{3} \mathbf{s}_m. \quad (3.3)$$

To complete the model, it is necessary to specify the orientation \mathbf{p}_n of the beads, and hence the principal axis of the stresslet, in relation to the filament conformation. Motivated by the experimental observation that molecular motors walking on microtubule tracks generate tangential stresses, we parametrize \mathbf{s}_m uniaxially, with its principal axis always parallel to the local tangent \mathbf{t}_m of the filament,

$$\mathbf{s}_m = s_0(\mathbf{t}_m \mathbf{t}_m - \frac{1}{3} \boldsymbol{\delta}). \quad (3.4)$$

The coefficient s_0 is positive for extensile stresses and negative for contractile stresses. Additionally, we assume that the activity is so large that the Brownian fluctuations make a negligible contribution to the dynamics. Active flow is balanced entirely by the filament elasticity. This leads to deterministic equations of motion for an active filament composed of non-motile beads,

$$\dot{\mathbf{R}}_n = \frac{1}{6\pi\eta a} \mathbf{F}_n^{int} + \sum_{m \neq n} \mathcal{F}^0 \mathcal{F}^0 \mathbf{G} \cdot \mathbf{F}_m^{int} + \frac{28\pi\eta a^3}{3} \sum_{m \neq n} \underbrace{\mathcal{F}^0 \mathcal{F}^1 \nabla \mathbf{G}}_{Active} \cdot \mathbf{s}_m. \quad (3.5)$$

These equations, without finite-sized corrections to the hydrodynamic flow, were first proposed in [86] and subsequently used in to study the dynamics of clamped active filaments [87].

Activity Number

Taking the ratio between the active and passive contribution in the Eq. 3.5, we can define a dimensionless measure of activity. Here it is the activity number \mathcal{A}_S , which can be cast in terms of rigidity parameter κ and length of the filament L as

$$\mathcal{A}_S = \frac{|S_0|}{|\mathbf{FL}|} = \frac{LS_0}{\kappa}. \quad (3.6)$$

With more modes of activity, there will be more activity numbers. These activity numbers can be derived alternatively by taking ratios of rates. For example, in d spatial dimensions, activity introduces a new rate $\Gamma_s = S_0/\eta L^d$ in addition to the rate of elastic relaxation $\Gamma_\kappa = \kappa/\eta L^{d+1}$ of the filament bending modes. The ratio of these two time scales yields, again, the activity number.

The activity number \mathcal{A}_S also measures the departure from equilibrium and the amount of energy that is injected into the fluid by the filament. We vary both the filament length and the activity number in studying the dynamics of the filament in $d = 3$ dimensions.

Fluid Flow

The flow produced by the filament is sum of contributions from the potentials and the activity,

$$\mathbf{v}(\mathbf{r}) = \sum_{n=1}^N \mathcal{F}^0 \mathbf{G} \cdot \mathbf{F}_n^{int} + \frac{28\pi\eta a^3}{3} \sum_{n=1}^N \underbrace{\mathcal{F}^1 \nabla \mathbf{G} \cdot \mathbf{s}_n}_{Active}. \quad (3.7)$$

3.3 Hydrodynamic instability

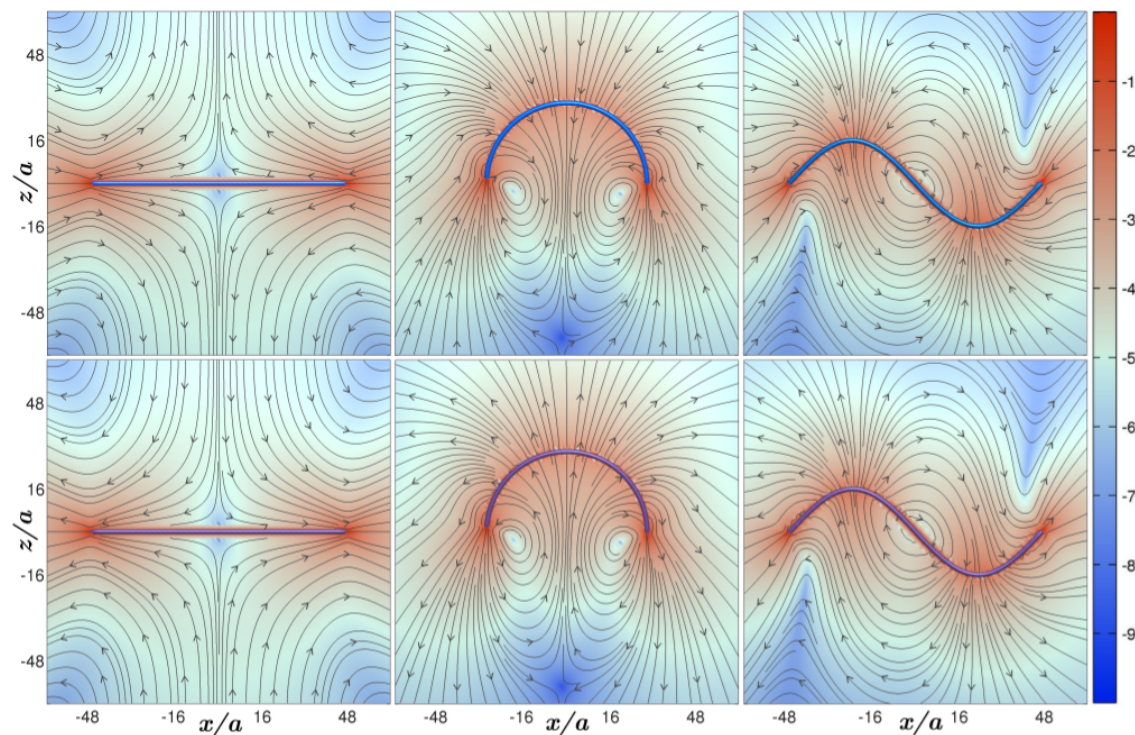


Figure 3.1: Streamlines of slow viscous flow around contractile (top row) and extensile (bottom row) minimally active filaments. Spontaneous flow in the linear conformation tends to compress contractile filaments and extend extensile filaments (first column). Both symmetric and antisymmetric transverse perturbations are suppressed in contractile filaments but enhanced in extensile filaments by the spontaneous flow (second and third columns). The latter leads to a linear instability in extensile filaments, when the elastic restoring force is no longer sufficient to counter the destabilizing tendency of the spontaneous flow.

The resultant flow is shown for three conformations, for both extensile and contractile filaments, in Fig (3.1). In the linear conformation, shown in the first column of Fig (3.1), the flow tends to compress contractile filaments and extend extensile filaments. The stationary length of the filament is then somewhat shorter in the contractile flow but somewhat longer in the extensile flow. In a symmetrically curved conformation, shown in the second column of Fig (3.1), the spontaneous flow tends to suppress curvature in the contractile filaments but tends to enhance it for extensile filaments. The suppression and enhancement are seen for anti-symmetrically curved conformations in the third column

of Fig (3.1). This shows that the interplay of flow and curvature is generally stabilizing for contractile filaments while it is destabilizing for extensile filaments. On dimensional grounds, a linear instability is expected when the filament length $L > l_A \sim \kappa/S_0$. In the remainder of the chapter, we shall focus only on extensile filaments and study the non-equilibrium stationary states that appear as a consequence of the linear instability.

3.4 Free and tethered filament

Our results are summarised in Fig. (3.2), which shows the non-equilibrium stationary states for both free filaments in panels (a) - (f) and for tethered filaments in panels (g) - (i). With the increase of activity, a linear instability appears in free filaments which leads to spontaneous symmetric curvature and an emergent autonomous motility, shown in panel (a). The conformation corresponds, roughly, to the first elastic eigenmode of the passive filament. With increasing amounts of activity, higher elastic eigenmodes appear through a series of bifurcations, shown in panels (b) - (f). Whenever the conformation is asymmetrical about the centre, the filament acquires a rotational component of motion. The higher elastic eigenmodes appear for smaller values of activity in longer filament, as is seen by comparing panel (c) with panels (e) and (f). Although the system is three-dimensional, filament motion is planarly stable in a plane that is determined by the initial condition. This rich dynamics ([online-movie](#)) and non-equilibrium steady states we have found are remarkably similar to an experiment on an isolated axoneme [28].

Tethering the filament at one end restricts translation and thus the energy transduction from the activity is fed into rotational and oscillatory states ([online-movie](#)). Beyond the threshold activity of \mathcal{A}_{S1} , a tethered filament rotates around the pivot, panel (g), in a plane that is chosen by the initial condition. Further energy injection leads to flagella like beating in a plane, shown in panel (h). The highest value of activity studied is shown in panel (i), where a conformation similar to the panel (d) appears but is now constrained

by the pivot and forced to rotate while maintaining conformation. With the increase in filament length and activity, we expect higher elastic eigenmodes to appear, and the filament either rotates or oscillates under the constraint of the tether.

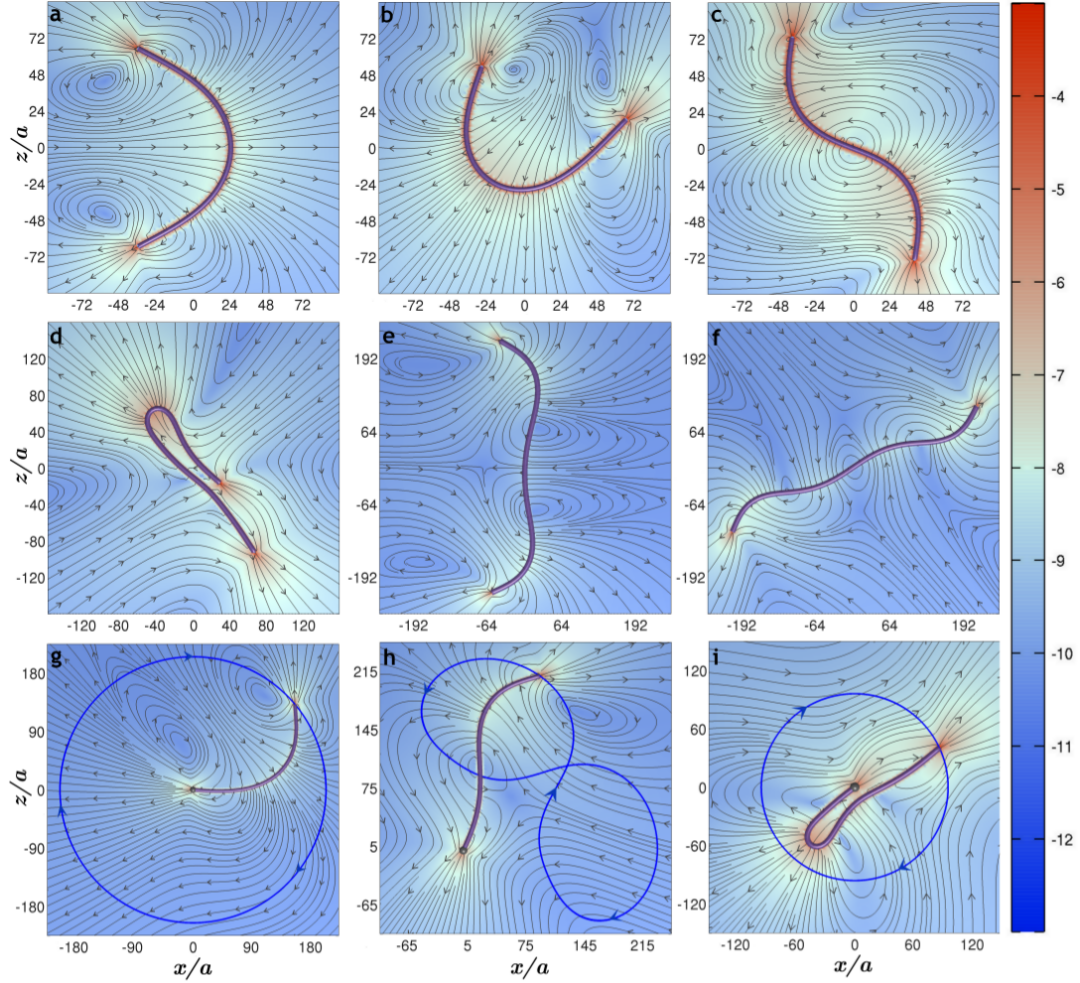


Figure 3.2: Non-equilibrium stationary states of a free, (a) - (f), and tethered, (g) - (i), minimally active filament. The figures show the filament conformation and the streamlines of slow viscous flow produced by the activity, where the background is coloured by the logarithm of the magnitude of the velocity. Free filament steady states are shown for three lengths with increasing values of activity \mathcal{A}_S . For short filaments ($N = 48$) increasing activity produces the three non-equilibrium steady states in (a) - (c), corresponding to the excitation of the first two elastic eigenmodes and their linear combinations. As the filament length is increased ($N = 80$ and $N = 128$) higher elastic eigenmodes appear with increasing amounts of activity in (d) - (f). (online-movie). Tethered filament steady states are shown for a fixed length ($N = 64$). Increasing activity produces a rotating steady state in (g), which bifurcates into an oscillating steady state in (h), with a return to a distinct rotating steady state in (i). (online-movie)

The dynamics of the centre of mass follows from summing the equation of motion over all beads. The contribution from internal spring forces vanishes, and on approximating the active flow by its contribution from the nearest neighbours, an approximate equation is obtained that relates the centre of mass motion to the filament curvature and the activity,

$$\mathbf{V}_{CM} \simeq -\frac{s_0}{4\pi\eta b_0} \langle \chi \hat{\mathbf{n}} \rangle = \chi. \quad (3.8)$$

In Fig. (3.3a), we compare the numerically computed values of the centre of mass velocity with the curvature vector χ defined above. There is a surprisingly good agreement between the two, indicating that principal effect of the non-local active flow can be expressed locally as a tendency to promote curvature.

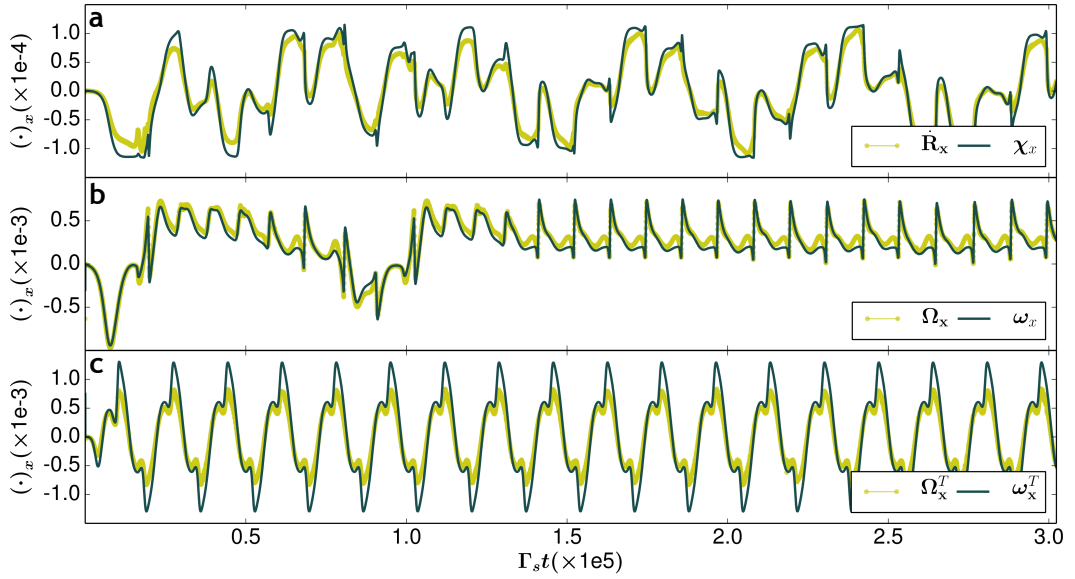


Figure 3.3: Comparison of filament kinematics and curvature dynamics. In (a) the x -component of the centre of mass velocity is compared with the x -component of the scaled average curvature vector (see Eq. 3.8) for a free filament. In (b) the x -component of the mean angular velocity about the centre of mass is compared with the scaled average first moment of the curvature vector (see Eq. 3.9). In (c) the same comparison is made for a tethered filament, with origin at the point of pivot. The comparison shows that the filament motion is strongly correlated with dynamics of activity induced curvature.

A similar relation holds for the angular velocity about the centre of mass,

$$\boldsymbol{\Omega}_{CM} \simeq -\frac{s_0}{8\pi\eta b_0} \langle \boldsymbol{\nu} \hat{\mathbf{n}} \times (\mathbf{R} - \mathbf{R}_{CM}) \rangle = \boldsymbol{\omega}. \quad (3.9)$$

and the previous comparison is repeated for both free and tethered filaments in Fig (3.3b) and Fig (3.3c). For tethered filaments, the pivot point, and not the centre of mass, is used to compute cross products, and the activity-dependent prefactor is two times smaller. This suggests that effective, local equations of motion may be accurate for describing some aspects of the dynamics of active filaments.

3.5 Clamped filament

Here, we present results of numerical simulation of an active filament, when it is clamped at one end. In this boundary condition, it exhibits a variety of spontaneous beating phenomena in a three-dimensional fluid.

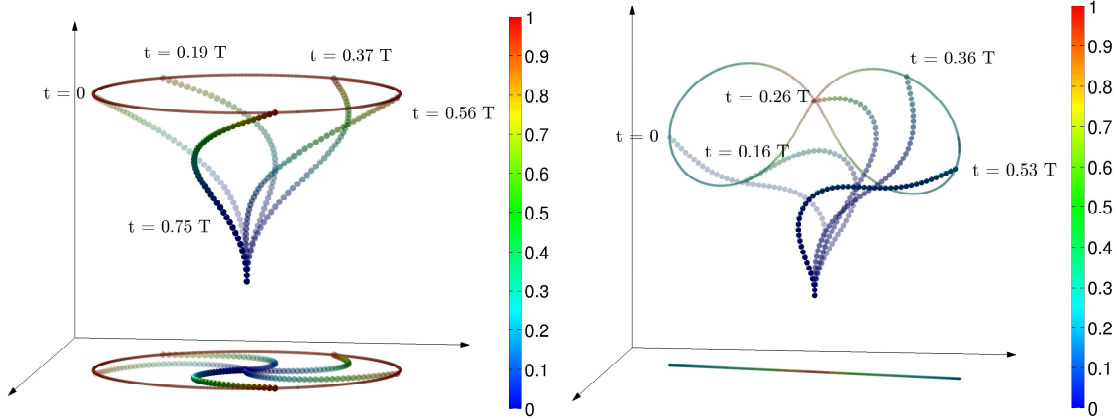


Figure 3.4: Biomimetic oscillations of the clamped filament plotted at different times over an oscillation period T . In (a) we see rigid aplanar corkscrew rotation for $\mathcal{A}_S = 25$ while in (b) we see flexible planar beating for $\mathcal{A}_S = 50$. The colour of the beads, as well as the trace of the tip, correspond to individual instantaneous monomer speeds. The colourbars are normalised by the maximum speed.

Spontaneous oscillations: A transverse perturbation breaks flow symmetry about the

central line of the filament resulting in a net flow in the direction of the perturbation. The destabilising effect of the hydrodynamic flow is countered by the stabilising effect of linear elasticity for activity numbers $\mathcal{A} < \mathcal{A}_{S1}$ but leads to a linear instability for $\mathcal{A} > \mathcal{A}_{S1}$. This instability produces filament deformations which are ultimately contained by the non-linear elasticity producing autonomously motile conformations [86, 88]. Here, the additional constraint imposed by the clamp transforms the autonomously motile states into ones with spontaneous oscillations.

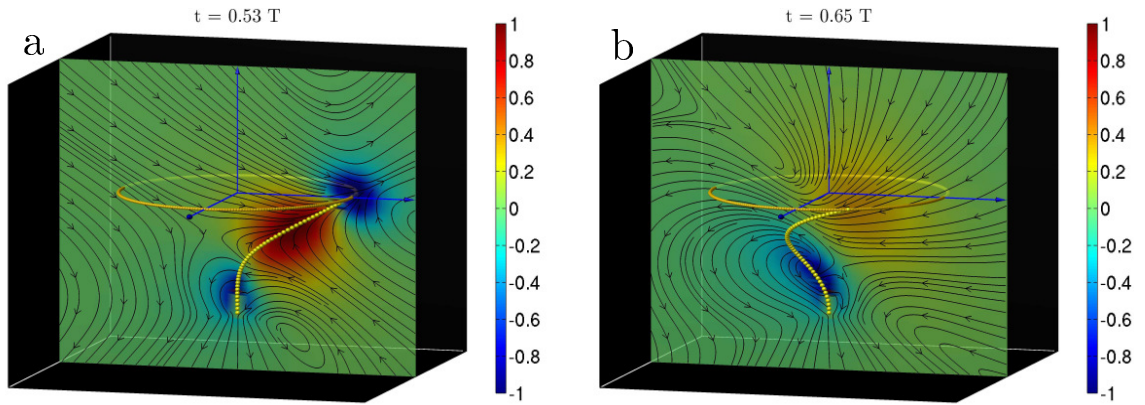


Figure 3.5: Flow fields of rigid aplanar corkscrew rotation at two different instances of rotation. The colour indicates the signed magnitude of the velocity field perpendicular to the plane normalised by its maximum.

Numerical simulations of Eq. (3.5) reveal two distinct oscillatory states (Figs. 3.4a, 3.4b). The first of these, seen in the range $\mathcal{A}_{S1} < \mathcal{A}_S < \mathcal{A}_{S2}$, is a state in which the filament rotates rigidly in a corkscrew-like motion about the axis of the clamp ([online-movie](#)). This rotational corkscrew motion is reminiscent of prokaryotic flagellar beating [137, 138]. We show this motion in Fig (3.4a) over one time period of oscillation together with the projection of the filament on the plane perpendicular to the clamp axis. A section of the three-dimensional flow in a plane containing the clamp axis is shown in Fig (3.5a and 3.5b). The net flow points in the direction opposite to the filament curvature and the entire flow pattern co-rotates with the filament.

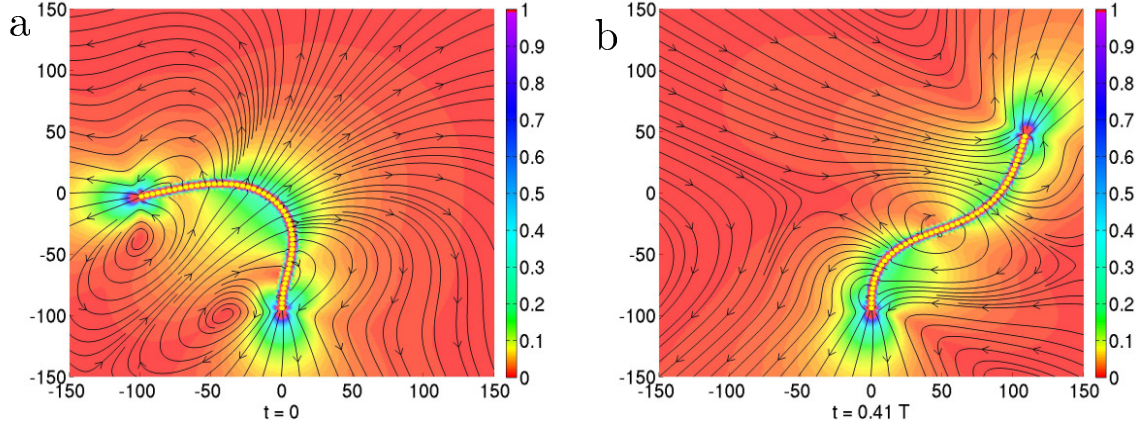


Figure 3.6: Flow fields of flexible planar beating at two instants of the oscillation cycle. The colour indicates the magnitude of the velocity in the plane normalised by its maximum.

In the second state, seen for $\mathcal{A}_5 > \mathcal{A}_{52}$, the filament beats periodically in a two-dimensional plane containing the axis of the clamp, with waves propagating from the clamp to the tip ([online-movie](#)). This flexible beating is reminiscent of eukaryotic flagellar motion [58, 17, 27, 135, 139]. We show this motion in (Fig. 3.4b) over one time period of oscillation together with the projection of the filament on the plane perpendicular to the clamp axis. The projection is now a line, showing that motion is confined to a plane. A section of the three-dimensional flow in the plane of beating is shown in Fig (3.6a and 3.6b). Two distinct types of filament conformations of opposite symmetry are now observed, corresponding to the different parity of the conformation with respect to the perpendicular bisector of the line joining the two end points. In the *even* conformation (Fig 3.6a), the flow points in the direction opposite to the curvature as in the corkscrew state. However, in the *odd* conformation (Fig 3.6b), the flow has a centre of vorticity at the point of inflection of the filament. This centre of vorticity moves up the filament and is shed at the tip at the end of every half cycle.

Scaling of time period and Amplitude. The physical parameters determining the time period T of the oscillatory states are the active stresslet S_0 , the bending modulus κ , the fluid viscosity η and the filament length L . Remarkably, variations of T in this

four-dimensional parameter space collapse, when scaled by the active relaxation rate $\Gamma_S = S_0/\eta L^3$, to a one-dimensional scaling curve of the form $L^{-\alpha} f(\mathcal{A}/L^\beta)$. We show the data collapse at fixed L and varying relative activity S_0/κ in Fig (3.7a) while the scaling with system size is shown in Fig (3.8a). Our best estimates for the exponents, obtained from Bayesian regression, are $\alpha = 1.3$ and $\beta = -1.2$ (Fig 3.8a). Qualitatively, at a fixed relative activity, the oscillation frequency decreases with increasing L , while at a constant L the oscillation frequency increases with increasing relative activity. This is in agreement with a simple dimensional estimate of the time period $T \sim \eta L^3/S_0$. For active beads with a stresslet of $S_0 \sim 6 \times 10^{-18} Nm$ in a filament of length $L \sim 100 \mu m$, our estimate of the time period gives a value of 170s, which agrees in order of magnitude with experiment [45]. The amplitude of oscillation A obeys a similar scaling relation with $\alpha = -1.46$, $\beta = -1.2$ (Fig. 3.7b, main panel). At fixed relative activity, A increases with increasing L , while at fixed L , it increases and then saturates at large relative activity. The mean amplitude in the planar beating state is marginally smaller than in the corkscrew rotating state (Fig.3.7b, inset).

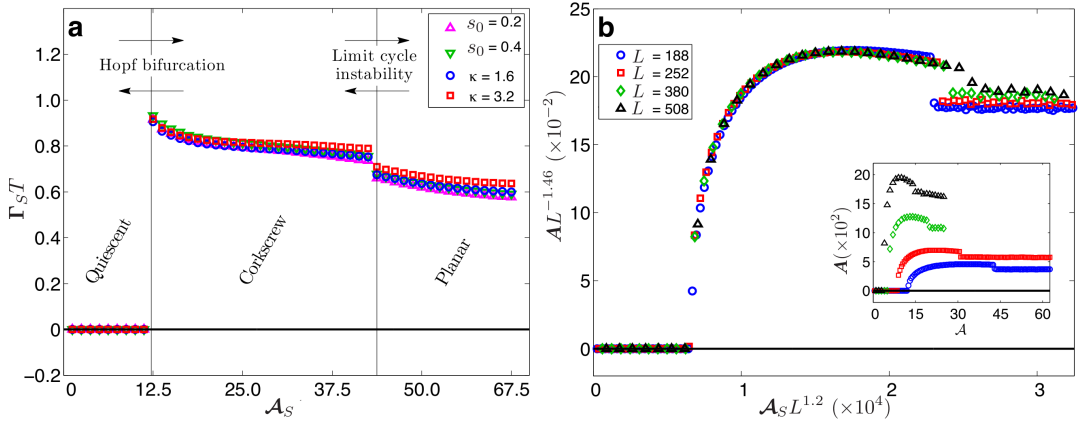


Figure 3.7: Variation of the scaled timeperiod $\Gamma_S T$ of filament beating with \mathcal{A}_S plotted for various values of κ and s_0 with $L = 188$, and (b, main panel) variation of the scaled amplitude $L^{-1.46} A$ with \mathcal{A}_S plotted for various lengths L with $\kappa = 1.6$. In (a) we show the appearance of spontaneous oscillations in the filament at $\mathcal{A}_S \sim 12.5$ corresponding to a rigid corkscrew rotation, followed by a transition at $\mathcal{A}_S \sim 45$ to flexible planar beating. In (b, inset) we show the increase in the unscaled amplitude with length.

The transition from aplanar to planar state can be separated out easily by computing convex hull or writhe of the filament trajectory. In the aplanar state the convex hull is nonzero but become zero in the planar state. In the first panel of the Fig (3.9), we show this transition through scaled convex hull with the increase of activity. Transitions for different lengths of the filament can be fitted into a single master curve using a Bayesian estimate.

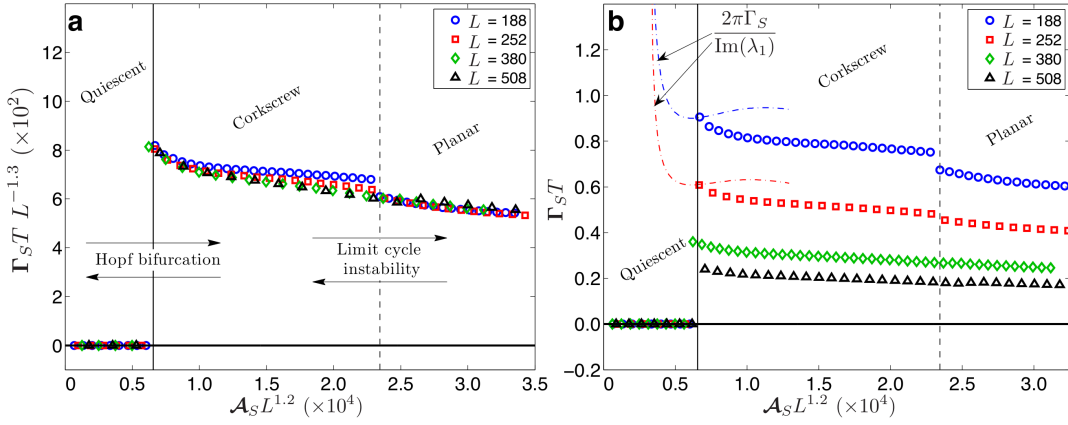


Figure 3.8: Variation of the non-dimensionalised time period $\Gamma_S T$ with activity number \mathcal{A}_S (a) with and (b) without L scaling, obtained from numerical simulations. The dashed lines in (b) represents the variation of $2\pi\Gamma_S / \text{Im}(\lambda_1)$ with \mathcal{A} for $L = 188$ and $L = 252$, data obtained from LSA. The rescaled plot of $\Gamma_S T$ in (a) shows that its variations are well captured by a scaling form $L^{-\alpha} f(\mathcal{A}_S / L^\beta)$, with $\alpha = 1.3$ and $\beta = -1.2$ estimated using Bayesian regression. The unscaled results in (b) show that the time period is of the order of the active timescale Γ_S^{-1} . The LSA estimate of the time period and the simulation result agree very well near the Hopf bifurcation point, and, predictably, deviates in the nonlinear regime.

Scaling of critical activities. The critical activities scale as $\mathcal{A}_{S1} = L^{-1.2}$ and $\mathcal{A}_{S2} = L^{-1.1}$, obtained from a Bayesian parameter estimation of data shown in Fig (3.9b). The critical values depend only on the ratio S_0 / κ , and not on S_0 and κ individually, as is clearly seen in Fig (3.7a).

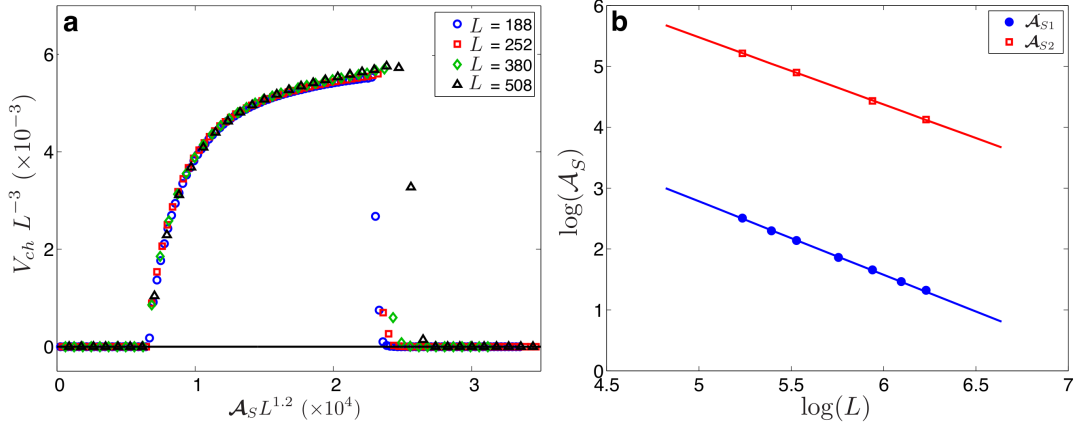


Figure 3.9: Variation of the rescaled volume of the convex hull V_{ch} of the filament with \mathcal{A}_S showing the transition between aplanar rotations in the regime $\mathcal{A} < \mathcal{A}_{S2}$ and planar oscillations in the regime $\mathcal{A} > \mathcal{A}_{S2}$. (b) Variation of the transition points \mathcal{A}_{S1} and \mathcal{A}_{S2} with L exhibiting a scaling relation $\mathcal{A}_S \sim L^\beta$. Using Bayesian regression, we estimate $\beta = -1.2$ for \mathcal{A}_{S1} and $\beta = -1.1$ for \mathcal{A}_{S2} , the different values responsible for the imperfect data collapse near the second transition. Symbols represent simulation data while solid lines represent the Bayesian estimate.

3.6 Linear stability analysis

To better understand the linear instability which is expected from the flows shown in Fig 3.1, we perform a stability analysis of the equations of motion, about the linear conformation. Taking the equations of motion to represent a dynamical system, $\dot{\mathbf{R}}_n = f(\mathbf{R}_1, \mathbf{R}_2, \dots, \mathbf{R}_n)$, we compute the Jacobian $\mathbf{J} = -\nabla_n f \Big|_{\mathbf{R}_n^0}$ at the stationary state with linear conformation \mathbf{R}_n^0 . The linearised dynamics, then, is

$$\delta \dot{\mathbf{R}}_n = \mathbf{J} \cdot \delta \mathbf{R}_n. \quad (3.10)$$

We numerically compute the eigenvalues of this stability matrix as a function of activity \mathcal{A}_S for both free and tethered filaments. To evaluate the importance of non-local hydrodynamic interactions, we also compare the eigenvalues for the dynamics in which all non-local (that is $m \neq n$) terms are deleted. The results are shown in Fig (3.10a) and Fig (3.10b) for free and tethered filaments, respectively.

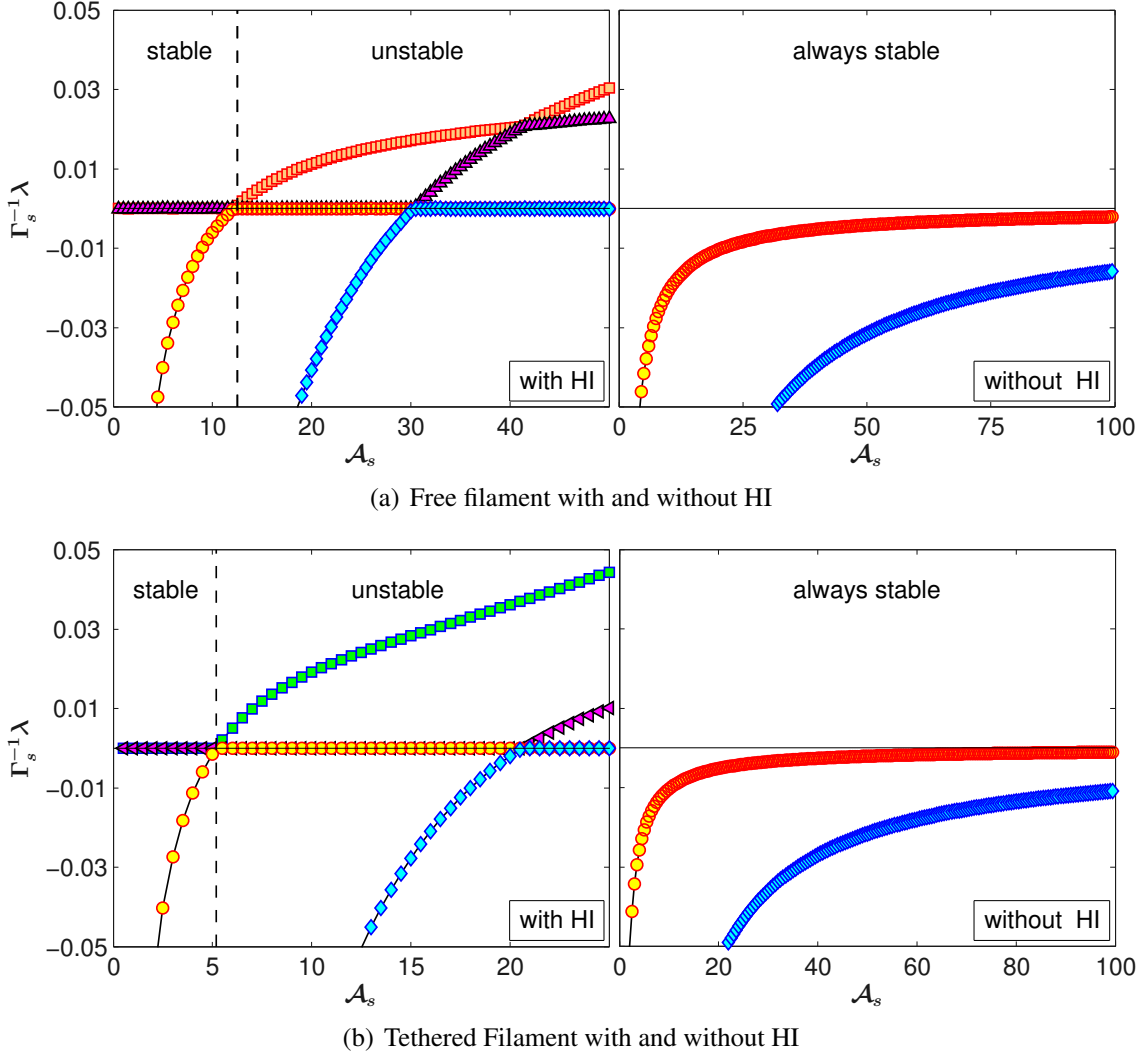


Figure 3.10: Variation of the largest non-zero eigenvalues of the stability matrix, \mathbf{J} , plotted against activity number, \mathcal{A}_S , for a free filament in (a) and a tethered filament in (b). In each case, the eigenvalues are computed including full hydrodynamic interactions (HI) (left panels) and neglecting all non-local hydrodynamic contributions (right panels). The eigenvalues remain negative, for all values of \mathcal{A}_S in a large range, when hydrodynamic interactions are neglected. Hydrodynamic interactions, therefore, are essential for the instability of the linear conformation and the bifurcation to dynamical steady states, signalled by the positive eigenvalues in each of the left panels.

Free and tethered filament. We see that the largest eigenvalue becomes positive at $\mathcal{A}_S \sim 12$ for free filaments and $\mathcal{A}_S \sim 5$ for tethered filaments. The bifurcation is thus a simple instability. The first eigenmode instability flows to the symmetrically curved conformation shown in Fig 3.10(a). Instabilities of the higher eigenmodes leads, the first

of which is visible in Fig. 3.2a at $\mathcal{A}_S \sim 40$, produces the more complicated states shown in panels (b) - (g) of Fig 3.2. The presence of the tether decreases the threshold value of the activity at which the instability occurs to $\mathcal{A}_S \sim 5$, but the sequence of instabilities remains identical.

Subsequent bifurcations with increasing values of activity are expected to have a more complicated character, as the stationary states are typically limit cycles. The numerical study of limit cycle instabilities is considerably more involved than that of time-independent stationary states. We shall explore this aspect of the dynamics of active filaments in a future study.

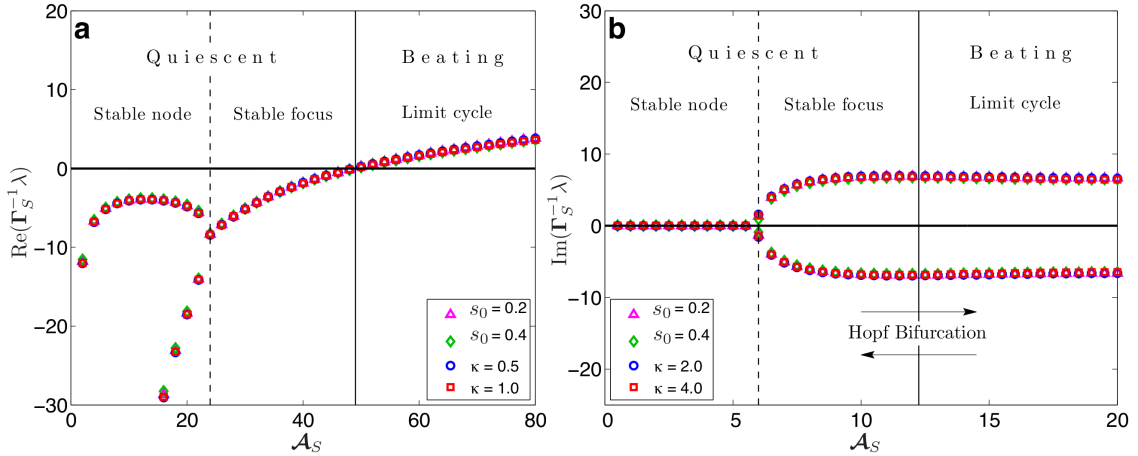


Figure 3.11: Variation of the scaled (a) real and (b) imaginary parts of the largest eigenvalues with \mathcal{A}_S , plotted for various values of κ and S_0 with $L = 188$. Data is obtained from a linear stability analysis (LSA) of the filament model. The largest eigenvalue pairs converge at $\mathcal{A}_S \sim 6$ and become complex with negative real parts, signalling the transition from stable node to stable focus. $\text{Re}(\lambda)$ become positive at $\mathcal{A}_{S1} \sim 12.5$ while $\text{Im}(\lambda)$ varies smoothly with \mathcal{A}_S , indicating a Hopf bifurcation into a limit cycle.

Clamped filament. In the absence of activity, $\mathcal{A}_S \sim 0$, all eigenvalues of the Jacobian are real and negative and the filament has an overdamped relaxation to equilibrium. With increasing \mathcal{A}_S , the two largest real eigenvalue pairs approach, converge, and become complex conjugate pairs ([online-movie](#)). This corresponds to a transition from a stable node to a stable focus where the response changes from being overdamped to under-

damped. The analysis reveals that the balance between hydrodynamic flow and linear elasticity has a non-monotonic variation. While the general trend is towards the slower relaxations with increasing \mathcal{A}_S corresponding to the greater relative strength of the hydrodynamic flow, this is reversed in a small window of activity where the increasing activity produces faster relaxations. This can be clearly seen in Fig. 3.11(a) and Fig. 3.12(a), where the rate of relaxation is given by the magnitude of the real part of the largest eigenvalue. With further increase of \mathcal{A}_S the complex eigenvalues approach the imaginary axis monotonically, crossing them at a critical value \mathcal{A}_{S1} (Fig. 3.12a, Figs. 3.11a and 3.11b). Through this supercritical Hopf bifurcation, the stable focus flows into the limit cycle corresponding to the corkscrew rotation. The value of \mathcal{A}_{S1} obtained from the linear stability analysis is in perfect agreement with that obtained from numerical simulation. As with the time-period and amplitude, the eigenvalue λ of the Jacobian obey scaling relations $\lambda \Gamma_S^{-1} = L^{-\alpha} f\left(\frac{\mathcal{A}_S}{L^\beta}\right)$ with $\alpha = 1.2$ and $\beta = -1.2$.

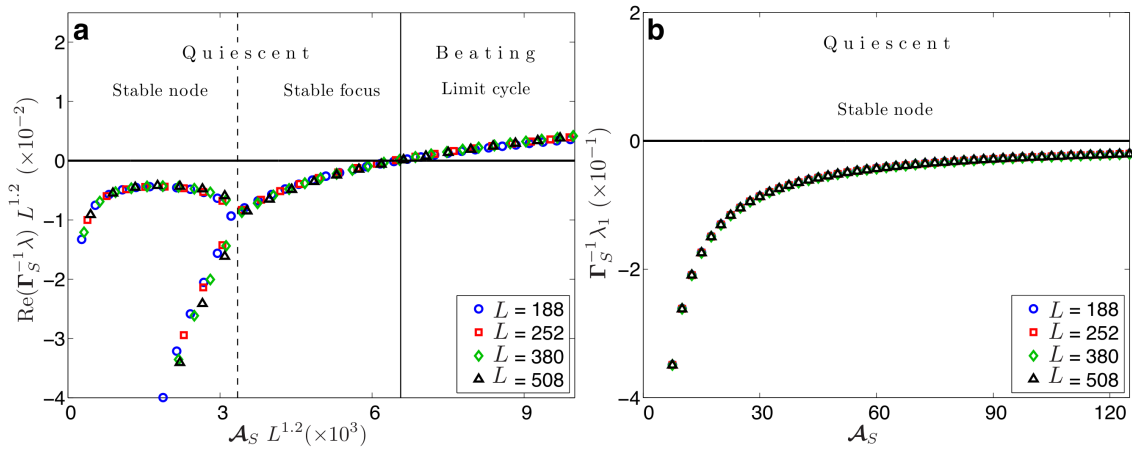


Figure 3.12: Variation of the largest scaled eigenvalues of the stability matrix (a) including HI and (b) excluding HI. In (a) we see the transition from a stable node to a stable focus followed by a supercritical Hopf bifurcation from quiescence to a limit cycle. In (b) we see only a stable quiescent state. In the absence of HI the eigenvalue scaling is completely determined by \mathcal{A}_S . Comparing (a) and (b) it is clear that hydrodynamic instabilities due to HI are the main mechanism for spontaneous oscillations. (a) also shows that the rate of relaxation (given by the magnitude of the real part of largest eigenvalue) to the steady state before the bifurcation decreases as we approach the bifurcation from below.

Importance of HI. Remarkably, there is no instability in the same range of activity, when hydrodynamic interactions are ignored, as shown in the right panels of Fig (3.10). We find that all eigenvalues remain real and negative for activity numbers corresponding to an order of magnitude greater than \mathcal{A}_{S1} , reflecting the stability of the quiescent state in the absence of HI (Fig. 3.12b, second column of 3.10). Thus, non-local active hydrodynamic flow is essential to produce the instabilities and the non-equilibrium stationary states reported above.

3.7 Discussion and conclusion

Through our work, we demonstrate that our minimal model of active filament can produce spontaneous motion and oscillations in the absence of any external driving, of the kind found in complex biological structures such as axoneme [28], eukaryotic spermatozoa [27] and in the assembly of motors and microtubules [23].

Moreover, we predict similar kind of oscillation can be found in a chain of tri-metallic catalytic nanorods [140, 141]. We emphasise that an experimental realisation of our system requires neither external actuation nor self-propulsion. The only chemo-mechanical requirement is that the active beads produce dipolar flows in the fluid. This makes them an attractive candidate for biomedical applications like targeted drug delivery. Our detailed prediction for the spatio-temporal dynamics of the hydrodynamic flows can be experimentally verified using particle imaging velocity [142].

Further inclusion of additional self-propulsion mode, $V^{(3t)}$ can reproduce motions and different steady states of a chain of self-propelling active beads for instance of synthetic catalytic nanorods [143, 144, 145, 146].

Previous work on bead-spring models of active filaments have focused on three distinct mechanisms of activity. In the earliest work of Jayaraman et al [86], activity arises from the hydrodynamic flow of the active beads. In that work, the equations of motion

for filament dynamics in three dimensions contained contributions from the leading order hydrodynamic flow due to stresslets and degenerate quadrupoles. A detailed study and all results were given for non-motile active beads, thus ignoring the velocity quadrupoles. In subsequent work, Chellakot et al [89] studied a chain of motile active beads subject to Brownian motion in two dimensions but ignored all non-local hydrodynamic effects, both passive and active. In related work, Jiang and Hou [91] studied a chain of passive beads, subject to forces of non-equilibrium origin, directed along the filament tangent. In their model, both passive hydrodynamic flow and hydrodynamically correlated Brownian motion is included in three dimensions, but the active flow is absent. Remarkably, in spite of these differences between the models, they yield a broadly similar phenomenology : linear instabilities, spontaneous motion, and oscillatory states.

To understand why this might be, it is best to situate all the previous models within the equations of motion presented here. The model studied in detail by Jayaraman et al [86] is obtained when self-propulsion velocities, \mathbf{V}_n^A , are set to zero, only the dipolar contribution to active flow is retained, and finite-sized corrections to hydrodynamic flow as well as Brownian motion are neglected. The model of Chellakot et al [89] is obtained when the self-propulsion velocity is directed along the axis \mathbf{p}_n , $\mathbf{V}_n^A = v_s \mathbf{p}_n$, and this axis is itself determined from the balance of a restoring and Brownian torques. This requires the angular velocity to be retained as a dynamical variable and all off-diagonal contributions to mobility and propulsion matrices to be ignored. Finally, the model of Jiang and Hou [91] is obtained by ignoring all active components of flow, $\mathbf{v}^A = 0$, but representing the force on the beads as $\mathbf{F}_n = -\nabla_n U + \alpha \mathbf{t}_n$, as the sum of contributions from the potentials and an unspecified non-equilibrium source. The common feature of all these models is that they produce motion in the direction of the curvature. This arises from the non-local hydrodynamic flow in the model of Jayaraman et al, and from the local contributions due to self-propulsion and non-equilibrium activity in the models of Chellakot

et al and Jiang et al respectively. The present work shows that a phenomenology beyond curvature instabilities remains to be explored. In particular, torsional instabilities, possible with self-rotating active beads that are unhindered by torsional potentials, are likely to yield further surprises in the dynamics of active filaments.

We have neglected, here, the active self-propulsion and set \mathbf{V}^A to zero. The motion of an active filament chain composed of self-propelling particles will be dominated by the self-propulsion terms which are all $\mathcal{O}(1)$, and the hydrodynamic interactions that have been studied here in detail will be subdominant. Such a model, especially in the case where the self-propulsion axis is aligned to the filament tangent, is expected to show the kinds of transition between translational and rotational states observed in the work of Jiang and Hou [91].

As a final remark, we draw attention to the similarity between the instabilities reported here and the convective instability by active stress studied in the pioneering work of Finlayson and Scriven [147].

External fields: sedimentation of an active filament

The conformational dynamics of an active filament is studied under a uniform external field. The external field, coupled with the activity and the hydrodynamic interaction, drives instabilities in directions *both* the parallel and the perpendicular to it. Introducing two dimensionless measures, the activity number \mathcal{A}_S and the sedimentation number \mathcal{S} , we demarcate regions of stable conformations and the transitions between them. We compare this with the known results for the conformational states of a steadily sedimenting passive filament. Our findings can be verified in the sedimentation of active biological filaments and chains of phoretic beads.

4.1 Introduction

A standard way of characterising soft matter is by measuring its response to external fields. Unlike phases composed of rigid molecules where external fields perturb supramolecular organization, in phases of flexible filamentous molecules, both the conformation of the polymer and supramolecular organization are perturbed by the external field. It is of interest, therefore, to first understand how a single filament deforms in response to an external field. This is the task which set ourselves to do in this chapter.

Previous studies incorporating the external field and hydrodynamic interaction show rich dynamical behaviours and conformational changes in slender bodies [148, 149, 150, 151, 152, 153, 154]. We first reproduce results for the settling of passive filaments

[149, 151, 152, 153, 154] as the zero activity limit of our formalism. We demonstrate that during the settling of a passive filament the non-local hydrodynamic force varies over different parts of the filament, which in turn determines the dynamical steady states as well as metastable states. During the metastable state, the filament takes the conformation that looks like a W. This marginally stable state ends up in a more stable state by a spontaneous release of elastic stress. We further show that, the lifespan of the metastable state decreases with the increase of difference between mean power dissipation in these two states. Other non-linear steady states are also found at high sedimentation number \mathcal{S} , which is a measure of the strength of external field to the elasticity of the filament. In the presence of internal activity the dynamic balance between fluid mediated force, external force and restraining elastic forces of the body get modified and consequently, a series of new steady states appear. These different states can be categorised by their conformational and dynamical features. Interestingly, similar kind of steady conformations can arise due to different dynamic balance. We further demarcate different regions of the steady conformations, in the two-dimensional phase space of activity number $\mathcal{A}_\mathcal{S}$ and sedimentation number \mathcal{S} and compute their dynamic response coefficients.

4.2 Model description

Including an additional body force to our minimal model of active filament, we obtain the update equation. The origin of this additional body force could be due to gravity, magnetic field or centrifugal force inside a centrifuge. Here for simplicity, we consider gravity.

Equation of motion: By considering additional external force to the Eq. (2.2), we

obtain

$$\dot{\mathbf{R}}_n = \frac{1}{6\pi\eta a}(\mathbf{F}_n^e + \mathbf{F}_n^{int}) + \sum_{m \neq n} \mathcal{F}^0 \mathcal{F}^0 \mathbf{G} \cdot (\mathbf{F}_m^e + \mathbf{F}_m^{int}) + \frac{28\pi\eta a^3}{3} \sum_{m \neq n} \underbrace{\mathcal{F}^0 \mathcal{F}^1 \nabla \mathbf{G} \cdot \mathbf{s}_m}_{\text{Active}}. \quad (4.1)$$

where η is the viscosity of the fluid, a is the radius of the individual beads.

Sedimentation number

Along with activity number \mathcal{A}_S , a dimensionless number can easily be derived by taking the ratio of internal elastic force and applied external force one. This is the sedimentation number \mathcal{S} . It can also be derived easily from the force balance equation presented in Eq. 2.21, by taking the ratio between external force and internal body force.

$$\mathcal{S} = \frac{|\mathbf{F}^e|}{|\mathbf{F}^{int}|} = \frac{L^2 |\mathbf{F}^e|}{\kappa} \quad (4.2)$$

where κ is the rigidity parameter and L is the length of the filament.

4.2.1 Hydrodynamic forces

Fluid flow: The fluid flow around the active bead, subject to external forcing can easily be computed by considering relevant modes. In this study, the fluid flow is due to contribution of external driving, elastic force of the body and internal apolar activity. Combining these we get,

$$\mathbf{v}(\mathbf{r}) = \sum_{n=1}^N \mathcal{F}^0 \mathbf{G} \cdot (\mathbf{F}_n^e + \mathbf{F}_n^{int}) + \frac{28\pi\eta a^3}{3} \sum_{n=1}^N \underbrace{\mathcal{F}^1 \nabla \mathbf{G} \cdot \mathbf{s}_n}_{\text{Active}}. \quad (4.3)$$

The resultant fluid flow around a settling passive bead and active beads are shown

in the Fig (4.1). In (a) the flow is due to Stokeslet term and in (b) and (c) the flows are combinations of Stokeslet and apolar activity mode, stresslet due to nonzero $\mathbf{V}^{(2s)}$ (b extensile and c contractile). Clearly, the activity modifies the fluid flow around the bead and consequent fluid-mediated hydrodynamic forces.

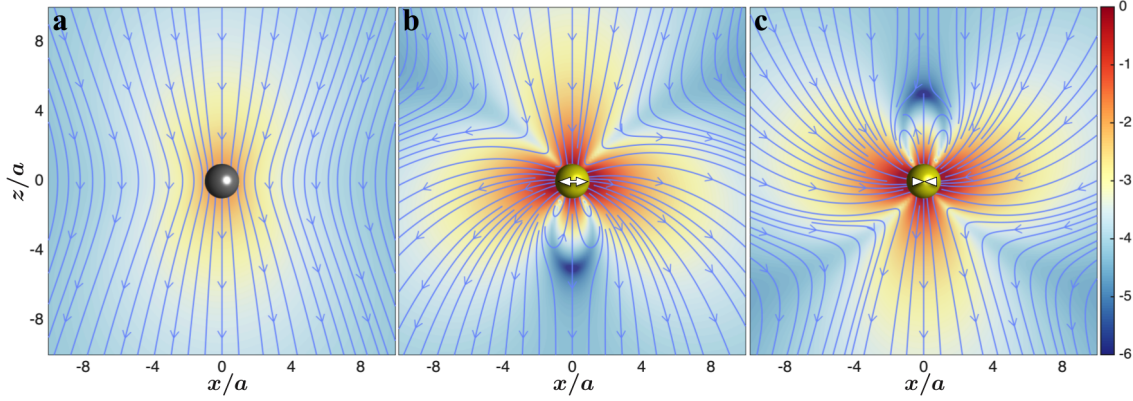


Figure 4.1: Fluid flow around a passive (a) and active (extensile (b) and contractile (c)) beads under uniform external field. The background is pseudo-coloured with the logarithm of the magnitude of the velocity in the plane normalised by its maximum, showing the variation of strength of the fluid flow.

The hydrodynamic force on active beads in a suspension can be computed from Eq. 2.19, by computing the resistance tensors γ . These resistance tensors can be computed with high accuracy by iterative methods [110]. On n -th bead, the hydrodynamic force is

$$\mathbf{F}_n^H = \underbrace{-\gamma_{nm}^{TT}(\{\mathbf{R}_i\}) \cdot \mathbf{V}_m}_{\text{passive}} - \underbrace{\gamma_{nm}^{(T,2s)}(\{\mathbf{R}_i\}) \cdot \mathbf{V}_m^{(2s)}(\{\mathbf{p}_i\})}_{\text{Active}}, \quad i \in \{1, \dots, N\}. \quad (4.4)$$

The complex coupling between conformation of the filament, external driving and internal activity is quite apparent in this equation. The expression for the force depends on the conformation of the filament, defined by the locations of all the beads \mathbf{R}_i , which determine the local tangent \mathbf{p}_i and which, in turn, determine the principal axes of the

activity modes $\mathbf{V}_m^{(2s)}$. It is the dynamic balance of the sum of the passive and active forces above with the internal elastic and external gravitation force that determines the stationary states of the filaments. Since the external force is conformation-independent in this case, the above two forces must sum, upto a constant, to the local elastic force.

4.3 Sedimentation of a passive filament

In this section, we study the dynamics of passive filaments from our general formulation of active slender bodies under external field by setting the active contribution to zero. We first reproduce the steady states found earlier [149, 151, 152, 153, 154] and discuss the results from the viewpoint of conformation dependent hydrodynamic force. All the steady and metastable states and their dynamics can be completely understood from this point of view. We conclude the section, with a new finding, a spinning aplanar steady state.

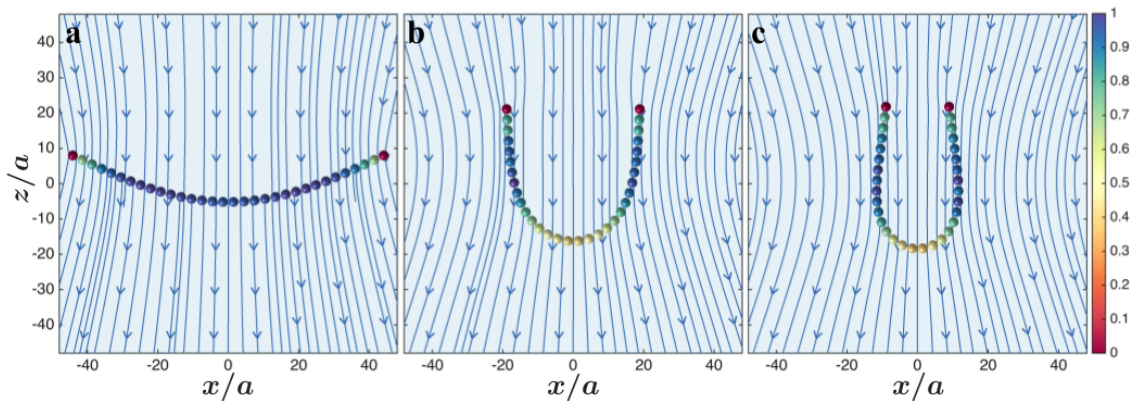


Figure 4.2: Planar steady state conformations of the filament, with increase of sedimentation number \mathcal{S} . The colour on the beads presents the variation of fluid mediated hydrodynamic force. During sedimentation of passive filament, the end points of the filament always have the minimal hydrodynamic force, and settle slower than the middle part, giving rise to V, U and horse-shoe shapes.

4.3.1 Planar steady states

At very small sedimentation number \mathcal{S} , the filament bends slightly in the middle and falls staying in a conformation that resembles a V . Initially, with the increase of the strength of the external field, the curvature in the filament increases, to more resemble an U , but after a certain threshold, the filament first reaches to a metastable steady state resembling a W which relaxes to the stable state horse-shoe like shape. All these planar steady states have been reported in earlier studies [149, 153, 152].

In the Fig (4.2), we have shown the steady states in the planar sedimentation, the fluid flow around its periphery and normalised hydrodynamic forces on different monomers. The many body force on the beads crucially depends on the shape of the filament. Approximately, at low sedimentation number, the hydrodynamic force at the middle is more than the edge, whereas, at moderate and high activity, the hydrodynamic force at the middle is lower than the ones, situated at the edges. In passive sedimentation, the hydrodynamic force on the last beads is always found to be lowest. Clearly, the location where the hydrodynamic force is least is where the elastic force must be the greatest, since their sum is the constant gravitational force. This explains why the curvature of the filament is greatest along the central regions of the filament. This transparent explanation has not been made explicit in previous studies.

4.3.2 Transient and metastable states

In the above, the stationary state deformation is a single-valued function of the sedimentation number: for any value of \mathcal{S} there is one and only one dynamically accessible long-lived conformation. In contrast, as the sedimentation number is increased, the stationary state deformation becomes a multi-valued function of \mathcal{S} : a series of dynamical states, with distinct distributions of lifetimes are possible for any given value of the sedimentation number.

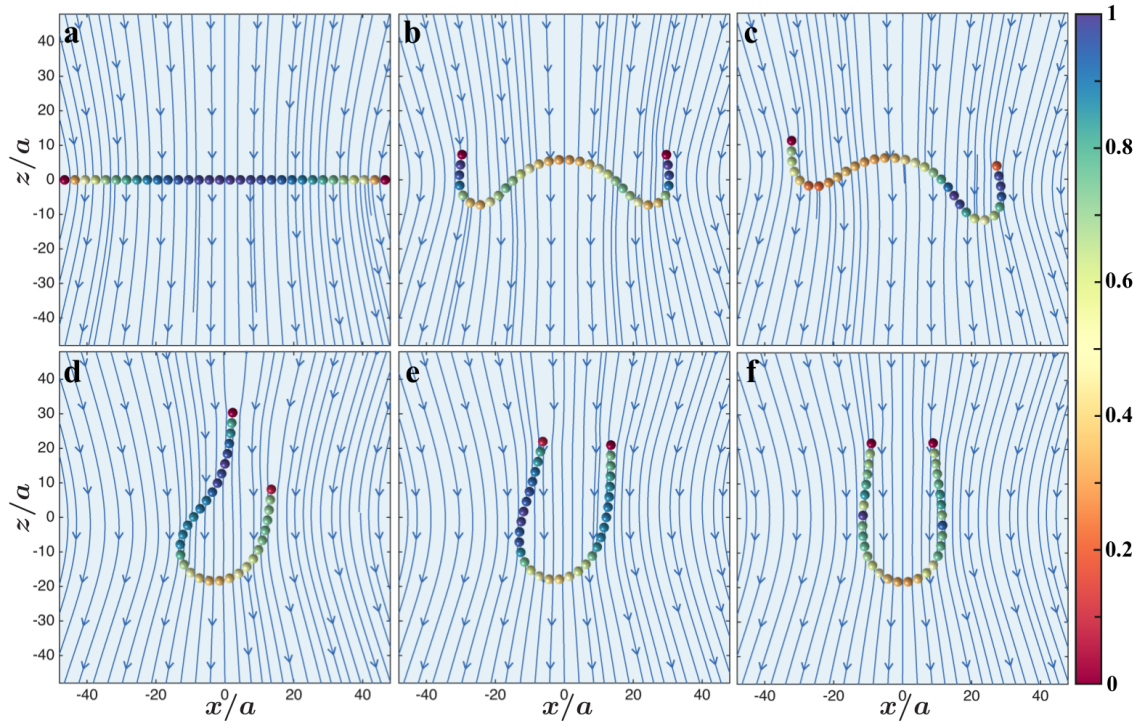


Figure 4.3: At moderately high sedimentation number \mathcal{S} , the planar filament initially reaches to a metastable state which by releasing elastic stress settle to a more stable state. To shed more light on this dynamical transition, we show the variation of hydrodynamic force on different parts of the filament, at different stages of transition.

We illustrate this in Fig (4.3), as the filament undergoes a series of transitions from the initial condition to a metastable state which finally relaxes to a stable state ([online-movie](#)). Initially, at the early stage of sedimentation, two domains of higher hydrodynamic force are generated about one-quarter away from the edges of the filament. As a result, a large amount of elastic energy gets accumulated in the middle of the filament and cannot be released by breaking the symmetry of the filament immediately. After a transient, the symmetry of the conformation breaks dynamically, one of the protrusions becomes dominant over the other, the centre of mass of the filament starts moving sideways and eventually the whole filament reaches a more stable state. The power dissipation in the metastable state is less than the stable state, which means the metastable conformation stores more energy than the stable steady conformation. Remarkably, we found that the

amount of time the filament spends before releasing the stored elastic energy depends on the difference of elastic energy stored in metastable and stable conformations (Fig. 4.4). The more the difference in energy, the lesser is the timespan.

When the difference of elastic energy is small, the transition occurs through a spontaneous release of stress stored in the metastable conformation. During such transition, two protrusions join up releasing the elastic energy dynamically and the conformation reaches a stable state without any sidewise displacements. At high sedimentation number, the filament settles to a steady state, where ends of the filament periodically oscillate. This oscillatory behaviour is reflected in the oscillations of the power dissipation in top-most curve of Fig. (4.4).

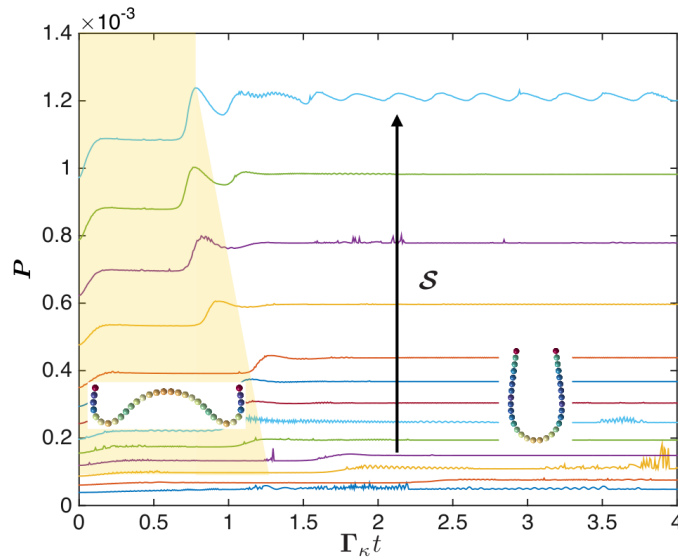


Figure 4.4: The transition from metastable W conformation to more stable horseshoe conformation can be understood from net power dissipation by the settling filament. In the plot, we show that, with the increase of sedimentation number \mathcal{S} , the difference between power dissipation increases, consequently, the lifespan of the metastable state decreases.

4.3.3 Aplanar steady states

There appear to be a multitude of aplanar steady states, several of which have been identified by Gompper and co-workers [154]. In the first of these states, (Fig (4.5a), the

filament forms a symmetric bow like structure, bent out of the plane, sliding sideways during sedimentation ([online-movie](#)). In the second steady state (Fig (4.5b), the filament forms a somewhat helical asymmetric conformation and sediments in a helical trajectory. In addition to these, we find a new steady state at high sedimentation number, when the filament spontaneously forms a twisted conformation as shown in the Fig (4.5c). While the whole filament spins about an axis parallel to the external field, the centre of mass follows a linear trajectory ([online-movie](#)). It is possible that there are further steady states in the dynamics which have not been reported yet. The principal purpose of our study of the passive problem is, first, to establish that our method can correctly reproduce previous results when activity is set to zero and, second, to provide a baseline from where we can attempt to understand the active problem as a perturbation from zero activity.

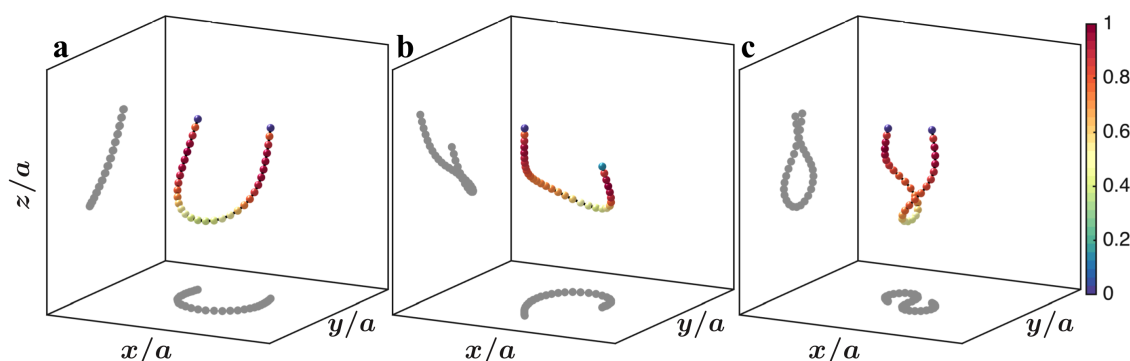


Figure 4.5: Aplanar steady states during sedimentation of passive filament are displaced. In all the figures the beads are coloured with normalised hydrodynamic force on them. In the steady state shown in (a), the filament slides sideways during sedimentation. In the steady state shown in (b), the filament sediments in helical trajectory. At high sedimentation number - \mathcal{S} - a non-linear state arises, shown in (c). During this state, the filament spins as its centre of mass settles in a linear trajectory.

4.4 Sedimentation of an active filament

We now study the sedimentation problem of an active filament, guided by the results of obtained above for zero activity.

4.4.1 Planar steady states

We find the sequence of steady states observed for zero activity as well as additional new steady states. We recall here, from Chapter 3, that spontaneous fluid flow because of contractile activity suppresses transverse perturbations whereas extensile activity enhances it. The manifestation of this in planar sedimentation at low activity, is in two ways: first by reducing (enhancing) the downward speed and by increasing (decreasing) domain of stability in the case of contractile (extensile) activity. The dynamics at a high *extensile* activity is even richer.

Beyond the critical value \mathcal{A}_S , where the filament become unstable due to spontaneous flow, the dynamics are due to a combination of both external field and internal activity. A series of new steady conformations can arise here due to dynamic balance of the active passive parts of the dissipative forces. One such mode is presented in the Fig (4.6b), where the filament forms an asymmetric bow and sediments in a linear trajectory ([online-movie](#)).

4.4.2 Aplanar steady states and transients

The aplanar dynamics of the active filament under sedimentation is rich. Our findings of different conformations and their trajectories are displayed in the Fig (4.6), their phase space and various other properties are shown in the Fig (4.7). We categorize this rich variety of states in the following manner.

Aplanar sliding state: This steady state is found predominantly when a planar conformation of a contractile filament goes unstable in the region demarcated by 2 in Fig (4.7a). During this state (Fig 4.6c), the filament forms a symmetric yet bent conformation which moves sideways as the filament sediments ([online-movie](#)). This phase is similar to what has been reported in passive filament sedimentation [154].

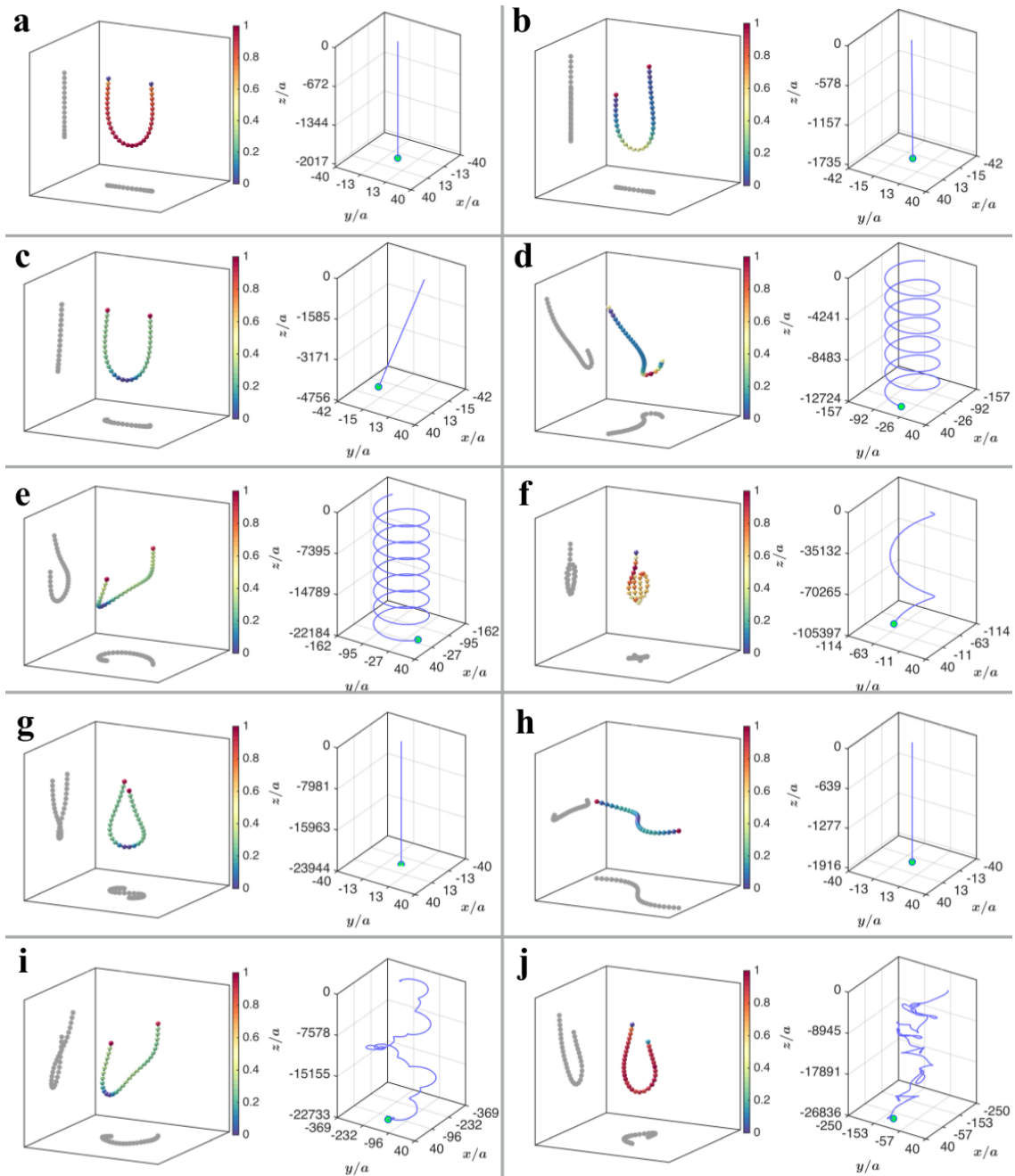


Figure 4.6: The inclusion of activity radically modifies the hydrodynamic force on different parts of the settling filament. Here we show various steady conformations, found in the sedimentation of active filament under a uniform external field. The steady conformations are presented in the left panel of the sub-figures, whereas the trajectories of the centre of mass of the filament are presented in the right panel of the sub-figures. We point here out that, in spite of trajectory and conformation of the filament is similar at different parameter domain, the distribution of hydrodynamic force along the filament can be quite different as presented in (d and e).

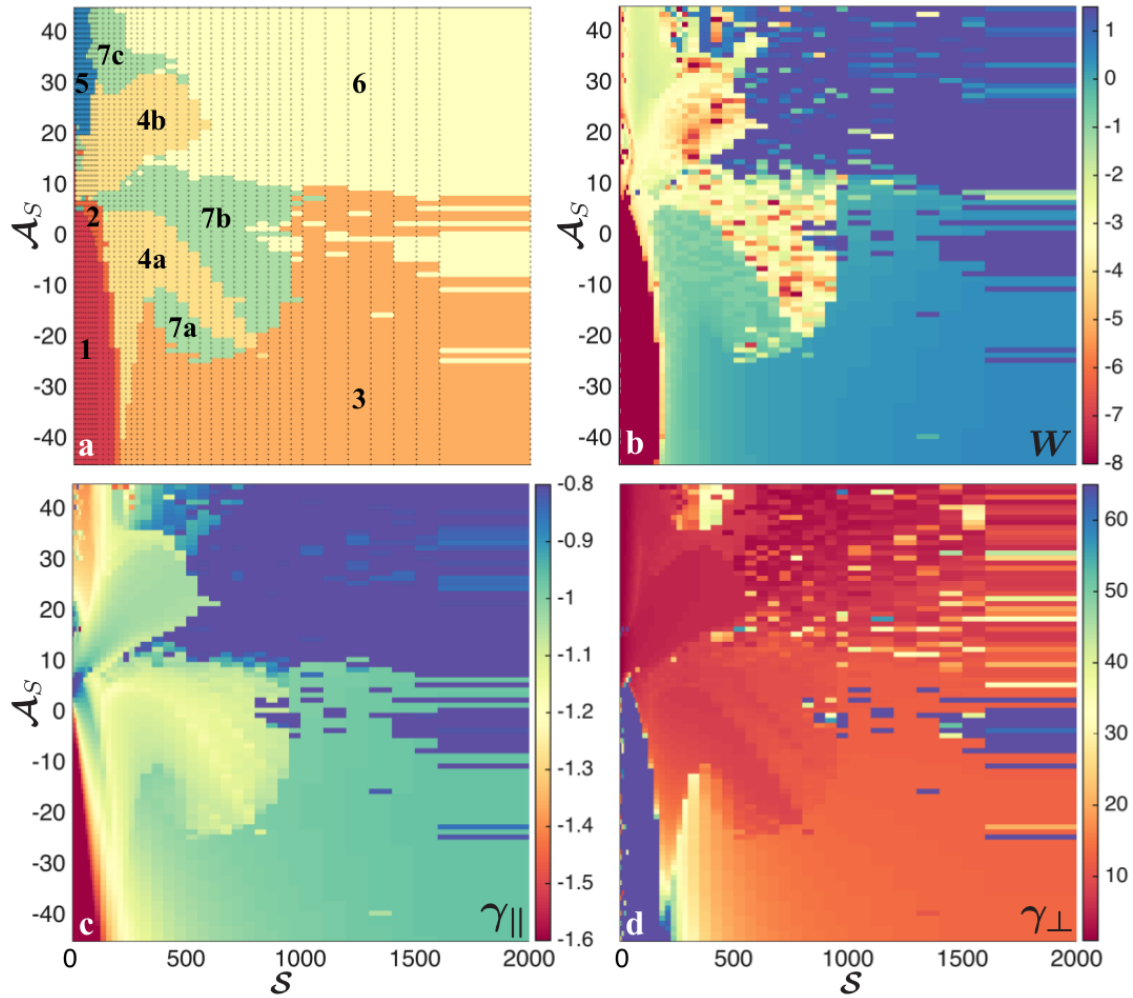


Figure 4.7: Here we separate out two-dimensional phase space, made of sedimentation number and activity number, in domains where different steady states are found, in (a), and their conformational property, mean writhe in (b) and dynamical properties, mean longitudinal and longitudinal resistances in (c) and (d). In the subfigure (a), 1 represents domain of planar sedimentation (Fig. 4.6 a), 2 represents domain of sliding sedimentation (Fig. 4.6 c), 3 represents domain of twisting sedimentation (Fig. 4.6 g), 4 represents domain of helical sedimentation (Fig. 4.6 d and e), 5 represents activity dominated rotation and sedimentation (Fig. 4.6 h), 6 represents higher modes forming different kind of loops (Fig. 4.6 f) and 7 represents long unsettled transient zones (Fig. 4.6 i and j).

Aplanar helical states: These states are found in different region of parameter space, demarcated as 4 in Fig (4.7a), suggesting an appearance of similar conformation due to different dynamic balance between competing mechanisms ([online-movie1](#) and [online-movie2](#)). In this state (Fig 4.6d and e), the filament forms an asymmetric helical structure

that settles following a helical trajectory. The speed of settling and the radius of the trajectory changes as any one of activity, external force and elasticity changes. Again, these are similar to conformations reported in the sedimentation of passive filaments [154].

Aplanar spinning states: These interesting states are found in predominantly in two domains, demarcated by 3 and 5 in Fig (4.7a). The region represented by 3, corresponds to the mode shown in (4.6 g) whereas, the region represented by 5, corresponds to the mode shown in (4.6 h). In the former region, the beads at the middle of the filament always stay lower than the beads of other parts and the whole filament spins continuously while the centre of mass of the filament follows a linear trajectory ([online-movie](#)). In the later case, though the trajectory is similar, the conformation of the filament is not. The minima of the conformation is not in the middle but close to the edges ([online-movie](#)).

Higher order states: At the region of high activity and high sedimentation number we observe a variety of complex higher order modes (6 in Fig 4.7a). Sometimes, they form loop-like structures (4.6 f [online-movie](#)), at other times they form conformations with a knot at the head and long tail, sometimes a knot in the middle of the filament with two asymmetrically extended ends and so on. One of these conformations has been reported earlier in the study of passive sedimentation in the presence of noise [151].

Transient states are also found in the phase space, where filament does not reach any of the steady states and sediments in an irregular trajectory. Examples of such conformations are shown in (4.6 i and j) and such regions are marked as 7 in Fig (4.7a).

4.4.3 Phase boundaries and dynamical features

The change of conformation of active slender bodies can be seen as a dynamic response to an external field. The best way to measure these non-linear responses by computing effective resistance coefficients in the parallel and perpendicular direction to the applied field. Similarly, conformational change can be observed by measuring writhe. These

quantities, mean writhe and effective friction coefficients are presented in the Fig (4.7).

Writhe is a measure of helicity of a three dimensional curve, defined as

$$W = \frac{1}{4\pi} \int_C \int_C d\mathbf{r}_1 \times d\mathbf{r}_2 \cdot \frac{\mathbf{r}_1 - \mathbf{r}_2}{|\mathbf{r}_1 - \mathbf{r}_2|^3}. \quad (4.5)$$

where \mathbf{r}_1 and \mathbf{r}_2 are points on the curve. We numerically compute discrete form of this quantity to characterise the filament conformation. The details are given in the Appendix.

Usually, writhe of the conformation is zero when the filament sediments in a plane and non-zero otherwise. For some of the transient states, mean writhe is found to diminish.

The response coefficients, effective friction tensors for the filament in their steady states are presented in Fig (4.7c) and Fig (4.7d). The parallel and perpendicular component are defined as,

$$\gamma_{\parallel} = \frac{|\mathbf{v}_{\parallel}|}{|\mathbf{F}^e|}; \quad \gamma_{\perp} = \frac{|\mathbf{v}_{\perp}|}{|\mathbf{F}^e|}, \quad (4.6)$$

where, \mathbf{v}_{\parallel} and \mathbf{v}_{\perp} are the steady state velocity of the filament in the direction parallel and perpendicular to the applied field \mathbf{F}^e . These quantities, γ_{\perp} and γ_{\parallel} are function of sedimentation number \mathcal{S} and activity number \mathcal{A}_S . We note that the parallel component is maximum for planar cases, and less for others. Similarly, perpendicular component is least for the planar cases, but more for other aplanar conformations.

4.5 Conclusion

Here, in this chapter we demonstrated the dynamic responses of active and passive filaments to external fields in detail. First at zero limit of activity of our model, we reproduced dynamical steady states in passive sedimentation found in earlier studies. We have discussed the effect of activity on planar as well as aplanar conformations. We concluded the chapter by computing various response coefficients to indicate non-linear responses

found in the presence of activity and non-local fluid interaction.

In the passive limit of our theory, we found new states and explained the dynamical transition from energetics and correlated it to the stability of the metastable state. In the presence of activity, we showed the appearance of a series of steady states which arise due to the dynamic balance of various forces out of equilibrium. We characterised those states and their regions of stability.

Our general modelling of active slender bodies makes it an ideal candidate to explain dynamical and conformational dynamics of contractile and extensile bio-filaments in external magnetic or centrifugal field [154, 155]. Moreover, one would expect similar settling dynamics in the system of a chain of tri-metallic nanorods under external field [140, 141].

Our theory, developed in this chapter can be thought as a generalisation of the bead-spring theory of passive filament including internal activity. In those earlier studies [149, 150, 151, 154], the beads are passive and coupled hydrodynamically through the Oseen-Burgers tensor. In a parallel development, slender body theory has been used to study the problem in detail [148, 152, 153]. Our work in this chapter can be thought of as an extension of these past studies to an active filament. It is well-known that response of polymeric matter to external perturbations is complex. An interesting direction for future research is to understand how active polymeric matter responds to external perturbations. The response of a single active filament studied in this chapter is a first step in that direction.

Biomimetics: passive filament driven by an active colloid

Active colloids and externally actuated semi-flexible filaments provide basic building blocks for designing autonomously motile micro-machines. In this chapter, we show that a passive semi-flexible filament can be actuated and transported by attaching an active colloid to its terminus. We study the dynamics of this assembly when it is free, tethered, or clamped using overdamped equations of motion that explicitly account for active fluid flow and the forces it mediates. Linear states are destabilized by buckling instabilities to produce stable states of non-zero curvature and writhe. We demarcate boundaries of these states in the two-dimensional parameter space representing dimensionless measures of polar and apolar activity. Our proposed assembly can be used as a novel component in the design of micro-machines at low Reynolds number.

5.1 Introduction

Autonomously motile micromotors are the basic building blocks for ballistic transport in cellular and extra-cellular level. Classic examples from biology include cilia and flagella [14]. The central role of those organelles is to accomplish individual motility, to help in transporting genetic material, removing unwanted materials, inducing spontaneous flow to push mucous, biological fluids in a particular direction and enhance transport. Development of synthetic and controllable micromachines may replace those biological micromachines to accomplish these jobs [156, 79]. Moreover, they can be used to trans-

port genetic material, therapeutic payloads and functionalised groups to a target and to enhance fluid mixing in microfluidic chambers by inducing flow.

But developing micromachines synthetically are quite challenging, hindered by the physical laws [95]. The major challenges are Brownian noise, viscosity dominated motion and many-body interactions. Combining chemistry, physics and technology, researchers around the world have come up with different interesting ideas. Those ideas are still evolving, which can be categorized mostly in three basic mechanisms, first, external driving control, second by internal activity, using phoretic mechanism and third bio-hybrid ones, combining biology and technology. External field used so far to move slender structures are electric [30, 157, 158], magnetic [159, 29, 129, 160] and recently by ultrasound [31, 161]. Internal mechanism covers various phoretic motions by patterning the surface of the solid body with different metals or by specific chemical compounds [143, 144, 146, 32, 162, 133]. Doing so, these bodies can move in a particular fluid medium such as H_2O_2 , hydrazine and other chemicals. These micromotors are quite fast but mostly work in corrosive environment. Recent developments of enzyme based micro-motors show more applicability inside an organism [81, 33]. The third category of micromachines is engineered in such a way that it can move using internal and sometimes by external driving [130, 35, 131, 132, 85]. Examples of this category include selective attachment of heart cell on a slender body and combining metallic structures with spermatozoa and flagella. Marangoni flow and bubble driven mechanisms are few of the other noteworthy suggestions [163, 162, 80]. While the motion of a slender body due to external driving has been explored theoretically in detail, there is no contribution for autonomous motion in the absence of external forces and torques, which include the second and third category of experiments we have mentioned.

Here, we demonstrate that spontaneous actuation can be achieved, by combining elastic filaments and active beads. We propose a novel way to develop synthetic micro-

actuator which can be used to increase mixing in microfluidic chambers, transport colloidal loads, to form an array of synthetic cilia.

In this chapter, we first develop our model in detail. Then, defining two dimensionless activity numbers, one for apolar activity another for polar activity with respect to the elasticity of the body, we study the dynamics of the assembly. We found that under compressive stress generated by the activity, the linear conformation buckles and as a consequence nonlinear steady states arise. Those aplanar and planar states and their properties are further characterised and their domain of appearance is demarcated in the two-dimensional phase space of two activity number. Further performing linear stability analysis on the linear conformation, we find out the nature of the transition from linear quiescent state to dynamic modes.

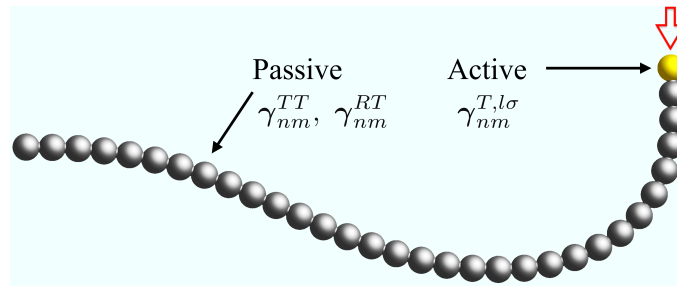


Figure 5.1: Schematic diagram of a passive filament driven by an active colloid suitably attached to its terminus.

5.2 Model description

Our micro-machine is modelled as an assembly of a passive filament and an active colloid attached suitably to its terminus. Schematic diagram of the assembly is presented in the Fig. (5.1). This particular design is motivated by the fact that smaller micro-motors are more efficient but vulnerable to thermal noise. Therefore, to make efficient yet controllable micro-machine, we propose to use the efficiency of the small active colloid along with passive segment as a bias. This model can also be seen as a subset of co-block

polymers that are made of passive and active segments.

As always, throughout this thesis, we discretise the filament by a set of total N beads connected consecutively to form a chain, which is described earlier in Sec. 2.2. These N beads are consists of N_1 active and N_2 passive beads distributed accordingly. In this particular problem, first $N - 1$ beads are passive and the last bead is active. The boundary conditions on the beads are then,

$$\mathbf{v}(\mathbf{R}_n + \boldsymbol{\rho}_n) = \begin{cases} \mathbf{V}_n + \boldsymbol{\Omega}_n \times \boldsymbol{\rho}_n, & n \in \text{passive} \\ \mathbf{V}_n + \boldsymbol{\Omega}_n \times \boldsymbol{\rho}_n + \mathbf{v}^A(\boldsymbol{\rho}_n), & n \in \text{active}. \end{cases}$$

The activity if the beads reveal through self-propulsion, \mathbf{V}_N^A , as well as in the generation of apolar active flows. Accordingly, we consider both $\mathbf{V}_N^{(2s)}$ and $\mathbf{V}_N^{(3t)}$.

$$\mathbf{v}^A(\boldsymbol{\rho}_n) = - \underbrace{\mathbf{V}_n^A + \frac{1}{15} \mathbf{V}_n^{(3t)} \cdot (\boldsymbol{\rho}_n \boldsymbol{\rho}_n - \frac{1}{3} \boldsymbol{\delta})}_{\text{polar}} + \underbrace{\mathbf{V}_n^{(2s)} \cdot \boldsymbol{\rho}_n}_{\text{apolar}}, \quad n \in N. \quad (5.1)$$

This model is sufficiently general to describe the far-field flow of a variety of polar and apolar active colloids. We assume that the principal axes of the slip coefficients are parallel to the tangent vector, \mathbf{t}_N , at the terminus of the filament, so that

$$\mathbf{V}_N^{(2s)} = as_0(\mathbf{t}_N \mathbf{t}_N - \frac{1}{3} \boldsymbol{\delta}), \quad (5.2)$$

$$\mathbf{V}_N^A = -\frac{3}{5} \mathbf{V}_N^{(3t)} = -\frac{3a^2}{5} d_0 \mathbf{t}_N. \quad (5.3)$$

Here we note that, in this parametrisation self-propulsion velocity \mathbf{V}_N^A and $\mathbf{V}_N^{(3t)}$ are related.

Equation of motion : Appealing to these considerations, we write down the effective

equation of motion for N -th active bead and constituent passive beads

$$\begin{aligned} \dot{\mathbf{R}}_n = & \frac{1}{6\pi\eta a} \mathbf{F}_n^{int} + \sum_{m \neq n} \mathcal{F}^0 \mathcal{F}^0 \mathbf{G} \cdot \mathbf{F}_m^{int} + \frac{28\pi\eta a^3}{3} \mathcal{F}^0 \mathcal{F}^1 \nabla_N \mathbf{G} \cdot \mathbf{s}_N \\ & + \frac{4\pi\eta a^5}{5} \nabla_N^2 \mathbf{G} \cdot \mathbf{d}_N, \quad n, m \in \text{filament} \end{aligned} \quad (5.4)$$

$$\dot{\mathbf{R}}_N = \frac{1}{6\pi\eta a} \mathbf{F}_N^{int} + \sum_{m \neq N} \mathcal{F}^0 \mathcal{F}^0 \mathbf{G} \cdot \mathbf{F}_m^{int} - \frac{3a^2}{5} \mathbf{d}_N. \quad \text{active colloid} \quad (5.5)$$

Dimensionless numbers : In the system of a passive slender body driven by an active colloid, we identify basic length scales. They are the length of the slender body, L and a is the radius of the cross section. From discretisation of the slender object to series of connected beads, we get another length scale that is the equilibrium separation between two consecutive beads, b . Similarly, we identify timescales of the system. For a passive filament of length L , and of bending rigidity κ , the rate at which any transverse perturbation relaxes is $\Gamma_\kappa = \kappa/\eta L^{d+1}$ in space dimension $d = 3$. Two modes of non-equilibrium surface activity generate compressive stress by hydrodynamic interaction at the terminus of the passive filament and comparing these with respect to the bending elasticity of the slender structure leads to two dimensionless numbers $\mathcal{A}^{(2s)}$ and $\mathcal{A}^{(3t)}$. We study the dynamics of slender body in the phase-space defined by these two dimensionless groups

$$\mathcal{A}^{2s} = \frac{7\pi\eta a^4 L^2 s_0}{\kappa b^2}, \quad (5.6)$$

$$\mathcal{A}^{3t} = \frac{18\pi\eta a^3 L^2 d_0}{5\kappa}. \quad (5.7)$$

5.3 Dynamics of the assembly

The dynamics of a passive filament driven by an active colloid is presented in this section. To get a clear understanding, we first investigate the dynamics of an active colloid of both motile and non-motile nature when weighted by a passive colloid. The spontaneous fluid-

flow generated through the interaction is presented in the Fig. (5.2). In the panel (a), the direction of movement of the assembly and fluid flow in its periphery is presented when the active bead is motile. Identical quantities are presented in (b and c), when the colloids are symmetric dipoles of extensile and contractile in nature. The white arrow indicates the direction of the movement of the assembly. The speed and the direction of the motile assembly depend on the position of the passive bead with respect to active bead, the orientation of the active bead and the separation between two beads.

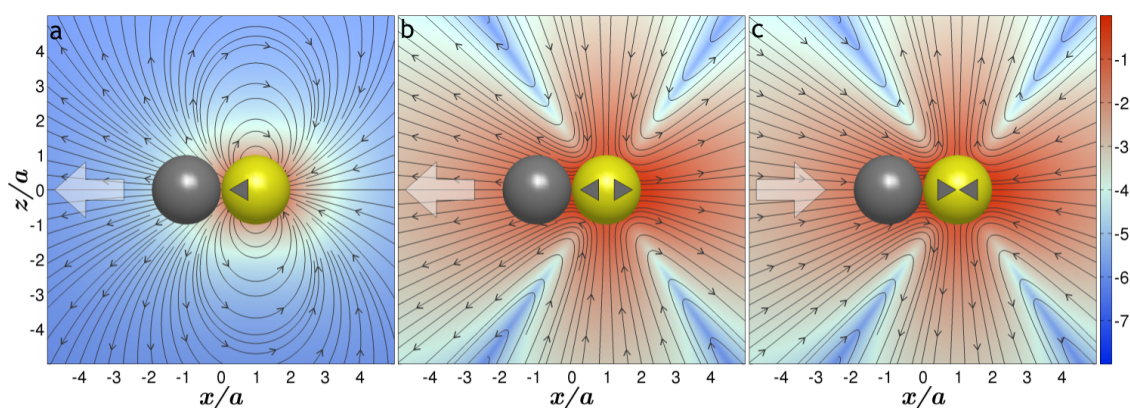


Figure 5.2: Fluid flows around an assembly of passive-active colloids with the background, pseudo-colored with the natural logarithm of the magnitude of the fluid velocity. In (a) the active colloid is motile (degenerate quadrupole) but in later panels (b and c) active colloids are non-motile (symmetric dipole) and respectively contractile and extensile in nature. Big white arrows in all the panels show the direction to which the assembly would move. Interestingly, an assembly of non-motile active colloid and a passive colloid can become motile by breaking the symmetry of the flow. The direction and velocity of the assembly critically depend on the parameters of the configuration, such as the orientation of the active bead, its nature and separation with the passive bead.

To find out the detailed dynamics of the assembly of passive filament driven by active colloid, we numerically integrate equations of motion of this system using a variable coefficient method. The parameters and method used are given in the appendix.

Results from our numerical investigation are presented in the Fig. (5.3) for all three cases. The steady states and fluid flow arising through the interplay between structure and the fluid are presented categorically.

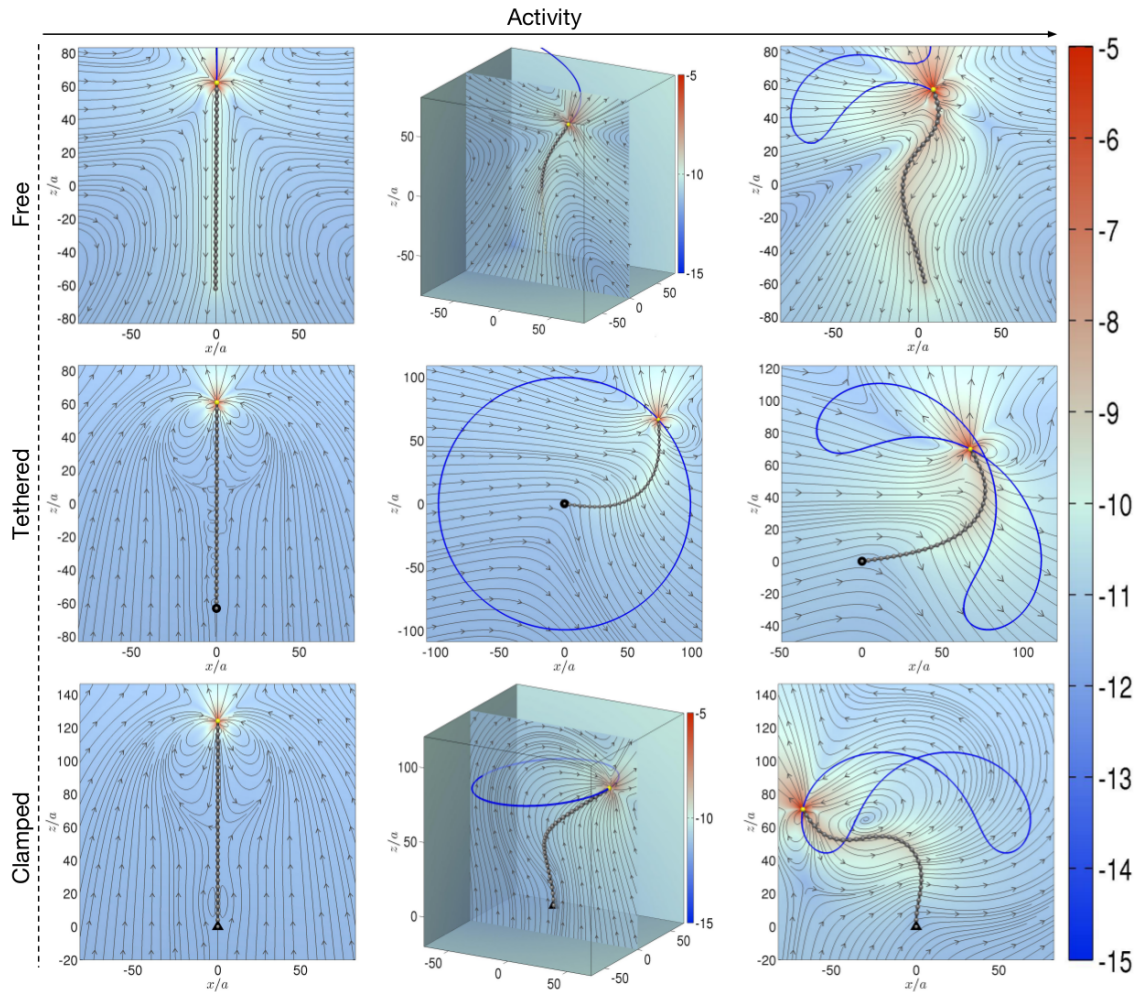


Figure 5.3: Non-equilibrium steady states of a free (a)-(c), of a tethered (d)-(f) and clamped (g)-(i) slender body with a active colloid attached to its terminus. The figures show various dynamic and static conformation of the slender body with the increase of activity. The fluid flows at a plane are shown by streamline with the background is pseudo-coloured with the logarithm of the magnitude of the fluid flow.

Free Boundary Condition: The steady states of the assembly, when free of any constraints, is shown in the first row of the Fig (5.3). When the active colloid produces a flow that pulls the passive structure, the linear conformation is stable to any transverse perturbations. But, when the spontaneous flow pushes the whole structure, after a critical threshold of combined activity, the linear conformation become unstable due to any transverse perturbation. This transition happens through a Hopf bifurcation. Just after the instability, the filament reaches a steady state. In this steady state ([online-movie](#)),

the whole assembly forms a three-dimensional helical structure and propel in a helical trajectory with time (Fig 5.3 middle panel of the first row). The shape of the body in this state, usually, varies a little during spontaneous motion. With further increase of activity, strength of the spontaneous fluid flow increase and after a critical value of net activity, the helical conformation becomes unstable and ends up in an oscillatory state. In this state, the conformation of the assembly become planar and oscillatory in nature. Autonomous propulsion happens in this state by complex oscillatory mode (shown in Fig 5.3 last panel of the first row). During this state, the assembly has distinctively two different parts, almost not changing initial part and dynamic active end. The [online-movie](#) explains the dynamics clearly.

Tethered Boundary Condition: The dynamics of the assembly is studied when the passive end is tethered to a point in an otherwise infinite medium. The outcome of the study is presented in the second row of the Fig. (5.3). When spontaneous flow pulls the assembly away from the tethered point, the bond between the passive beads gets stretched to counterbalance the pull. But when the spontaneous flow pushes the assembly towards the tethered point, after a certain threshold, the linear assembly undergoes a transition and a new dynamic state arises. In this state, the whole assembly bends slightly and start rotating in a plane around the tethered point. This transition happens through simple instability, unlike the constraint-less case. In this state, the rate of activity which promotes bending matches with the restoring elasticity. When the strength of the activity increases, this dynamic balance dissolves away and oscillatory mode arises. For even higher activity regime, this state becomes unstable and end up in other higher order complex modes.

Clamped Boundary Condition: The dynamics of the assembly, clamped at the passive end is studied here. The dynamical steady states and spontaneous fluid flow around it is displayed in the third row of Fig. (5.3). The linear assembly due to spontaneous flow that pulls the assembly away from the clamped point is quite similar to the tethered case.

This conformation also goes through the transition under compressive flow. But because of clamping condition, the rotational mode is infeasible. The only possibility remains, is to go to a three-dimensional helical state. In this state, the assembly with slight helical conformation does not change its shape with time and undergoes revolution. The conformation is shown in the middle panel of the third row of the Fig. (5.3). This transition occurs through a Hopf bifurcation. The dynamic balance between elasticity and activity breaks down with further increase of activity and planar beating mode arises. With further increase of the activity this mode becomes unstable and higher order complex modes appear.

Writhe and Curvature : Using properties of the assembly such as mean curvature, standard deviation, writhe can be used to distinguish various steady states. While curvature of a structure identifies bending, writhe identifies out of plane distortions. Basically writhe is a measure of helicity presented in an earlier section 5.4. During the linear steady states, both the quantities, mean curvature and writhe are zero but pick up nonzero contribution when aplanar. In the planar beating state, writhe and time averaged curvature is zero, but standard deviation of the curvature is nonzero. For the case of planar rotation, found when the filament is tethered, the mean curvature of the assembly is also nonzero, but writhe is zero. Thus, using these two quantities of the conformation of the assembly, the phase space can easily be demarcated into zones of different steady states.

In the Fig. (5.4), we display the dynamics of the writhe to demonstrate the way initial linear conformation relaxes to different steady states when the filament is free and clamped varying one of the parameters keeping the other fixed. In the low activity, the writhe of the filament always stays at zero after initial transients, indicating stability of linear conformation. In the intermediate values of activity, after the initial transient writhe saturates at a finite value, indicating aplanar mode. With further increase of activity, the writhe of the conformation again goes to zero, indicating the appearance of planar steady

state. Similar phenomena are found again for clamped filament. For the tethered filament, all the steady states are planar and curvature is enough to identify the states.

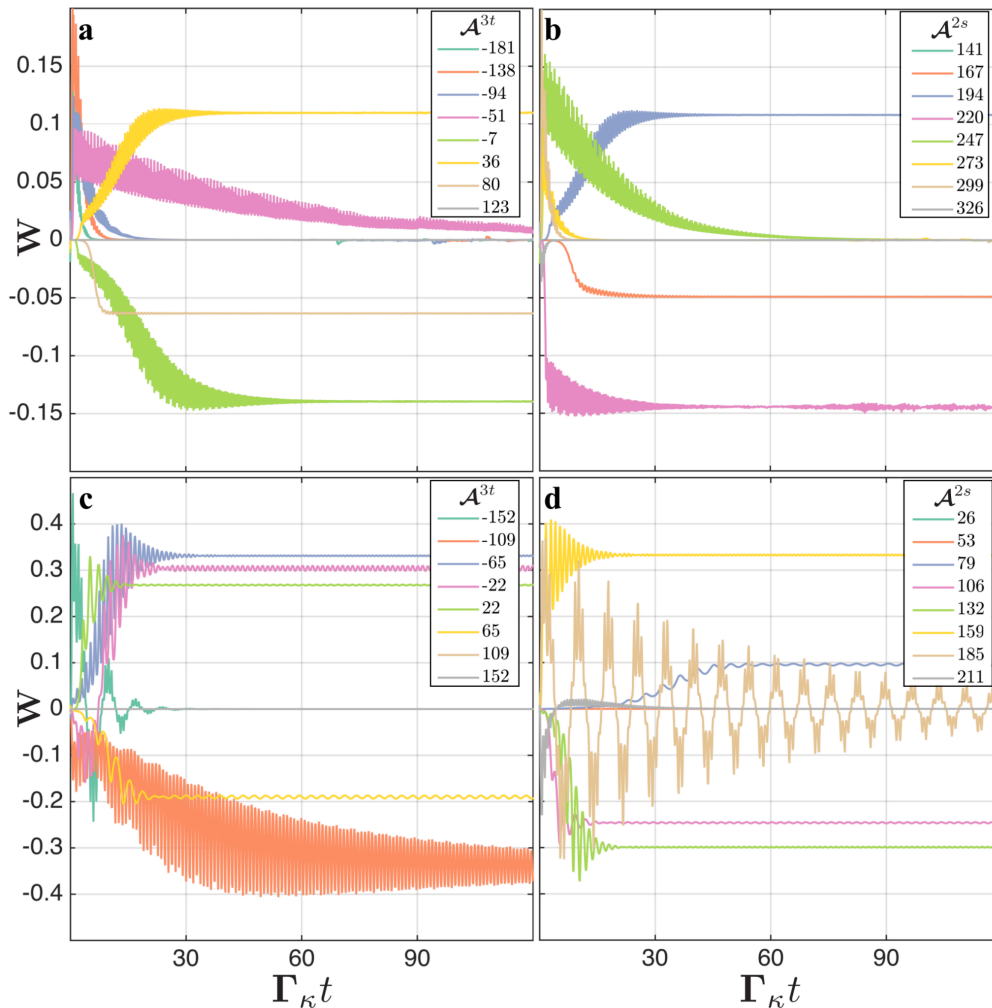


Figure 5.4: Writhe of the assembly is plotted when the assembly is free (a-b) and clamped (c-d). In subfigure (a) and (b), the variation of writhe shown with the increase of one dimensionless number, while the other number is kept constant. It shows that at a lower value of activity(s) writhe is zero as the conformation is linear, at the intermediate value it become nonzero as the conformation is helical and at the higher value it again goes back to zero due to planar mode, indicating a transition from helical conformation to planar conformation. Similar plot for clamped assembly is presented in the subfigure (c and d).

Phase boundary : In the two-dimensional phase spaces defined by apolar $\mathcal{A}^{(2s)}$ and polar activity $\mathcal{A}^{(3t)}$, regions of different steady states are demarcated in the Fig. (5.5) for all the three cases, free, tethered and clamped. The simulation points are shown with

symbols.

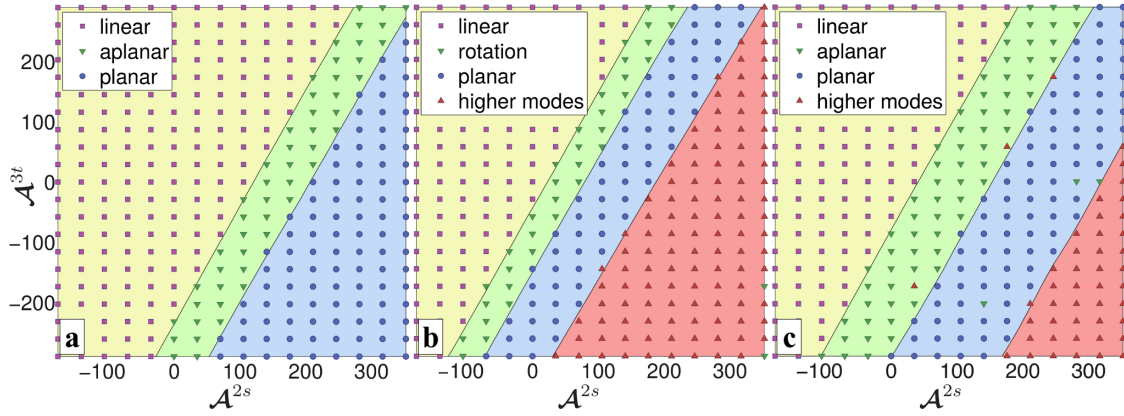


Figure 5.5: Phase diagram (colour online) of dynamic steady states for free-free boundary condition in (a), for tethered-free boundary condition in (b) and for clamped-free boundary condition in (c) in dimensionless parameters \mathcal{A}^{2s} and \mathcal{A}^{3t} .

5.4 Linear stability analysis

To elucidate the nature of transition, a linear stability analysis (LSA) is performed numerically on the steady linear conformation of the assembly. The procedure of performing LSA is presented earlier in the Sec. 3.6. The result of our analysis for this system is presented in the Fig. (5.6) keeping polar activity to zero. The transition from linear conformation to oscillatory helical conformations, in the cases of free and clamped, happen through a Hopf bifurcation. During this kind of transition, two eigenvalue become unstable simultaneously. On the contrary, the transition from linear quiescent conformation to revolution with a slight bent, in the case of tethered boundary condition, occurs through a simple instability. Only one eigenvalue become positive during this transition.

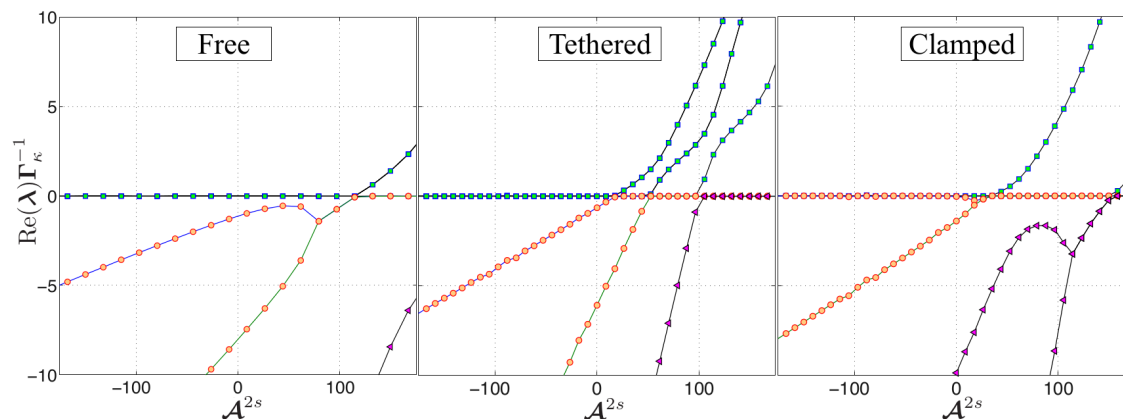


Figure 5.6: Linear stability analysis of the linear conformation is presented with the increase of dimensionless parameter \mathcal{A}^{2s} for free (a), tethered (b) and clamped (c) assembly. We show that, the transitions through which stable linear conformation goes to oscillatory states (a and c), instabilities occur through Hopf bifurcations, on the contrary when the transition leads linear conformation to global rotation (b), the instability happens through zero-crossing of the largest eigenvalue.

5.5 Conclusion

In this chapter, we show that autonomous actuation can be achieved by attaching an active colloid to the terminus of a elastic passive filament. Furthermore, our detail numerical study shows, the interplay between elasticity of the passive segment of the filament and activity that promotes buckling instability in a viscous environment generate actuation. This spontaneous actuation in the absence of any external forcing can be used as an engine of a micromachine, micro-actuator and for efficient mixing.

The ideal candidate to check our theory can be developed by attaching a catalytic nanomotors to an elastic slender structure and keeping the whole assembly in H_2O_2 solution. Moreover, attaching a large number of these components to a surface, synthetic yet autonomously actuating ciliary layer can be developed.

Previous studies on biomimetic motion usually modelled by external driving of an elastic body and corresponding actuation dynamics are studied in details with and without hydrodynamic interaction [164, 92, 89, 154]. Therefore, force-free torque-free nature of

active suspension and activity induced hydrodynamic interactions are not considered.

Emergence: collective dynamics of many active rods

Here, we present the emergent behaviour of active rods in a viscous fluid in an unbounded domain and near a wall. Active rods in the micro-hydrodynamic regime can produce spontaneous flow and interact with others hydrodynamically. As its consequence, in unbounded geometry, a pair of extensile rods attract each other in parallel and repel in perpendicular conformation and show the opposite dynamics for the contractile case. These fluid mediated interactions lead to form assemblies, which are in general autonomously motile and dynamic in nature. The presence of no-slip wall modifies the properties of the spontaneous flow, resultant hydrodynamic interaction and dynamical behaviours. Though the dynamics parallel to the wall remains qualitatively the same, the dynamics perpendicular to it differs significantly due to the breaking of translational symmetry in the concerned direction. To elucidate the problem in detail, we successively investigate the dynamics of a single rod, a pair and many of them in detail near a wall. Furthermore, the collective dynamics in unbounded and wall-bounded domains are compared with each other. Our theory and understanding provide the first crucial step to developing a general theory of momentum conserving active suspension near a wall. We conclude the chapter by comparing our findings with recent experiments on tri-metallic active rods near a wall and possible future direction.

6.1 Introduction

Assembling identical components to a complex yet robust structure is very common in different contexts in biology, chemistry and physical sciences. Elucidating the mechanism behind these processes, not only quench the thirst for theoretical knowledge but also help in developing methods to synthesise materials with desired property. Such novel materials have revolutionised the whole technology many times over the last century. In recent times, there is a fresh interest to develop smart material, that can modify their behaviours and conformations dynamically in response to external perturbations [165, 166, 167, 168, 169]. Though the mechanisms behind these dynamic processes, near thermal equilibrium, are well-understood by either energy minimisation or entropy maximisation [170, 171], mechanisms beyond the realm of equilibrium are hardly understood. Therefore, an enormous potential lies in developing novel techniques.

Moreover, those active systems, unlike their passive counterparts, show rich collective dynamics and emergent phenomena. For example, In recent experiments on chemically active colloids, microbes and active motor microtubule assemblies display enhanced diffusion, autonomous motion, phase separation, pattern formation and spontaneous generation and dissociation of defects [37, 36, 172, 23, 45, 42, 49, 34, 47, 48, 46, 173, 43, 44]. In spite of much work over last few year [11], such phenomena are yet to be fully understood. Consequently, full control over these systems is still beyond reach .

So far, the theory developed for these systems are either from continuum analysis or from kinetic theories [11, 174, 175, 173, 176]. While in continuum approach, the symmetries of the problem are used to identify hydrodynamic variables and corresponding constitutive equations, kinetic theories provide a systematic method to get the probability functions satisfying specific collision rules. These relevant quantities are then studied in long wavelength approximations to predict the dynamics of the system. Thus, in those methods, small wavelength phenomena, the effect of boundaries and microscopic details

are not included.

In a typical experimental system, these small microscopic details and presence of macroscopic boundaries are crucial. For example, non-motile active nano-rods in H_2O_2 solution show rich dynamic behaviours near a wall [141, 140]. They generate specific conformations in a pair and spontaneous motions. The mechanism behind the motions is not yet completely understood. Therefore, to elucidate the mechanism behind the phenomena and to fill up the gap between experiments and theory in this chapter, we investigate the dynamics of slender active rods in unbounded and wall-bounded geometry. The conservation of momentum and consequently, the hydrodynamic interaction between different rods are explicitly considered.

6.2 Model description

Active rods are modelled by a series of beads connected each other by stiff non-linear elastic potential. The strength of the elasticity is an order of magnitude higher than the other relevant scales. These beads are active and produce dipolar flow along their principal axes. In unbounded domain description of an active body is already presented in the Sec. 2.6. Near a no-slip wall, the hydrodynamic interaction between the beads and corresponding hydrodynamic forces and torques are computed by using Lorentz-Blake tensor [115, 116], presented earlier in Eq. (2.42),

$$G_{ij}^w = G_{ij} - G_{ij}^* - 2h\mathbf{M}\nabla_j G_{i3}^* + 2h^2\mathbf{M}\nabla^2 G_{ij}^*. \quad (6.1)$$

Equation of motion: Thus modifying Green function that encodes correct hydrodynamic interaction, we get

$$\dot{\mathbf{R}}_n = \boldsymbol{\mu}^w \cdot \mathbf{F}_n^{int} + \sum_{m \neq n} \mathcal{F}^0 \mathcal{F}^0 \mathbf{G}^w \cdot \mathbf{F}_m^{int} + \frac{28\pi\eta a^3}{3} \sum_{m \neq n} \underbrace{\mathcal{F}^0 \mathcal{F}^1 \nabla \mathbf{G}^w \cdot \mathbf{s}_m}_{Active}. \quad (6.2)$$

In spite of the similarity with the Eq. 3.5, many crucial differences are hidden behind those innocuous equations. The first point to note is that, due to the self-interaction with the image, one body mobility matrix gets modified and no longer isotropic in all direction. The second point is that an isolated active rod, which is quiescent in an infinite domain, can have motion produced by complex interaction with its own image.

In the following sections, we first describe the dynamics of the pair of active rods in an unbounded domain and followed by, the dynamics of them near a wall. We have considered both the cases when the rods are neutrally buoyant as well as when the rods are bottom heavy. We conclude the chapter with comparison with dynamics of many active rods in the infinite domain and near a macroscopic wall.

6.3 Dynamics of two active rods in unbounded flow

Resolving the dynamics of a pair of rods is the cornerstone to elucidate the dynamics of many active rods. Therefore, we choose various experimentally observed conformations and study the dynamics of them only due to hydrodynamic interaction. The conformation found in experiments are generally of two kinds, perpendicular and parallel. An extensile active rod generates a spontaneous flow, that pulls the fluid from all the direction perpendicular to its major axis and expels out the fluid along its axis. In the case of a contractile active rod, the spontaneous flow pulls the fluid along the axis and expelled out to all the direction perpendicular to the principal axis of the rod. Here, we note down that, an isolated rod can not move by itself in an infinite domain by breaking the flow symmetry.

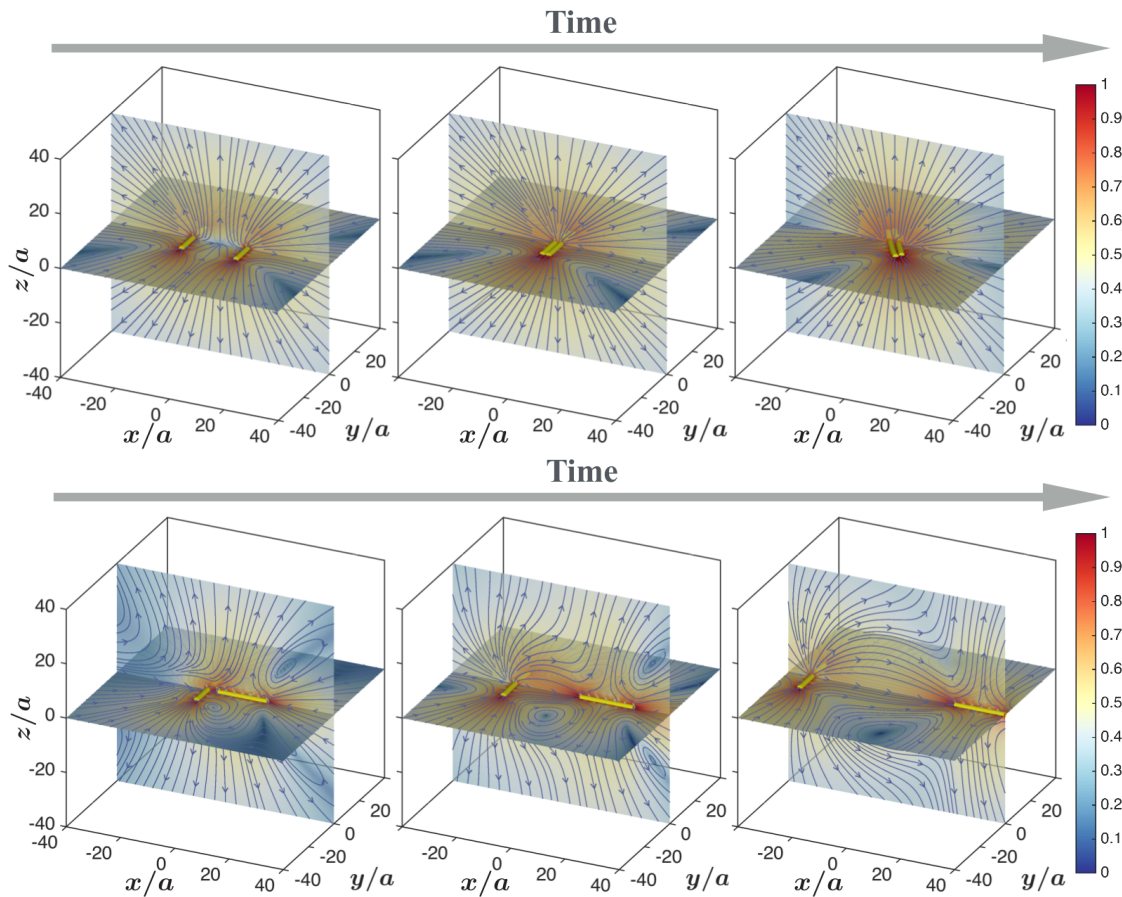


Figure 6.1: Dynamics of a pair of stiff extensile rods in an infinite medium. Hydrodynamic interaction generates net attraction when the rods are in parallel configuration whereas, generates repulsion when they are in the perpendicular configuration.

Let's assume, a pair of extensile rods is suspended in an infinite domain, in parallel to each other. Due to the geometry, the spontaneous fluid flow generated by one pull the other and vice-versa. Therefore, there is a net attraction between the parallel extensile rods due to HI. The dynamics is shown in the first row of the Fig. 6.1 and by a [online-movie](#). On the other hand, if the extensile rods are in perpendicular conformation (say in T shape), the flow produced by the first rod (upper one) pulls the second one, but the flow generated by the second rod pushes the first filament away. The fluid flow due to the latter is stronger than the former because the spontaneous flow is expelled out only in one direction pulling the fluid from other two perpendicular directions. As a

result, perpendicular conformation or T configuration is unstable and unlikely to form spontaneously for extensile rods (shown in the second row of the Fig. 6.1 and in [online-movie](#)).

We found that once two parallel extensile rods form a pair, a misalignment happens dynamically and the assembly starts rotating ([online-movie](#)). The sense of the rotation of the cluster is found to be clockwise if the end of the rod situated at the right side of the assembly extended downwards.

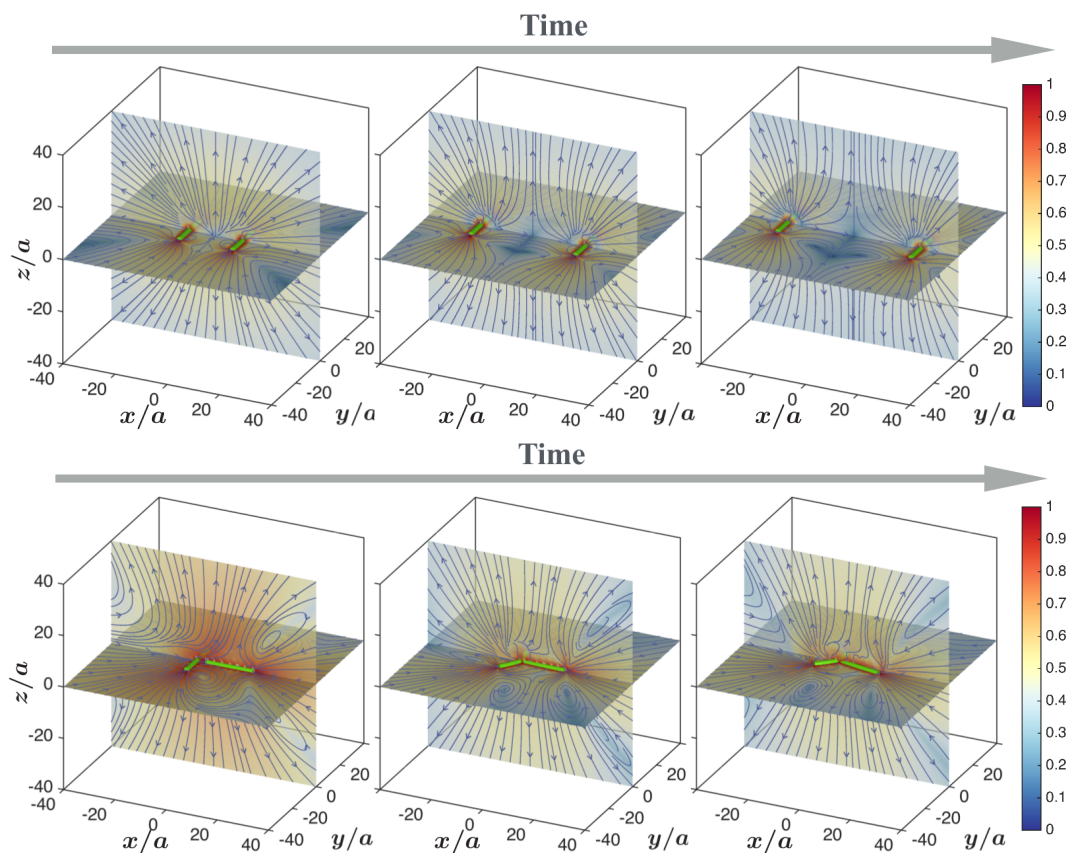


Figure 6.2: Dynamics of a pair of stiff active contractile rods in an infinite medium. In contrary to the extensile case, here, hydrodynamic interaction generates net repulsion when the rods are in parallel configuration whereas, generates attraction when they are in the perpendicular configuration.

For the case of contractile rods, the spontaneous fluid flow it generates is exactly opposite to its extensile counterpart. Therefore, there is net hydrodynamic repulsion if the

rods are in parallel and a net hydrodynamic attraction when the rods are in perpendicular or in T conformation. The dynamics of the pairs are presented in the Fig. 6.2. The contractile rods can spontaneously form a stable T junction and the whole assembly moves in the direction towards the leg of the T. For high activity, the contractile assembly deforms and the whole assembly start a revolution in a big circle ([online-movie](#)). Both the assemblies parallel extensile conformation and perpendicular contractile conformation move with a certain time-period and a speed which critically depends on the activity number. The speed of the assembly, both rotation for extensile case and translation for contractile case, increase with the increase of the absolute value of activity number.

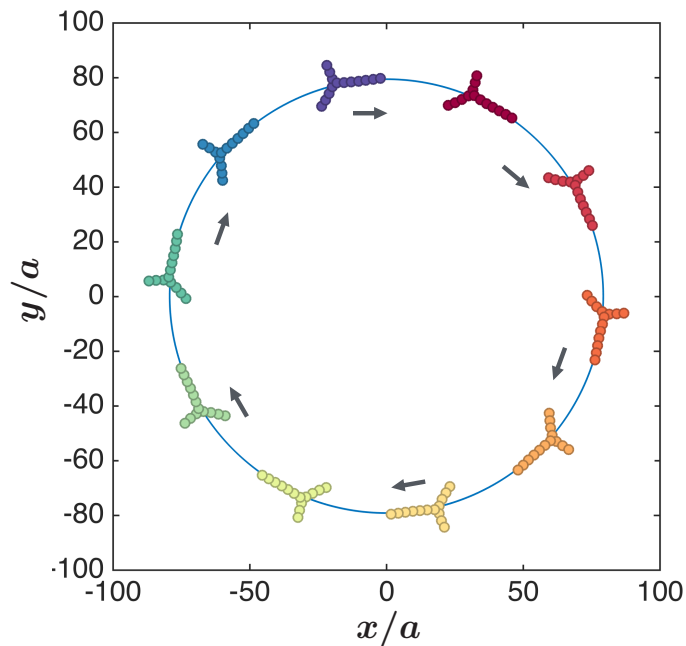


Figure 6.3: A pair of contractile rods form a stable T junction and the whole configuration start rotating in a circle. Configurations of the filaments at different instances of the time period are plotted in different colours, highlighting the rotation of the whole configuration.

These dynamics were observed earlier in [?] where the active rods both contractile and extensile were considered on a fluid film. In that case, the rods are constrained in a plane because of the geometry and not because of the up-down symmetry of the fluid domain.

6.4 Dynamics of active rods near a wall

Presence of macroscopic wall changes the dynamics of rods near a wall. As mentioned earlier, we model the hydrodynamic interaction near a macroscopic wall by computing resistance tensors, mobility tensors and propulsion tensors by taking derivatives of the finite sized Lorentz-Blake tensor which assumes no-slip boundary condition on the macroscopic wall. Modifying the boundary condition on the wall change the properties of hydrodynamic interaction and resultant dynamics.

6.4.1 Single active rod

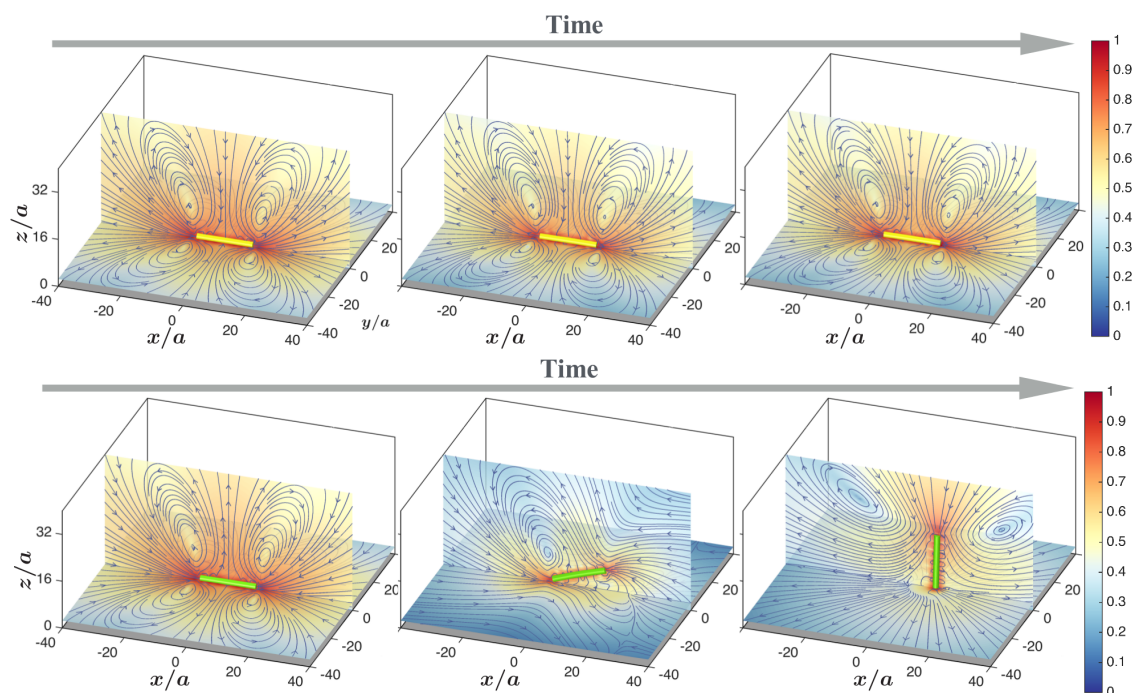


Figure 6.4: Instability of a single neutrally buoyant active rod near a wall. Due to hydrodynamic interaction with the wall, the contractile rod spontaneously reorients itself from parallel to perpendicular direction near a wall. On the other hand, an extensile rod prefers to stay in parallel to the wall.

The dynamics of a neutrally buoyant active rod near a wall is very interesting and the results are presented in the Fig. 6.4. The first row presents the dynamics of an extensile

rod while the second row presents the dynamics of a contractile rod. Columns from right to left present conformation of the rods with increasing time. Detailed dynamics can be found in [online-movie1](#) and [online-movie2](#). We found that an extensile rod is hydrodynamically stable in parallel to the wall but a contractile rod is not. In the latter case, the rod reorients itself to align perpendicular to the wall.

To elucidate the dynamics, we investigate the problem from virtual image point of view. An extensile rod generates an image which also produces extensile flow. Therefore, to a leading order, an extensile rod near a wall can be imagined as a pair of extensile rods (one real and another virtual), in parallel conformation. A pair of extensile rods in an infinite flow hydrodynamically attract each other. Therefore, the extensile rod near a wall prefer to align in parallel. On the other hand, the image created by the contractile rod produces contractile flow. We now recall that there is hydrodynamic repulsion between a pair of parallel contractile rods and an attraction when the rods are perpendicular to each other. This mechanism reorients the rod to perpendicular to the wall.

These phenomena we observed here has great implication in the dynamics of microbes near a wall. In recent studies, it is shown that microbes are neither contractile nor extensile but their nature oscillates over the swimming cycle [142, 177, 108]. Now from our study it is clear that there is an additional rate arising from hydrodynamic interaction that depends on the nature of the activity. Therefore, this fluid-mediated interaction along with other relevant time-scales will be a key factor to determining the escape time statistics of active particles near a wall [178, 179, 180, 181].

6.4.2 Two active rods

Here in this section the dynamics of a pair of active rods is studied in detail to get an understanding of emergent collective dynamics of the active rods near a wall. We initiate our numerical studies, with different possible configurations and investigate the dynamics

in detail. We choose three conformations, a) both the rods are parallel to each other and to the wall, b) both the rods are perpendicular to each other and parallel to the wall and lastly, c) both the rods parallel to each other but perpendicular to the wall.

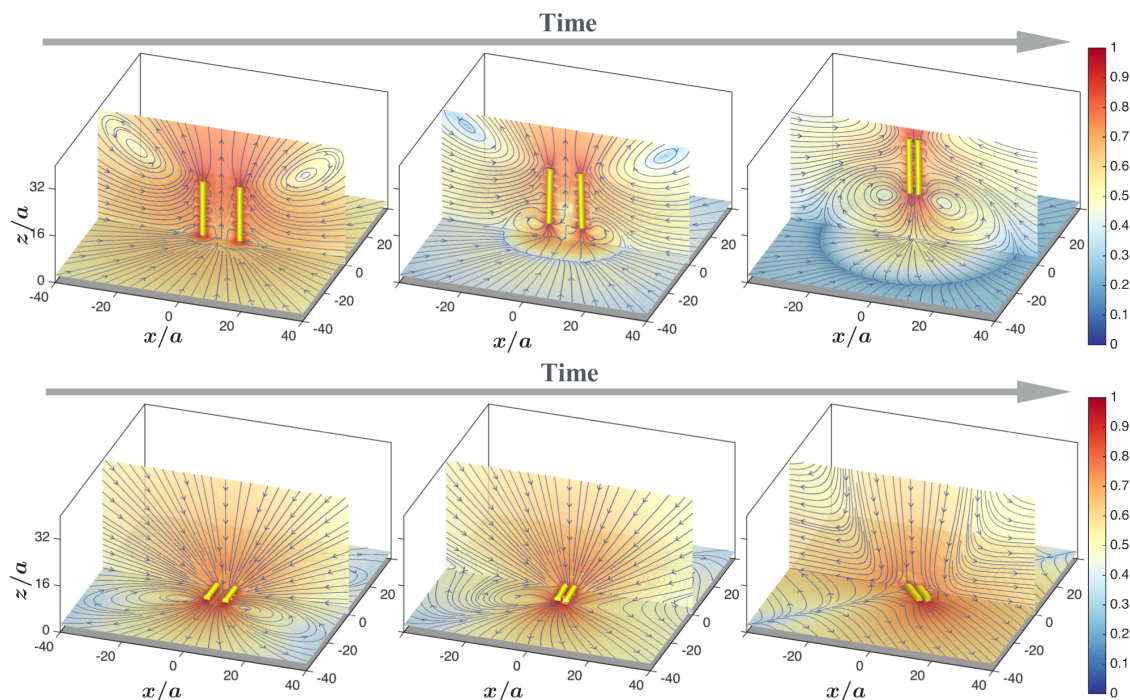


Figure 6.5: Dynamics of a pair of neutrally buoyant extensile rods near a macroscopic wall. In the first panel, we show that two parallel active rods in perpendicular to the wall, forms a stable pair and slowly drifts away from the wall. In the Second panel, we show that two parallel active rods also in parallel to the wall form a pair and goes to a quiescent state, unlike spontaneous rotation in the case of unbounded flow.

The dynamics for extensile rods are summarised in the Fig. 6.5. Individual extensile rods in parallel to the wall is hydrodynamically stable; when they are in parallel to each other, like unbounded domain, they generate a flow, that brings both the rods closer. Once the rods form an assembly, it rotates a little and become static (the first row of Fig. 6.5 and [online-movie1](#)). At high activity, they slide past each other, aligning in parallel ([online-movie2](#)). In similarity with the dynamics in infinite flow, the extensile rods in perpendicular conformation near a wall produces a repulsive flow that pushes the rods far from each other. But surprisingly, when the rods are placed in parallel, close to each

other and perpendicular to the wall, they do not reorient individually. Instead they form a pair and start moving away from the wall, due to interaction with the image of the conformation (the second row of Fig. 6.5 and [online-movie](#)).

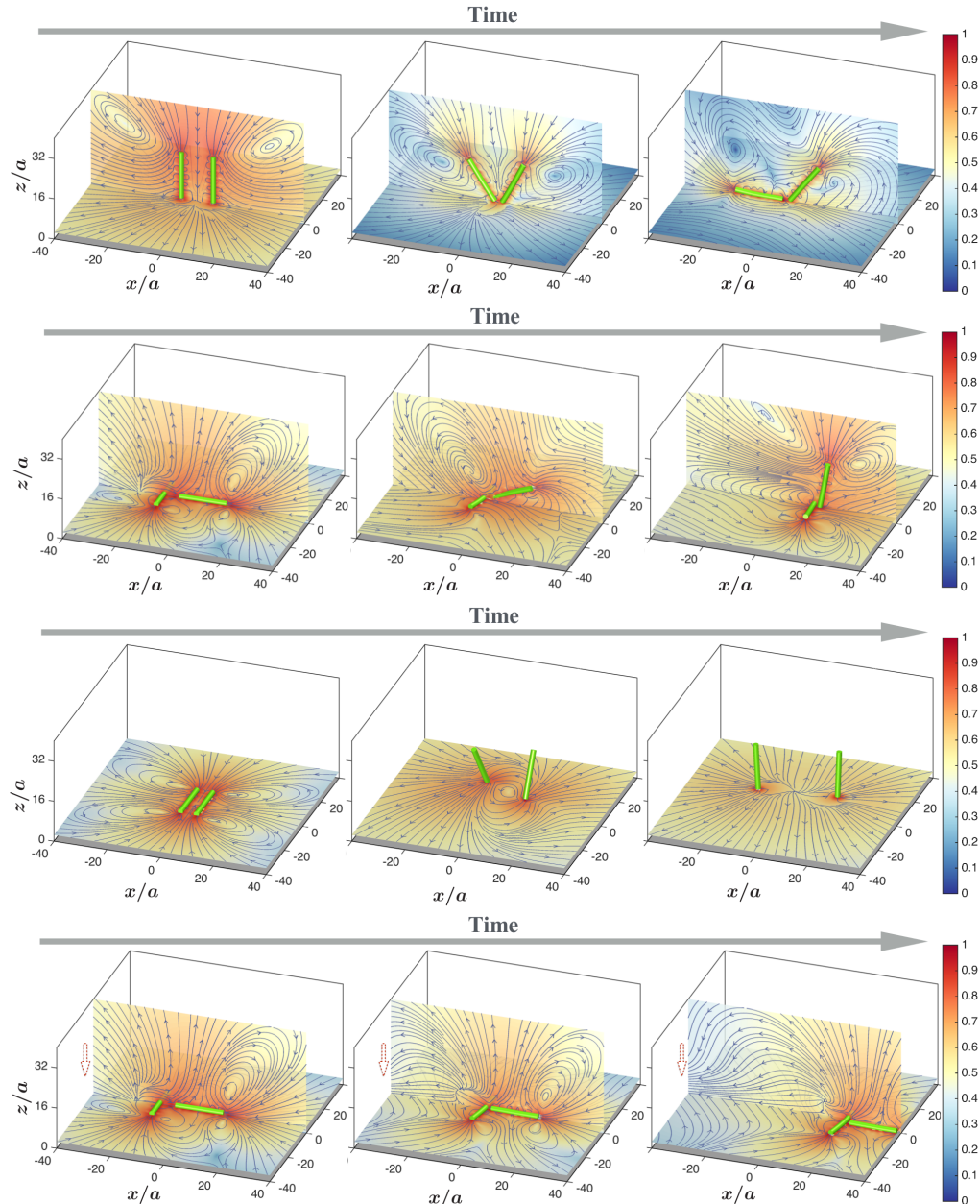


Figure 6.6: Dynamics of a pair of neutrally buoyant contractile rods near a macroscopic wall when neutrally buoyant (first three rows) and when denser than the surrounding fluid (last row). In first three panels, dynamic steady states of the pair of contractile rods are shown near a wall. In the last row, we show that like in an unbounded domain, the rods attract each other in perpendicular conformation and start translating.

Inclusion of bottom-heaviness of the rods increase the stability of the parallel conformation; we always found that the rods reorient themselves to be parallel to the wall and once it is parallel to the wall, the dynamics are similar to their infinite counterparts with rates at which they form pair or move away from each other are different.

The dynamics of contractile rods are presented in the Fig. 6.6. We have found that the dynamics of such rods, when bottom heavy, are qualitatively similar to the dynamics they produce in an infinite domain. They attract each other in perpendicular conformation (the last row of Fig. 6.6 and [online-movie](#)) and repel in parallel configuration ([online-movie](#)). They also display a new dynamical steady state when two rods aligned in a line ([online-movie](#)). But when these rods are neutrally buoyant they produce a variety of steady states due to *both* self-image interaction and pair interaction. If the rods are far away from each other they behave predominantly like isolated rods, but hydrodynamically repel each other once they get settled in their individual stable states ie. perpendicular to the wall (the third row of Fig. 6.5 and [online-movie](#)). If they are in proximity, they produces different steady states which are combinations of T-junctions and individual stable conformation (last columns of Fig. 6.6), perpendicular to the wall. Their detailed dynamics can be found in [online-movie1](#) and [online-movie2](#).

6.5 Dynamics of many active rods

Here we present the dynamics of many active rods in an infinite domain and near a wall. The dynamics observed in our numerical study depends crucially on various parameters of the system. Though the parameter space is full of interesting dynamics, here we choose one example each for contractile and extensile rods in unbounded flow and near a wall. The dynamics of the rods are restricted inside a circular domain by an additional cylindrical potential.

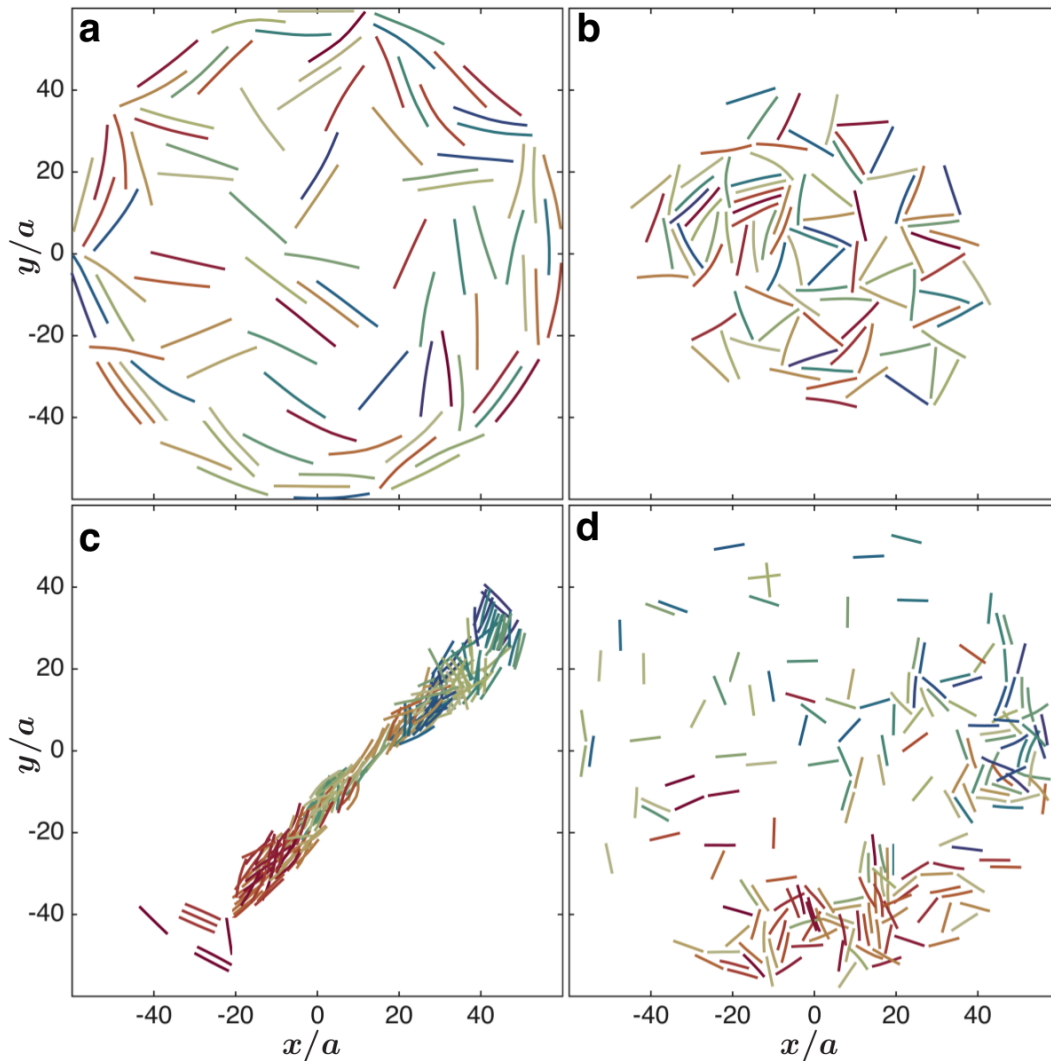


Figure 6.7: Dynamics of many active rods in infinite flow (a - extensile and b - contractile) and near a wall (c extensile and d contractile).

Extensile rods in an infinite domain : We initiate our study with an ordered structure, keeping the rods on a rectangular lattice. The dynamics can be found in the [online-movie](#). The structure with this particular configuration is not hydrodynamically stable. It undergoes an instability and a dynamical state arise when some of the rods go to the edge of the potential while the rest produce a system-wide spontaneous circulation. We recall that a pair of extensile rods forms a stable state in an infinite flow, but whenever there are more rods, pairs of rods collide among themselves which leads to the breaking of the

pairs and emergence of spontaneous circulation. This is reminiscent of spontaneous flow observed in microtubule-motor assembly [23, 45].

Contractile rods in an infinite domain : We recall from the pair dynamics that the contractile rods prefer to form T-junctions. In a collection of such type of active rods, we observe an emergence of gel-like structure where the rods form a big assembly with dynamic junctions. The dynamics is shown in the [online-movie](#). Similar dynamics is reported earlier in [?].

Extensile bottom-heavy rods near wall : In the suspension of extensile rods near a wall, we observe a dynamic assembly. We recall that in the pair dynamics parallel filaments hydrodynamically attract each other and later slips past each other. Here, the interplay between parallel attraction that enhance aggregation and slip that suppresses aggregation, leads to a oscillatory dynamics. The dynamics is presented in the [online-movie](#). The dynamics closely resembles experiment presented in [141].

Contractile bottom-heavy rods near wall : The contractile rods in the suspension near a wall display a spontaneous motion which is combination of formation of T junction and head to head alignment shown earlier in the pair dynamics. The dynamics of the collection of them is present in this [online-movie](#).

The instances of the dynamics are presented in the Fig. (6.7).

6.6 Conclusion

Here, in this chapter we have presented the collective dynamics of active rods in an infinite fluid and near a wall. The dynamics of the active rods near a wall is explained using the view point of the virtual image and the pair dynamics.

Through our modelling of active rods we have reproduced similar dynamics found in active rods near wall [141, 140]. But our model fails to produce some of the pair dynamics presented in the study of [140], as we have not considered the formation of

local bond between neighbour rods. This local bond formation changes the distribution of active flow which in turn changes the dynamics. We believe that by the inclusion of this feature in our model, it can reproduce dynamics observed in [\[140\]](#).

Conclusion

In this thesis, a formalism to study generic active slender bodies in a viscous medium is developed considering basic competing factors - elasticity of the body, Brownian motion, hydrodynamic interactions and activity. We have derived a general equation of motion for these bodies, using the properties of the viscous flow, a generic form of non-equilibrium activity occurring on the fluid-structure interface and satisfying momentum conservation. This equation of motion is an extension of the Zimm model and provides the foundation to study a suspension of active filaments.

In chapter 3, our model has produced a series of steady states which closely resemble the dynamics found in microtubule-motor assemblies. This highlights the applicability of our theory in explaining the complex dynamics of active slender bodies. There are many important and relevant questions in the systems where these bodies are in a collection. These questions include synchronisation of cilia, anomalous diffusion, enhanced mixing, spontaneous formation of ordered structure, defect dynamics and so on. It is very intriguing to explore how the infusion of local energy can modify the behaviour of hydrodynamic variables, their constitutive equations and relaxation rates.

In chapter 4, we have demonstrated the rich dynamics of an active slender body under an external field. We found spontaneous formation of complex shapes and dynamics which are consequences of the dynamic balance between conservative and dissipative forces, of both active and passive origin. We expect that dissipative hydrodynamic force will modify the collective behaviour and dynamical properties under external driving. We intend to explore them in future.

In chapter 5, we have suggested a new method to synthesise a micromachine by as-

sembling an active colloid and a passive filament. With the invention of catalytic nanomotors and other synthetic micro-motors, it is very relevant and timely to understand their individual dynamics to increase efficiency, how they could be used to accomplish different micro-scale tasks and how their collective behaviour could be controlled better. Our micromachine design is a contribution in that direction.

In chapter 6, we have demonstrated the remarkable behaviour of active slender rods near a wall. There are many experimental studies on microtubule-motor assays, spermatozoa, and other bio-filaments which show dynamic pattern formation and surprisingly counterintuitive motions near a wall. The elasticity of the body, activity and hydrodynamic interaction critically affect the outcome of those studies, which remain to be explored in detail.

Though we have developed a generic theory of slender body considering all the competitive factors, we have not explored the statistical properties of those bodies due to thermal fluctuations. We wish to explore this avenue in future along with rheological properties of active polymeric fluids.

Appendix

A.1 Constraint force on the tethered bead

Tethering the filament generates a conformation dependent constraint force at the tethered point. We take care of hydrodynamics to satisfy the boundary condition appropriately, such that net velocity of the respective end vanishes. Then we back-calculate the constrained force self-consistently on the course of simulation.

$$\begin{aligned} \dot{\mathbf{R}}_1 = & -\frac{1}{6\pi\eta a} (\nabla_1 U + \mathbf{F}_c) - \sum_{m=2}^N \mathcal{F}^0 \mathcal{F}^0 \mathbf{G}(\mathbf{R}_1, \mathbf{R}_m) \cdot \nabla_m U \\ & + \frac{28\pi\eta a^3}{3} \sum_{m=2}^N \mathcal{F}^0 \mathcal{F}^1 \nabla \mathbf{G}(\mathbf{R}_1, \mathbf{R}_m) \cdot \mathbf{s}_m \end{aligned} \quad (\text{A.1})$$

$$\begin{aligned} \mathbf{F}_c = & -\nabla_1 U - 6\pi\eta a \sum_{m=2}^N \mathcal{F}^0 \mathcal{F}^0 \mathbf{G}(\mathbf{R}_1, \mathbf{R}_m) \cdot \nabla_m U \\ & + 56\pi^2 \eta^2 a^4 \sum_{m=2}^N \mathcal{F}^0 \mathcal{F}^1 \nabla \mathbf{G}(\mathbf{R}_1, \mathbf{R}_m) \cdot \mathbf{s}_m. \end{aligned} \quad (\text{A.2})$$

A.2 Integrals and matrix elements

The expressions for the boundary integrals $\mathbf{G}^{(l)}$ and $\mathbf{K}^{(l)}$ and the matrix elements $\mathbf{G}_{nm}^{(l,l')}$ and $\mathbf{K}_{nm}^{(l,l')}$ are given as [109],

$$\mathbf{G}^{(l+1)}(\mathbf{r}, \mathbf{R}_m) = \frac{2l+1}{4\pi a^2} \int \mathbf{G}(\mathbf{r}, \mathbf{R}_m + \boldsymbol{\rho}_m) \mathbf{Y}^{(l)}(\hat{\boldsymbol{\rho}}_m) dS_m \quad (\text{A.3})$$

$$= a^l \Delta^{(l)} \mathcal{F}^l \nabla_m^{(l)} \mathbf{G}(\mathbf{r}, \mathbf{R}_m) \quad (\text{A.4})$$

$$\mathbf{K}^{(l+1)}(\mathbf{r}, \mathbf{R}_m) = \frac{1}{l!(2l-1)!!} \int \mathbf{K}(\mathbf{r}, \mathbf{R}_m + \boldsymbol{\rho}_m) \cdot \mathbf{n} \mathbf{Y}^{(l)}(\hat{\boldsymbol{\rho}}_m) dS_m \quad (\text{A.5})$$

$$= \frac{4\pi a a^l \Delta^{(l)}}{(l-1)!(2l+1)!!} \mathcal{F}^l \nabla_m^{(l-1)} \mathbf{K}(\mathbf{r}, \mathbf{R}_m) \quad (\text{A.6})$$

$$\mathbf{G}_{nm}^{(l+1, l'+1)}(\mathbf{R}_n, \mathbf{R}_m) = \begin{cases} \delta_{ll'} \frac{2l+1}{2\pi a} \int \mathbf{Y}^{(l)}(\hat{\boldsymbol{\rho}}) (\boldsymbol{\delta} - \hat{\boldsymbol{\rho}}\hat{\boldsymbol{\rho}}) \mathbf{Y}^{(l)}(\hat{\boldsymbol{\rho}}) d\Omega; & m = n; \\ a^{l+l'} \mathcal{F}_n^l \mathcal{F}_m^{l'} \nabla_n^{(l)} \nabla_m^{(l')} \mathbf{G}(\mathbf{R}_n, \mathbf{R}_m); & m \neq n; \end{cases} \quad (\text{A.7})$$

$$\mathbf{K}_{nm}^{(l+1, l'+1)}(\mathbf{R}_n, \mathbf{R}_m) = \begin{cases} -\delta_{ll'} 4\pi \delta \Delta^{(l)}; & m = n; \\ \frac{4\pi a^{(l+l'+1)}}{(l'-1)!(2l'+1)!!} \mathcal{F}_n^l \mathcal{F}_m^{l'} \nabla_n^{(l)} \nabla_m^{(l'-1)} \mathbf{K}(\mathbf{R}_n, \mathbf{R}_m); & m \neq n; \end{cases} \quad (\text{A.8})$$

A.3 Discrete form of the writhe

The discrete form of Writhe is derived in the study of protein folding by Levitt [182]. Later used by Klenin and Langowski [183] to quantify coiled DNA. We used the form given by the later,

$$W = \sum_{i=1}^N \sum_{j=1}^N \frac{\Omega_{ij}}{4\pi}. \quad (\text{A.9})$$

where $\frac{\Omega_{ij}}{4\pi}$ is equivalent of the double integral over i and j -th line-segments of the filament. This term vanishes for $i = j$ and $i = j + 1$ [183].

A.4 Simulation method and parameters

We have taken a general strategy to study the dynamics of filaments and rods. In each chapter, we first write down the equation of motion considering the competing factors, then define relevant dimensionless groups. These update equations are further integrated numerically using a variable coefficient method. We simulate the system for several hundred relaxation time scales of the relevant factor. The parameter space we used are given in the table A.1.

Chapter	Relevant dimensionless numbers	Domain and Green function	Other parameters
Chapter 3 : Dynamics	\mathcal{A}_S	Unbounded (\mathbf{G})	spring constant $k = 1$ bondlength $b_0 = 4a$ bending rigidity $\kappa = 0.1$ Monomer $Nm = 16 - 128$ stresslet $s_0 = 0 - 0.5$
Chapter 4 : External fields	$\mathcal{A}_S, \mathcal{S}$	Unbounded (\mathbf{G})	spring constant $k = 1$ bondlength $b_0 = 4a$ bending rigidity $\kappa = 0.1$ Monomer $Nm = 4 - 128$ stresslet $s_0 = 0 - 0.5$ Sedimentation number $\mathcal{S} = 0 - 2000$
Chapter 5 : Bio-mimetics	$\mathcal{A}^{(2s)}, \mathcal{A}^{(3t)}$	Unbounded (\mathbf{G})	spring constant $k = 1$ bondlength $b_0 = 4a$ bending rigidity $\kappa = 0.1$ Monomer $Nm = 32$ stresslet $s_0 = -0.5 - 0.5$ quadrupole strength $d_0 = -0.005 - 0.005$
Chapter 6 : Emergence	\mathcal{A}_S, ϕ	Wall-bounded (\mathbf{G}^w)	spring constant $k = 1$ bondlength $b_0 = 4a, 3a$ bending rigidity $\kappa = 10$ Monomer $Nm = 3 - 11$ No of rods $Np = 1 - 2^8$ stresslet $s_0 = -0.5 - 0.5$

Table A.1: Parameter range used for our numerical studies are presented here.

References

- [1] Antoni van Leeuwenhoek and Samuel Hoole. *The Select Works of Antony Van Leeuwenhoek: Containing His Microscopical Discoveries in Many of the Works of Nature*, volume 1. Whittingham and Arliss, 1816.
- [2] Robert Brown. Xxvii. a brief account of microscopical observations made in the months of june, july and august 1827, on the particles contained in the pollen of plants; and on the general existence of active molecules in organic and inorganic bodies. *Philosophical Magazine Series 2*, 4(21):161–173, 1828.
- [3] Albert Einstein. The theory of the brownian movement. *Ann. der Physik*, 17:549, 1905.
- [4] Marian Von Smoluchowski. Zur kinetischen theorie der brownschen molekularbewegung und der suspensionen. *Annalen der physik*, 326(14):756–780, 1906.
- [5] Paul Langevin. Sur la théorie du mouvement brownien. *CR Acad. Sci. Paris*, 146(530-533):530, 1908.
- [6] Albert Einstein. *Investigations on the Theory of the Brownian Movement*. Courier Corporation, 1956.
- [7] George E Uhlenbeck and Leonard S Ornstein. On the theory of the brownian motion. *Physical review*, 36(5):823, 1930.
- [8] Hannes Risken. Fokker-planck equation. In *The Fokker-Planck Equation*, pages 63–95. Springer, 1984.

- [9] Nicolaas Godfried Van Kampen. *Stochastic processes in physics and chemistry*, volume 1. Elsevier, 1992.
- [10] Sriram Ramaswamy. The mechanics and statistics of active matter. *Annual Review of Condensed Matter Physics*, 1:323–345, 2010.
- [11] MC Marchetti, JF Joanny, S Ramaswamy, TB Liverpool, J Prost, Madan Rao, and R Aditi Simha. Hydrodynamics of soft active matter. *Reviews of Modern Physics*, 85(3):1143, 2013.
- [12] David Saintillan and Michael J Shelley. Active suspensions and their nonlinear models. *Comptes Rendus Physique*, 14(6):497–517, 2013.
- [13] Jens Elgeti, Roland G Winkler, and Gerhard Gompper. Physics of microswimmers-single particle motion and collective behavior: a review. *Reports on progress in physics*, 78(5):056601, 2015.
- [14] Christopher Brennen and Howard Winet. Fluid mechanics of propulsion by cilia and flagella. *Annual Review of Fluid Mechanics*, 9(1):339–398, 1977.
- [15] Michael Silverman and Melvin Simon. Flagellar rotation and the mechanism of bacterial motility. *Nature*, 249:73–74, 1974.
- [16] CJ Brokaw. Bending moments in free-swimming flagella. *Journal of Experimental Biology*, 53(2):445–464, 1970.
- [17] CJ Brokaw. Non-sinusoidal bending waves of sperm flagella. *Journal of Experimental Biology*, 43(1):155–169, 1965.
- [18] KE Machin. Wave propagation along flagella. *J. exp. Biol*, 35(4):796–806, 1958.

-
- [19] Sébastien Camalet, Frank Jülicher, and Jacques Prost. Self-organized beating and swimming of internally driven filaments. *Physical review letters*, 82(7):1590, 1999.
- [20] Sébastien Camalet and Frank Jülicher. Generic aspects of axonemal beating. *New Journal of Physics*, 2(1):24, 2000.
- [21] Ingmar H Riedel-Kruse, Andreas Hilfinger, Jonathon Howard, and Frank Jülicher. How molecular motors shape the flagellar beat. *HFSP journal*, 1(3):192–208, 2007.
- [22] Naïs Coq, Antoine Bricard, Francois-Damien Delapierre, Laurent Malaquin, Olivia Du Roure, Marc Fermigier, and Denis Bartolo. Collective beating of artificial microcilia. *Physical review letters*, 107(1):014501, 2011.
- [23] Timothy Sanchez, David Welch, Daniela Nicastro, and Zvonimir Dogic. Cilia-like beating of active microtubule bundles. *Science*, 333(6041):456–459, 2011.
- [24] Shay Gueron, Konstantin Levit-Gurevich, Nadav Liron, and Jacob J Blum. Cilia internal mechanism and metachronal coordination as the result of hydrodynamical coupling. *Proceedings of the National Academy of Sciences*, 94(12):6001–6006, 1997.
- [25] Shay Gueron and Konstantin Levit-Gurevich. Energetic considerations of ciliary beating and the advantage of metachronal coordination. *Proceedings of the National Academy of Sciences*, 96(22):12240–12245, 1999.
- [26] Mojca Vilfan, Anton Potočnik, Blaž Kavčič, Natan Osterman, Igor Poberaj, Andrej Vilfan, and Dušan Babič. Self-assembled artificial cilia. *Proceedings of the National Academy of Sciences*, 107(5):1844–1847, 2010.

- [27] Charles B Lindemann and Robert Rikmenspoel. Sperm flagella: autonomous oscillations of the contractile system. *Science*, 175(4019):337–338, 1972.
- [28] Matthew Bessen, Rose B Fay, and George B Witman. Calcium control of waveform in isolated flagellar axonemes of chlamydomonas. *The Journal of Cell Biology*, 86(2):446–455, 1980.
- [29] Rémi Dreyfus, Jean Baudry, Marcus L Roper, Marc Fermigier, Howard A Stone, and Jérôme Bibette. Microscopic artificial swimmers. *Nature*, 437(7060):862–865, 2005.
- [30] Gabriel Loget and Alexander Kuhn. Electric field-induced chemical locomotion of conducting objects. *Nature communications*, 2:535, 2011.
- [31] Wei Wang, Luz Angelica Castro, Mauricio Hoyos, and Thomas E Mallouk. Autonomous motion of metallic microrods propelled by ultrasound. *ACS nano*, 6(7):6122–6132, 2012.
- [32] Alexander A Solovev, Samuel Sanchez, and Oliver G Schmidt. Collective behaviour of self-propelled catalytic micromotors. *Nanoscale*, 5(4):1284–1293, 2013.
- [33] Jahir Orozco, Cortès Allan, Guanzhi Cheng, Sirilak Sattayasamitsathit, Wei Gao, Xiaomiao Feng, Yufeng Shen, and Joseph Wang. Molecularly imprinted polymer-based catalytic micromotors for selective protein transport. *Journal of the American Chemical Society*, 135(14):5336–5339, 2013.
- [34] Wei Wang, Wentao Duan, Suzanne Ahmed, Thomas E Mallouk, and Ayusman Sen. Small power: Autonomous nano-and micromotors propelled by self-generated gradients. *Nano Today*, 8(5):531–554, 2013.

-
- [35] Brian J Williams, Sandeep V Anand, Jagannathan Rajagopalan, and M Taher A Saif. A self-propelled biohybrid swimmer at low Reynolds number. *Nature communications*, 5, 2014.
- [36] Christopher Dombrowski, Luis Cisneros, Sunita Chatkaew, Raymond E Goldstein, and John O Kessler. Self-concentration and large-scale coherence in bacterial dynamics. *Physical Review Letters*, 93(9):098103, 2004.
- [37] Xiao-Lun Wu and Albert Libchaber. Particle diffusion in a quasi-two-dimensional bacterial bath. *Physical Review Letters*, 84(13):3017, 2000.
- [38] Andrey Sokolov, Igor S Aranson, John O Kessler, and Raymond E Goldstein. Concentration dependence of the collective dynamics of swimming bacteria. *Physical Review Letters*, 98(15):158102, 2007.
- [39] Francis G Woodhouse and Raymond E Goldstein. Spontaneous circulation of confined active suspensions. *Physical review letters*, 109(16):168105, 2012.
- [40] Hugo Wioland, Francis G Woodhouse, Jörn Dunkel, John O Kessler, and Raymond E Goldstein. Confinement stabilizes a bacterial suspension into a spiral vortex. *Physical review letters*, 110(26):268102, 2013.
- [41] Francis G Woodhouse and Raymond E Goldstein. Cytoplasmic streaming in plant cells emerges naturally by microfilament self-organization. *Proceedings of the National Academy of Sciences*, 110(35):14132–14137, 2013.
- [42] Henricus H Wensink, Jörn Dunkel, Sebastian Heidenreich, Knut Drescher, Raymond E Goldstein, Hartmut Löwen, and Julia M Yeomans. Meso-scale turbulence in living fluids. *Proceedings of the National Academy of Sciences*, 109(36):14308–14313, 2012.

- [43] Volker Schaller, Christoph Weber, Christine Semmrich, Erwin Frey, and Andreas R Bausch. Polar patterns of driven filaments. *Nature*, 467(7311):73–77, 2010.
- [44] Yutaka Sumino, Ken H Nagai, Yuji Shitaka, Dan Tanaka, Kenichi Yoshikawa, Hugues Chaté, and Kazuhiro Oiwa. Large-scale vortex lattice emerging from collectively moving microtubules. *Nature*, 483(7390):448–452, 2012.
- [45] Tim Sanchez, Daniel TN Chen, Stephen J DeCamp, Michael Heymann, and Zvonimir Dogic. Spontaneous motion in hierarchically assembled active matter. *Nature*, 491(7424):431–434, 2012.
- [46] Felix C Keber, Etienne Loiseau, Tim Sanchez, Stephen J DeCamp, Luca Giomi, Mark J Bowick, M Cristina Marchetti, Zvonimir Dogic, and Andreas R Bausch. Topology and dynamics of active nematic vesicles. *Science*, 345(6201):1135–1139, 2014.
- [47] Jeremie Palacci, Stefano Sacanna, Asher Preska Steinberg, David J Pine, and Paul M Chaikin. Living crystals of light-activated colloidal surfers. *Science*, 339(6122):936–940, 2013.
- [48] Ivo Buttinoni, Julian Bialké, Felix Kümmel, Hartmut Löwen, Clemens Bechinger, and Thomas Speck. Dynamical clustering and phase separation in suspensions of self-propelled colloidal particles. *Physical review letters*, 110(23):238301, 2013.
- [49] I Theurkauff, C Cottin-Bizonne, J Palacci, C Ybert, and L Bocquet. Dynamic clustering in active colloidal suspensions with chemical signaling. *Physical Review Letters*, 108(26):268303, 2012.
- [50] Alexander P Petroff, Xiao-Lun Wu, and Albert Libchaber. Fast-moving bacteria self-organize into active two-dimensional crystals of rotating cells. *Physical*

-
- review letters*, 114(15):158102, 2015.
- [51] Andrey Sokolov and Igor S Aranson. Reduction of viscosity in suspension of swimming bacteria. *Physical Review Letters*, 103(14):148101, 2009.
- [52] Augustus Edward Hough Love. *A treatise on the mathematical theory of elasticity*, volume 1. Cambridge University Press, 2013.
- [53] Raymond E Goldstein, Alain Goriely, Greg Huber, and Charles W Wolgemuth. Bistable helices. *Physical Review Letters*, 84(7):1631, 2000.
- [54] Reinhard Vogel and Holger Stark. Force-extension curves of bacterial flagella. *The European Physical Journal E*, 33(3):259–271, 2010.
- [55] KE Machin. The control and synchronization of flagellar movement. *Proceedings of the Royal Society of London B: Biological Sciences*, 158(970):88–104, 1963.
- [56] Robert Rikmenspoel. The tail movement of bull spermatozoa: Observations and model calculations. *Biophysical journal*, 5(4):365, 1965.
- [57] Henry C Fu, Charles W Wolgemuth, and Thomas R Powers. Beating patterns of filaments in viscoelastic fluids. *Physical Review E*, 78(4):041913, 2008.
- [58] J Gray and GJ Hancock. The propulsion of sea-urchin spermatozoa. *Journal of Experimental Biology*, 32(4):802–814, 1955.
- [59] Joseph B Keller and Sol I Rubinow. Slender-body theory for slow viscous flow. *J. Fluid Mech*, 75(4):705–714, 1976.
- [60] Robert E Johnson. An improved slender-body theory for stokes flow. *Journal of Fluid Mechanics*, 99(02):411–431, 1980.
- [61] Raymond E Goldstein, Thomas R Powers, and Chris H Wiggins. Viscous nonlinear dynamics of twist and writhe. *Physical Review Letters*, 80(23):5232, 1998.

- [62] Charles W Wolgemuth, Thomas R Powers, and Raymond E Goldstein. Twirling and whirling: Viscous dynamics of rotating elastic filaments. *Physical Review Letters*, 84(7):1623, 2000.
- [63] Manoel Manghi, Xaver Schlagberger, and Roland R Netz. Propulsion with a rotating elastic nanorod. *Physical review letters*, 96(6):068101, 2006.
- [64] Hendrik Anthony Kramers. The behavior of macromolecules in inhomogeneous flow. *The Journal of Chemical Physics*, 14(7):415–424, 1946.
- [65] Prince E Rouse Jr. A theory of the linear viscoelastic properties of dilute solutions of coiling polymers. *The Journal of Chemical Physics*, 21(7):1272–1280, 1953.
- [66] Bruno H Zimm. Dynamics of polymer molecules in dilute solution: viscoelasticity, flow birefringence and dielectric loss. *The journal of chemical physics*, 24(2):269–278, 1956.
- [67] Masao Doi. *The theory of polymer dynamics*. Number 73. oxford university press, 1988.
- [68] David M Woolley, Rachel F Crockett, William DI Groom, and Stuart G Revell. A study of synchronisation between the flagella of bull spermatozoa, with related observations. *Journal of Experimental Biology*, 212(14):2215–2223, 2009.
- [69] Charles J Brokaw. Thinking about flagellar oscillation. *Cell motility and the cytoskeleton*, 66(8):425–436, 2009.
- [70] Larisa Gheber and Zvi Priel. Synchronization between beating cilia. *Biophysical journal*, 55(1):183, 1989.
- [71] Douglas R Brumley, Marco Polin, Timothy J Pedley, and Raymond E Goldstein.

-
- Hydrodynamic synchronization and metachronal waves on the surface of the colonial alga *Volvox carteri*. *Physical review letters*, 109(26):268102, 2012.
- [72] Douglas R Brumley, Marco Polin, Timothy J Pedley, and Raymond E Goldstein. Metachronal waves in the flagellar beating of *Volvox* and their hydrodynamic origin. *Journal of The Royal Society Interface*, 12(108):20141358, 2015.
- [73] Douglas R Brumley, Kirsty Y Wan, Marco Polin, and Raymond E Goldstein. Flagellar synchronization through direct hydrodynamic interactions. *Elife*, 3:e02750, 2014.
- [74] Makoto Okuno and Yukio Hiramoto. Mechanical stimulation of starfish sperm flagella. *Journal of Experimental Biology*, 65(2):401–413, 1976.
- [75] Raymond E Goldstein, Marco Polin, and Idan Tuval. Noise and synchronization in pairs of beating eukaryotic flagella. *Physical review letters*, 103(16):168103, 2009.
- [76] James Lighthill. Flagellar hydrodynamics. *SIAM review*, 18(2):161–230, 1976.
- [77] Rothchild. Measurement of sperm activity before artificial insemination. *Nature*, 163(4140):358–359, 1949.
- [78] FJ Nédélec, Thomas Surrey, Anthony C Maggs, and Stanislas Leibler. Self-organization of microtubules and motors. *Nature*, 389(6648):305–308, 1997.
- [79] Virendra V Singh and Joseph Wang. Nano/micromotors for security/defense applications. a review. *Nanoscale*, 7(46):19377–19389, 2015.
- [80] Hong Wang, Guanxia Zhao, and Martin Pumera. Beyond platinum: Bubble-propelled micromotors based on Ag and MnO₂ catalysts. *Journal of the American Chemical Society*, 136(7):2719–2722, 2014.

- [81] Krishna K Dey, Xi Zhao, Benjamin M Tansi, Wilfredo J Méndez-Ortiz, Ubaldo M Córdova-Figueroa, Ramin Golestanian, and Ayusman Sen. Micromotors powered by enzyme catalysis. *Nano letters*, 15(12):8311–8315, 2015.
- [82] Wei Gao and Joseph Wang. The environmental impact of micro/nanomachines: a review. *Acs Nano*, 8(4):3170–3180, 2014.
- [83] Hong Wang, James Guo Sheng Moo, and Martin Pumera. From nanomotors to micromotors: The influence of the size of an autonomous bubble-propelled device upon its motion. *ACS nano*, 2016.
- [84] Wentao Duan, Wei Wang, Sambaeta Das, Vinita Yadav, Thomas E Mallouk, and Ayusman Sen. Synthetic nano-and micromachines in analytical chemistry: Sensing, migration, capture, delivery, and separation. *Annual Review of Analytical Chemistry*, 8:311–333, 2015.
- [85] Hassan Masoud, Benjamin I Bingham, and Alexander Alexeev. Designing maneuverable micro-swimmers actuated by responsive gel. *Soft Matter*, 8(34):8944–8951, 2012.
- [86] Gayathri Jayaraman, Sanoop Ramachandran, Somdeb Ghose, Abhrajit Laskar, M Saad Bhamla, PB Sunil Kumar, and R Adhikari. Autonomous motility of active filaments due to spontaneous flow-symmetry breaking. *Physical review letters*, 109(15):158302, 2012.
- [87] Abhrajit Laskar, Rajeev Singh, Somdeb Ghose, Gayathri Jayaraman, PB Sunil Kumar, and R Adhikari. Hydrodynamic instabilities provide a generic route to spontaneous biomimetic oscillations in chemomechanically active filaments. *Scientific reports*, 3, 2013.

-
- [88] Abhrajit Laskar and R Adhikari. Brownian microhydrodynamics of active filaments. *Soft matter*, 11(47):9073–9085, 2015.
- [89] Raghunath Chelakkot, Arvind Gopinath, L Mahadevan, and Michael F Hagan. Flagellar dynamics of a connected chain of active, polar, Brownian particles. *Journal of The Royal Society Interface*, 11(92):20130884, 2014.
- [90] Rolf E Isele-Holder, Jens Elgeti, and Gerhard Gompper. Self-propelled worm-like filaments: spontaneous spiral formation, structure, and dynamics. *Soft matter*, 11(36):7181–7190, 2015.
- [91] Huijun Jiang and Zhonghuai Hou. Hydrodynamic interaction induced spontaneous rotation of coupled active filaments. *Soft matter*, 10(46):9248–9253, 2014.
- [92] Huijun Jiang and Zhonghuai Hou. Motion transition of active filaments: rotation without hydrodynamic interactions. *Soft Matter*, 10(7):1012–1017, 2014.
- [93] Blaise Delmotte, Eric Climent, and Franck Plouraboué. A general formulation of bead models applied to flexible fibers and active filaments at low reynolds number. *Journal of Computational Physics*, 286:14–37, 2015.
- [94] Debarati Sarkar and Snigdha Thakur. Coarse-grained simulations of an active filament propelled by a self-generated solute gradient. *Physical Review E*, 93(3):032508, 2016.
- [95] Edward M Purcell. Life at low reynolds number. *Am. J. Phys*, 45(1):3–11, 1977.
- [96] Augustin Louis Baron Cauchy. *Research on the balance and inner movement of elastic or inelastic solids or fluids*. Bull Soc Philomath, Paris 9, 1823.
- [97] Leo Graetz M Smoluchowski. *Handbuch der Elektrizität und des Magnetismus*, edited by Graetz, Leipzig, volume 2. 1914.

- [98] BV Deryagin, SS Dukhin, and AA Korotkova. Diffusiophoresis in electrolyte solutions and its role in mechanism of film formation from rubber latexes by method of ionic deposition. *Kolloidnyi Zhurnal*, 23(1):53, 1961.
- [99] BV Derjaguin, IE Dzyaloshinsky, MM Koptelova, and LP Pitayevsky. Molecular-surface forces in binary solutions. *Discussions of the Faraday Society*, 40:246–252, 1965.
- [100] John L Anderson. Colloid transport by interfacial forces. *Annual review of fluid mechanics*, 21(1):61–99, 1989.
- [101] John L Anderson and Dennis C Prieve. Diffusiophoresis caused by gradients of strongly adsorbing solutes. *Langmuir*, 7(2):403–406, 1991.
- [102] BV Derjaguin, GP Sidorenkov, EA Zubashchenkov, and EV Kiseleva. Kinetic phenomena in boundary films of liquids. *Kolloidn. zh*, 9:335–347, 1947.
- [103] Debarati Sarkar, Snigdha Thakur, Yu-Guo Tao, and Raymond Kapral. Ring closure dynamics for a chemically active polymer. *Soft Matter*, 10(47):9577–9584, 2014.
- [104] R Golestanian, TB Liverpool, and A Ajdari. Designing phoretic micro-and nano-swimmers. *New Journal of Physics*, 9(5):126, 2007.
- [105] MJ Lighthill. On the squirming motion of nearly spherical deformable bodies through liquids at very small reynolds numbers. *Communications on Pure and Applied Mathematics*, 5(2):109–118, 1952.
- [106] JR Blake. A spherical envelope approach to ciliary propulsion. *Journal of Fluid Mechanics*, 46(01):199–208, 1971.

-
- [107] Takuji Ishikawa, MP Simmonds, and TJ Pedley. Hydrodynamic interaction of two swimming model micro-organisms. *Journal of Fluid Mechanics*, 568:119–160, 2006.
- [108] Somdeb Ghose and R Adhikari. Irreducible representations of oscillatory and swirling flows in active soft matter. *Physical review letters*, 112(11):118102, 2014.
- [109] Rajesh Singh, Somdeb Ghose, and R Adhikari. Many-body microhydrodynamics of colloidal particles with active boundary layers. *Journal of Statistical Mechanics: Theory and Experiment*, 2015, 2014.
- [110] Rajesh Singh and R Adhikari. Traction relations for active colloids and their application. *arXiv preprint arXiv:1603.05735*, 2016.
- [111] BU Felderhof. Stokesian swimmers and active particles. *arXiv:1502.00242*, 2015.
- [112] Howard A Stone and Aravinthan DT Samuel. Propulsion of microorganisms by surface distortions. *Physical review letters*, 77(19):4102, 1996.
- [113] Olga Aleksandrovna Ladyzhenskaya. *The boundary value problems of mathematical physics*, volume 49. Springer Science & Business Media, 2013.
- [114] Constantine Pozrikidis. *Boundary integral and singularity methods for linearized viscous flow*. Cambridge University Press, 1992.
- [115] HA Lorentz. *Zittingsverlag akad. v. Wet.* 5, 168, 1896.
- [116] JR Blake. A note on the image system for a stokeslet in a no-slip boundary. In *Mathematical Proceedings of the Cambridge Philosophical Society*, volume 70, pages 303–310. Cambridge Univ Press, 1971.

- [117] TJ Murphy and JL Aguirre. Brownian motion of n interacting particles. i. extension of the einstein diffusion relation to the n -particle case. *The Journal of Chemical Physics*, 57(5):2098–2104, 1972.
- [118] Donald L Ermak and JA McCammon. Brownian dynamics with hydrodynamic interactions. *The Journal of chemical physics*, 69(4):1352–1360, 1978.
- [119] Jens Rotne and Stephen Prager. Variational treatment of hydrodynamic interaction in polymers. *The Journal of Chemical Physics*, 50(11):4831–4837, 1969.
- [120] Hiromi Yamakawa. Transport properties of polymer chains in dilute solution: hydrodynamic interaction. *The Journal of Chemical Physics*, 53(1):436–443, 1970.
- [121] John G Kirkwood and Jacob Riseman. The intrinsic viscosities and diffusion constants of flexible macromolecules in solution. *The Journal of Chemical Physics*, 16(6):565–573, 1948.
- [122] Takenao Yoshizaki and Hiromi Yamakawa. Validity of the superposition approximation in an application of the modified oseen tensor to rigid polymers. *The Journal of Chemical Physics*, 73(1):578–582, 1980.
- [123] Andreas Kaiser, Sonja Babel, Borge ten Hagen, Christian von Ferber, and Hartmut Löwen. How does a flexible chain of active particles swell? *The Journal of chemical physics*, 142(12):124905, 2015.
- [124] Rajesh Singh, Abhrajit Laskar, and R. Adhikari. Pystokes: Hampi, 2014.
- [125] Josue Sznitman, Xiaoning Shen, Prashant K Purohit, and Paulo E Arratia. The effects of fluid viscosity on the kinematics and material properties of *c. elegans* swimming at low reynolds number. *Experimental Mechanics*, 50(9):1303–1311, 2010.

-
- [126] Bian Qian, Thomas R Powers, and Kenneth S Breuer. Shape transition and propulsive force of an elastic rod rotating in a viscous fluid. *Physical review letters*, 100(7):078101, 2008.
- [127] MK Jawed, NK Khouri, F Da, E Grinspun, and PM Reis. Propulsion and instability of a flexible helical rod rotating in a viscous fluid. *Physical review letters*, 115(16):168101, 2015.
- [128] Bumjin Jang, Emiliya Gutman, Nicolai Stucki, Benedikt F Seitz, Pedro D Wendel-García, Taylor Newton, Juho Pokki, Olgacİğ Ergeneman, Salvador PaneİA, Yizhar Or, et al. Undulatory locomotion of magnetic multilink nanoswimmers. *Nano letters*, 15(7):4829–4833, 2015.
- [129] Wei Gao, Sirilak Sattayasamitsathit, Kalayil Manian Manesh, Daniel Weihs, and Joseph Wang. Magnetically powered flexible metal nanowire motors. *Journal of the American Chemical Society*, 132(41):14403–14405, 2010.
- [130] Veronika Magdanz, Samuel Sanchez, and Oliver G Schmidt. Development of a sperm-flagella driven micro-bio-robot. *Advanced Materials*, 25(45):6581–6588, 2013.
- [131] Mariana Medina-Sánchez, Lukas Schwarz, Anne K Meyer, Franziska Hebenstreit, and Oliver G Schmidt. Cellular cargo delivery: toward assisted fertilization by sperm-carrying micromotors. *Nano letters*, 16(1):555–561, 2015.
- [132] Alexander M Maier, Cornelius Weig, Peter Oswald, Erwin Frey, Peer Fischer, and Tim Liedl. Magnetic propulsion of microswimmers with dna-based flagellar bundles. *Nano letters*, 16(2):906–910, 2016.
- [133] Apabrita Mallick, Dipti Lai, and Soumyajit Roy. Autonomous movement induced

- in chemically powered active soft-oxometalates using dithionite as fuel. *New Journal of Chemistry*, 40(2):1057–1062, 2016.
- [134] Sidney L Tamm. Mechanical synchronization of ciliary beating within comb plates of ctenophores. *Journal of experimental biology*, 113(1):401–408, 1984.
- [135] Charles J Brokaw. Microtubule sliding in swimming sperm flagella: direct and indirect measurements on sea urchin and tunicate spermatozoa. *The Journal of cell biology*, 114(6):1201–1215, 1991.
- [136] Timothy Sanchez and Zvonimir Dogic. Engineering oscillating microtubule bundles. *Methods Enzymol.*, 254:205–224, 2013.
- [137] Howard C Berg and Robert A Anderson. Bacteria swim by rotating their flagellar filaments. *nature*, 245:380–382, 1973.
- [138] Howard C Berg. The rotary motor of bacterial flagella. *Biochemistry*, 72(1):19, 2003.
- [139] Miki Fujimura and Makoto Okuno. Requirement of the fixed end for spontaneous beating in flagella. *Journal of experimental biology*, 209(7):1336–1343, 2006.
- [140] Megan S Davies Wykes, Jérémie Palacci, Takuji Adachi, Leif Ristroph, Xiao Zhong, Michael D Ward, Jun Zhang, and Michael J Shelley. Dynamic self-assembly of microscale rotors and swimmers. *Soft Matter*, 12(20):4584–4589, 2016.
- [141] Erik L Jewell, Wei Wang, and Thomas E Mallouk. Catalytically driven assembly of trisegmented metallic nanorods and polystyrene tracer particles. *Soft matter*, 12(9):2501–2504, 2016.

-
- [142] Knut Drescher, Raymond E Goldstein, Nicolas Michel, Marco Polin, and Idan Tuval. Direct measurement of the flow field around swimming microorganisms. *Physical Review Letters*, 105(16):168101, 2010.
- [143] Walter F Paxton, Kevin C Kistler, Christine C Olmeda, Ayusman Sen, Sarah K St. Angelo, Yanyan Cao, Thomas E Mallouk, Paul E Lammert, and Vincent H Crespi. Catalytic nanomotors: autonomous movement of striped nanorods. *Journal of the American Chemical Society*, 126(41):13424–13431, 2004.
- [144] Javier Vicario, Rienk Eelkema, Wesley R Browne, Auke Meetsma, René M La Crois, and Ben L Feringa. Catalytic molecular motors: fuelling autonomous movement by a surface bound synthetic manganese catalase. *Chemical communications*, (31):3936–3938, 2005.
- [145] Geoffrey A Ozin, Ian Manners, Sébastien Fournier-Bidoz, and André Arsenault. Dream nanomachines. *Advanced Materials*, 17(24):3011–3018, 2005.
- [146] Jeffrey M Catchmark, Shyamala Subramanian, and Ayusman Sen. Directed rotational motion of microscale objects using interfacial tension gradients continually generated via catalytic reactions. *Small*, 1(2):202–206, 2005.
- [147] BA Finlayson and LE Scriven. Convective instability by active stress. In *Proceedings of the Royal Society of London A: Mathematical, Physical and Engineering Sciences*, volume 310, pages 183–219. The Royal Society, 1969.
- [148] Xianghua Xu and Ali Nadim. Deformation and orientation of an elastic slender body sedimenting in a viscous liquid. *Physics of Fluids (1994-present)*, 6(9):2889–2893, 1994.
- [149] M Cosentino Lagomarsino, I Pagonabarraga, and CP Lowe. Hydrodynamic induced deformation and orientation of a microscopic elastic filament. *Physical*

-
- review letters*, 94(14):148104, 2005.
- [150] X Schlagberger and RR Netz. Orientation of elastic rods in homogeneous stokes flow. *EPL (Europhysics Letters)*, 70(1):129, 2005.
- [151] Xaver Schlagberger and Roland R Netz. Anomalous polymer sedimentation far from equilibrium. *Physical review letters*, 98(12):128301, 2007.
- [152] Lei Li, Harishankar Manikantan, David Saintillan, and Saverio E Spagnolie. The sedimentation of flexible filaments. *Journal of Fluid Mechanics*, 735:705–736, 2013.
- [153] Behzad Shojaei and Hamid Dehghani. The sedimentation of slim flexible particles in stokes flow. *Indian Journal of Science and Technology*, 8(28):1, 2015.
- [154] Guglielmo Saggiorato, Jens Elgeti, Roland G Winkler, and Gerhard Gompper. Conformations, hydrodynamic interactions, and instabilities of sedimenting semi-flexible filaments. *Soft matter*, 11(37):7337–7344, 2015.
- [155] Marcus Roper, Rémi Dreyfus, Jean Baudry, Marc Fermigier, Jérôme Bibette, and Howard A Stone. On the dynamics of magnetically driven elastic filaments. *Journal of Fluid Mechanics*, 554:167–190, 2006.
- [156] Maria Guix, Carmen C Mayorga-Martinez, and Arben Merkoçi. Nano/micromotors in (bio) chemical science applications. *Chemical reviews*, 114(12):6285–6322, 2014.
- [157] Suk Tai Chang, Erin Beaumont, Dimiter N Petsev, and Orlin D Velez. Remotely powered distributed microfluidic pumps and mixers based on miniature diodes. *Lab on a Chip*, 8(1):117–124, 2008.

-
- [158] Percy Calvo-Marzal, Sirilak Sattayasamitsathit, Shankar Balasubramanian, Joshua R Windmiller, Cuong Dao, and Joseph Wang. Propulsion of nanowire diodes. *Chemical Communications*, 46(10):1623–1624, 2010.
- [159] Ambarish Ghosh and Peer Fischer. Controlled propulsion of artificial magnetic nanostructured propellers. *Nano letters*, 9(6):2243–2245, 2009.
- [160] BA Evans, AR Shields, R Lloyd Carroll, S Washburn, MR Falvo, and R Superfine. Magnetically actuated nanorod arrays as biomimetic cilia. *Nano letters*, 7(5):1428–1434, 2007.
- [161] Victor Garcia-Gradilla, Jahir Orozco, Sirilak Sattayasamitsathit, Fernando Soto, Filiz Kuralay, Ashley Pourazary, Adlai Katzenberg, Wei Gao, Yufeng Shen, and Joseph Wang. Functionalized ultrasound-propelled magnetically guided nanomotors: Toward practical biomedical applications. *ACS nano*, 7(10):9232–9240, 2013.
- [162] Manoj Manjare, Bo Yang, and Y-P Zhao. Bubble driven quasioscillatory translational motion of catalytic micromotors. *Physical review letters*, 109(12):128305, 2012.
- [163] E Hendarto and YB Gianchandani. Marangoni-driven micromotor in liquid medium. In *2011 16th International Solid-State Sensors, Actuators and Microsystems Conference*, pages 246–249. IEEE, 2011.
- [164] Chris H Wiggins and Raymond E Goldstein. Flexive and propulsive dynamics of elastica at low reynolds number. *Physical review letters*, 80(17):3879–3882, 1998.
- [165] Peidong Yang, Tao Deng, Dongyuan Zhao, Pingyun Feng, David Pine, Bradley F Chmelka, George M Whitesides, and Galen D Stucky. Hierarchically ordered oxides. *science*, 282(5397):2244–2246, 1998.

-
- [166] Younan Xia, Yujie Xiong, Byungkwon Lim, and Sara E Skrabalak. Shape-controlled synthesis of metal nanocrystals: Simple chemistry meets complex physics? *Angewandte Chemie International Edition*, 48(1):60–103, 2009.
- [167] Qian Chen, Sung Chul Bae, and Steve Granick. Directed self-assembly of a colloidal kagome lattice. *Nature*, 469(7330):381–384, 2011.
- [168] Zhenli Zhang and Sharon C Glotzer. Self-assembly of patchy particles. *Nano Letters*, 4(8):1407–1413, 2004.
- [169] Sharon C Glotzer and Michael J Solomon. Anisotropy of building blocks and their assembly into complex structures. *Nature materials*, 6(8):557–562, 2007.
- [170] Jonathan S Lindsey. Self-assembly in synthetic routes to molecular devices. biological principles and chemical perspectives: a review. *New J. Chem*, 15(2-3):153–179, 1991.
- [171] George M Whitesides and Bartosz Grzybowski. Self-assembly at all scales. *Science*, 295(5564):2418–2421, 2002.
- [172] He-Peng Zhang, Avraham BeâĂŽzer, E-L Florin, and Harry L Swinney. Collective motion and density fluctuations in bacterial colonies. *Proceedings of the National Academy of Sciences*, 107(31):13626–13630, 2010.
- [173] Karsten Kruse, Jean-François Joanny, Frank Jülicher, Jacques Prost, and Ken Sekimoto. Asters, vortices, and rotating spirals in active gels of polar filaments. *Physical review letters*, 92(7):078101, 2004.
- [174] R Aditi Simha and Sriram Ramaswamy. Hydrodynamic fluctuations and instabilities in ordered suspensions of self-propelled particles. *Physical review letters*, 89(5):058101, 2002.

-
- [175] R Aditi Simha and Sriram Ramaswamy. Statistical hydrodynamics of ordered suspensions of self-propelled particles: waves, giant number fluctuations and instabilities. *Physica A: Statistical Mechanics and its Applications*, 306:262–269, 2002.
- [176] David Saintillan and Michael J Shelley. Instabilities and pattern formation in active particle suspensions: kinetic theory and continuum simulations. *Physical Review Letters*, 100(17):178103, 2008.
- [177] Jeffrey S Guasto, Karl A Johnson, and Jerry P Gollub. Oscillatory flows induced by microorganisms swimming in two dimensions. *Physical review letters*, 105(16):168102, 2010.
- [178] Allison P Berke, Linda Turner, Howard C Berg, and Eric Lauga. Hydrodynamic attraction of swimming microorganisms by surfaces. *Physical Review Letters*, 101(3):038102, 2008.
- [179] Knut Drescher, Jörn Dunkel, Luis H Cisneros, Sujoy Ganguly, and Raymond E Goldstein. Fluid dynamics and noise in bacterial cell–cell and cell–surface scattering. *Proceedings of the National Academy of Sciences*, 108(27):10940–10945, 2011.
- [180] WE Uspal, Mikhail N Popescu, S Dietrich, and M Tasinkevych. Self-propulsion of a catalytically active particle near a planar wall: from reflection to sliding and hovering. *Soft Matter*, 11(3):434–438, 2015.
- [181] Konstantin Schaar, Andreas Zöttl, and Holger Stark. Detention times of microswimmers close to surfaces: influence of hydrodynamic interactions and noise. *Physical review letters*, 115(3):038101, 2015.

- [182] Michael Levitt. Protein folding by restrained energy minimization and molecular dynamics. *Journal of molecular biology*, 170(3):723–764, 1983.
- [183] Konstantin Klenin and Jörg Langowski. Computation of writhe in modeling of supercoiled dna. *Biopolymers*, 54(5):307–317, 2000.